The Dissertation Committee for Kevin Chek-Shing Marr certifies that this is the approved version of the following dissertation:

Investigation of Acoustically Forced Non-Premixed Jet Flames in Crossflow

Committee:

Noel T. Clemens, Co-Supervisor

Ofodike A. Ezekoye, Co-Supervisor

Matthew J. Hall

Venkat Raman

Philip L. Varghese

Investigation of Acoustically Forced Non-Premixed Jet Flames in Crossflow

by

Kevin Chek-Shing Marr, B.S.AS.E.; M.S.E.

Dissertation

Presented to the Faculty of the Graduate School of

The University of Texas at Austin

in Partial Fulfillment

of the Requirements

for the Degree of

Doctor of Philosophy

The University of Texas at Austin

May 2011

To Stephanie

Acknowledgements

First and foremost, I'd like to thank my wife, Stephanie, and my family for all their support throughout the course of my educational pursuits and for never once telling me that I should quit and find a real job. I am truly appreciative for the opportunity to work under both my advisors, Prof. Noel T. Clemens and Prof. Ofodike A. Ezekoye, and for all their guidance and mentorship over these past several years. Hopefully, I was able to absorb some of Dr. Clemens' attention to detail and Dr. Ezekoye's eye on the big picture. I'm especially grateful for our weekly Posse meetings, where some of the most insightful discussions I've had were shared over a pitcher a beer. I'd also like to thank my dissertation committee, Prof. Matthew J. Hall, Prof. Venkat Raman and Prof. Philip L. Varghese, for agreeing to serve on my committee and taking the time to review my dissertation. Of course, I cannot forget my fellow graduate students for their friendship and support—Dr. Mirko Gamba for showing me the ropes, being there to answer my questions even after you graduated, and most importantly teaching me how to make real Italian pizza, my fellow quals study buddies, Dr. Zach Murphree and Kelly Stephani, for our bonding experience over those three months of misery, and my fellow lab mates past and present, Dr. Justin Wagner, Dr. Venkat Narayanaswamy, Agustin Valdivia, Bryan Lochman, Ross Burns and Chris Combs, for sharing equipment and sharing ideas.

Investigation of Acoustically Forced Non-Premixed Jet Flames in Crossflow

Publication No._____

Kevin Chek-Shing Marr, Ph.D.

The University of Texas at Austin, 2011

Supervisors: Noel T. Clemens and Ofodike A. Ezekoye

The work presented here discusses the effects of strong acoustic forcing on jet flames in crossflow (JFICF) and the physical mechanisms behind theses effects. For forced non-premixed JFICF, the jet fuel flow is modulated using an acoustic speaker system, which results in a drastic decrease in flame length and soot luminosity. Forced JFICF are characterized by periodic ejections of high-momentum, deeply penetrating vortical structures, which draws air into the jet nozzle and enhances mixing in the nearfield region of the jet. Mixture fraction images of the non-reacting forced jet in crossflow are obtained from acetone planar laser-induced fluorescence and show that the ejected jet fluid is effectively partially premixed. Flame luminosity images and exhaust gas measurements show that forced non-premixed JFICF exhibit similar characteristics to unforced partially-premixed JFICF. Both strong forcing and air dilution result in net

reductions in NOx, but increases in CO and unburned hydrocarbons. NOx scaling analysis is presented for both forced non-premixed and unforced partially-premixed flames. Using flame volume arguments, EI_{NOx} scales with amplitude ratio for forced non-premixed flames, but does not scale with air dilution for unforced partially-premixed flames. The difference in scaling behavior is attributed to differences in flame structure. The effect of forcing on the flowfield dynamics of non-premixed JFICF is investigated using high-speed stereoscopic particle image velocimetry and luminosity imaging. The frequency spectra of the windward and lee-side flame base motions obtained from luminosity movies of the forced JFICF show a peak at the forcing frequency in the lee-side spectrum, but not on the windward-side spectrum. The lee-side flame base responds to the forcing frequency because the lee-side flame base stabilizes closer to the jet exit. The windward-side flame base does not respond to the forcing frequency because the integrated effect of the incident crossflow and vortical ejections leads to extinction of the flame base. From the PIV measurements, flowfield statistics are conditioned at the flame base. The local gas velocity at the flame base did not collapse for forced and unforced JFICF and was found to exceed $3S_L$. The flame propagation velocity was determined from the motion of the flame base, which is inferred from regions of evaporated seed particles in the time-resolved PIV images. The flame propagation velocity collapses for forced and unforced JFICF, which implies that the flame base is an edge flame; however, the most probable propagation velocity, approximately 2-$3S_L$, is larger than propagation velocity predicted by edge flame theories. A possible explanation is that the flame propagation is enhanced by turbulent intensities and flame curvature.

Table of Contents

Nomenclature

α	absorption coefficient in m^{-1}
β	mixture fraction decay exponent
χ_i	mole fraction for species *i*
$\Delta D_{PLIF\text{-}PLMS}$	bias error of the flame base
$\Delta x_{PLIF\text{-}PLMS}$	*x*-component of the bias error of the flame base
$\Delta y_{PLIF\text{-}PLMS}$	*y*-component of the bias error of the flame base
Δt	PIV time delay
Δt_{AB}	PIV time delay between pulses *A* and *B*
Δt_{BA}	PIV time delay between pulses *B* and *A*
ϕ	species quantum efficiency
φ	angle of camera relative to image normal
λ	wavelength of laser
θ	angle of light ray relative to laser beam direction
ρ_a	density of dilution air
ρ_{cf}	density of crossflow air
ρ_j	density of jet fuel
σ	molecular absorption cross-section
τ_G	global flame residence time
$\tau_{G,crit}$	critical global flame residence time

ω_z	out-of-plane vorticity component
ζ	mixture fraction
ζ_j	mixture fraction of fluid exiting the jet
ζ_s	stoichiometric mixture fraction
A	Jet in crossflow trajectory proportionality constant
B	Jet in crossflow trajectory exponent
C	concentration of absorbing species
d	jet exit diameter
d^*	effective jet exit diameter
EI_i	emissions index for species i
f	forcing frequency
$h_{lift,lee}$	lee-side flame liftoff height
$h_{lift,wind}$	windward-side flame liftoff height
I	attenuated laser light intensity
I_o	non-attenuated laser light intensity
L	stroke length
L/d	stroke ratio
L_o	laser sheet correction image
L_{mod}	modified laser sheet correction image for absorption
l_f	flame length
$l_{f,forced}$	flame length of forced non-premixed flame
$l_{f,premix}$	flame length of unforced partially-premixed flame

$\dot{m}_a$	mass flow rate of dilution air
$\dot{m}_{cf}$	mass flow rate of crossflow air
$\dot{m}_f$	mass flow rate of fuel
$\dot{m}_{NOx}$	mass production rate of NOx
MW_i	molecular weight of species i
N_e	number of photons emitted per unit area
N_i	incident photon flux
P	pressure
Q_f	flow rate of fuel
r	blowing ratio
$\mathrm{Re}_{\mathrm{j,mean}}$	jet Reynolds number based on mean jet exit velocity
$\mathrm{Re}_{\mathrm{j,peak}}$	jet Reynolds number based on peak jet exit velocity
r_{mean}	blowing ratio based on mean jet exit velocity
r_{peak}	blowing ratio based on peak jet exit velocity
s	jet in crossflow trajectory path coordinate
$\lvert S_b \rvert$	flame propagation speed
$S_{b,x}$	x-component of the flame propagation velocity
$S_{b,x}$	y-component of the flame propagation velocity
S_{jet}	jet in crossflow PLIF image
S_L	premixed laminar flame speed
S_T	premixed turbulent flame speed

T	temperature
u	x-component of the fluid velocity
u'	x-component velocity fluctuation
u'_o	velocity fluctuation tangent to flame front propagation direction
U_{cf}	crossflow velocity
$u_{f,x}$	x-component of the flame base velocity
$u_{f,y}$	y-component of the flame base velocity
U_j	jet exit velocity
$U_{j,mean}$	mean jet exit velocity
$U_{j,peak}$	peak jet exit velocity
V	fluid speed
v	y-component of the fluid velocity
v'	y-component velocity fluctuation
V_f	flame volume
w	w-component of the fluid velocity
w'	w-component velocity fluctuation
$\overline{\dot{w}_{NOx}}$	NOx volumetric production rate
x	crossflow-streamwise coordinate
x_f	x-location of the flame base
y	crossflow-normal coordinate
Y_f	mass fraction of fuel
y_f	y-location of the flame base

Y_i	mass fraction of species i
z	out-of-plane coordinate

List of Tables

List of Figures

Chapter 1: Introduction

1.1 MOTIVATION

Jets in crossflow (JICF) and jet flames in crossflow (JFICF) are fundamental fluid mechanical geometries that play an important role in many practical engineering systems. In particular, understanding the characteristics of JFICF is essential in designing combustion systems such as gas flares, gas turbines, and jet engines. Owing to increasing concern on environmental issues, characterizing the mechanisms for pollutant emission in such flames has become increasingly critical. For example, there is growing interest in developing strategies to reduce smoke and other pollutants emitted from refinery flare stacks, particularly in the presence of a high crosswind. For these types of flame systems, smoke reduction has often been accomplished by diluting the fuel flow with air or steam. In gas turbines, fuel is often premixed or partially premixed with air in order to reduce pollutants, in particular NOx; however premixed combustion has inherent stability and safety issues related to blowout and flashback. Interestingly, previous work has shown that at sufficiently high amplitude ratios, modulation of the fuel flow rate in free jet flames can create significant mixing in the near field resulting in significant reductions in soot production and flame length (Lakshminarasimhan *et al.* 2006, 2007); however, little work has been done to characterize the flowfield structure and pollutant emissions for the JFICF configuration.

1.2 JETS AND JET FLAMES IN CROSSFLOW

Non-reacting jets in crossflow have been studied extensively over the years. As early as the 1930s, researchers have been interested in a variety of JICF applications from chimney plumes (Bosanquet and Pearson 1936) to V/STOL aircraft (Garner 1967). Owing to the considerable amount JICF research, only several relevant works will be highlighted here. A review paper by Margason (1993) gives a comprehensive historical overview of JICF research including both experimental and numerical studies. The majority of work discussed by Margason was published before the 1990s and focused on the global features of the JICF such as jet penetration and trajectory, velocity and vorticity fields, and induced pressure distributions along the wall.

Shown in Figure 1.1, the JICF is characterized by a complex system of four main vortical structures—horseshoe vortices, jet shear-layer vortices, wake vortices, and a counter-rotating vortex pair (CVP)—generated by the interaction of the jet with the crossflow (Fric and Roshko 1994, Kelso and Smits 1994, Kelso *et al.* 1996). Despite its complexity, several works (Pratte and Baines 1967, Margason 1968) found that the trajectory of unforced JICF can be properly scaled according to a simple power law

$$\frac{y}{rd} = A\left(\frac{x}{rd}\right)^{B}, \tag{1.1}$$

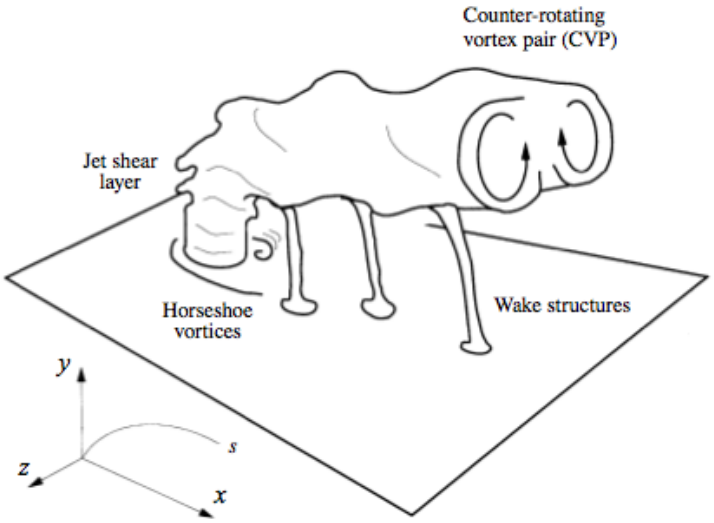

Figure 1.1. Main vortical structures of the jet in crossflow. Taken from Smith and Mungal (1998). Reprinted with permission from Cambridge University Press.

where A and B are constants, x and y are the spatial co-ordinates in the crossflow-streamwise and crossflow-normal directions, and d is the jet diameter. The *blowing ratio*, r, is defined as

$$r = \sqrt{\frac{\rho_j U_j^2}{\rho_{cf} U_{cf}^2}}, \tag{1.2}$$

where ρ is the density, U is a characteristic velocity, and the subscripts j and cf refer to jet and crossflow, respectively. Pratte and Baines (1967) using photographs of jets seeded with smoke cite values of A=2.05 and B=0.28, while a self-similarity analysis by Broadwell and Breidenthal (1984) found B=1/3. Values reported in the literature range

from $1.2<A<2.6$ and $0.28<B<0.34$ (Hasselbrink and Mungal 2001a). The variation in coefficient values can be attributed to the different definitions of the jet trajectory based on jet center steamline, maximum velocity or maximum concentration.

Other studies have focused on the mixing characteristics of the JICF. In the same study mentioned above, Broadwell and Breidenthal (1984) studied mixing of an aqueous jet in a water tunnel and showed that the mixing length was shorter at higher Reynolds numbers due to the presence of small-scale turbulent structures. Smith and Mungal (1998) used planar laser-induced fluorescence (PLIF) of acetone vapor seeded into the jet to measure the 2-D scalar concentration field. They found that when the jet trajectory coordinate, s, is normalized by rd, the mean centerline concentration in the nearfield follows an $s^{-1.3}$ decay rate (compared to s^{-1} for free jets), and that the far-field decay approaches a slower $s^{-2/3}$ decay rate indicating a more wake-like behavior. Su and Mungal (2004) considered two JICF configurations—one where the jet nozzle is flush with the wall and the other where the nozzle protrudes into the freestream flow. The latter describes the typical smokestack or, in the reacting case, gas flare geometry. They found that the scaling results were consistent between both flow geometries, but the centerline concentrations in the nearfield decayed at an s^{-1} rate similar to free jets. The difference in decay rates between their findings and that of Smith and Mungal was attributed to the difference in the exit velocity profiles—pipe flow profile used by Su and Mungal compared to a top hat profile used by Smith and Mungal.

Somewhat less work has been directed toward the reacting counterpart of the JICF, the jet flame in crossflow. Kalghatgi (1983) studied the shapes and sizes of non-premixed

hydrocarbon JFICF and identified five shape parameters that can be related to the jet diameter, the jet exit velocity, the crossflow speed, and the density of the jet fluid by one equation. Hasselbrink and Mungal (2001b) used a simultaneous particle image velocimetry (PIV) and OH PLIF technique to investigate the effect of heat release on the flowfield of a lifted, non-premixed JFICF. They found that the scaling laws developed for JICF reasonably predicted the streamline trajectory of the JFICF. They also suggested that significant partial premixing occurs upstream of the flame front, but by mid-flame, the premixed air has been fully consumed resulting in a non-premixed flame. Han and Mungal (2003) also applied a simultaneous PIV/CH PLIF to study a hydrogen piloted JFICF, where the flame is attached to the lee side of the nozzle lip but lifted on the windward side. They found that the CH structures appear thicker on the lee side than on the windward side and that the correlation between high shear strain rate and the CH layer was not as distinct on the lee side compared to the windward side. Both of these observations were attributed to significant partial premixing on the lee side.

1.3 FORCED JETS AND JET FLAMES

In forced flames, acoustic or mechanical forcing is applied to the fuel jet to induce perturbations or to modulate the jet. Several researchers have shown benefits of using forced flames in combustor design. Because complex physics arise from the coupled interaction between the unsteady fluid motion and species reactions, significant effort has been directed toward understanding the effects of forcing on both the flowfield and combustions characteristics.

1.3.1 Engineering Applications of Forced Jet Flames

Forced jets have been shown to be useful in several engineering applications. In the combustion field, pulse combustors rely on flapper valves to control the fuel supply to the combustor section. A review paper by Zinn (1992) and works by Keller *et al.* (1994) discuss pulse combustion research and conclude that pulsations increase mixing and heat transfer rates and result in lower emissions of nitrogen oxides (NOx), carbon monoxide (CO) and soot. In general, premixed reactants are used, but some work has been done for non-premixed systems (Tang *et al.* 1995). Other studies have investigated the use of high-frequency, low-amplitude acoustic excitation as an active control mechanism for acoustic instabilities in premixed combustion chambers (Gutmark *et al.* 1989, Gutmark *et al.* 1992). They showed that self-excited combustion oscillations that arise from interactions between chamber acoustic modes and jet instabilities can be suppressed by forcing the jet with an acoustic speaker at the specific frequency and phase delay required to cancel out the acoustic perturbations.

1.3.2 Flowfield Structure of Forced Jets and Jet Flames

Studies by Crow and Champagne (1971), Parikh and Moffat (1982), Vermeulen *et al.* (1992), Johari and Paduano (1997), among others showed that various methods of forcing affect both free jets and confined jets by increasing entrainment and improving spreading and mixing characteristics. Various studies also showed similar results for the crossflow configuration. Vermeulen *et al. (*1990) acoustically pulsed an air JICF and found that pulsing increased jet penetration by up to 92%. They found that the centerline

turbulence decayed faster for the pulsed jet and concluded that the pulsing increases jet mixing with the lower momentum crossflow. M'Closkey *et al.* (2002) used acoustic forcing by driving a speaker with either sine or square waveforms in a wind tunnel and found that for square wave excitation the optimal jet penetration occurs at subharmonics of the natural vortex shedding frequency of the jet. Figure 1.2 shows a smoke visualization image of a forced jet forced with a 110 Hz sine wave taken from M'Closkey *et al.* This frequency exhibited the highest penetration length into the crossflow.

Johari *et al.* (1999) and Eroglu and Breidenthal (2001) both investigated fully modulated JICF in a water tunnel by using a solenoid valve to periodically shut off the jet supply. This forcing method allowed for adjustments of both the frequency of the pulses and the duty cycle or portion of time the valve is open during each cycle. Both groups

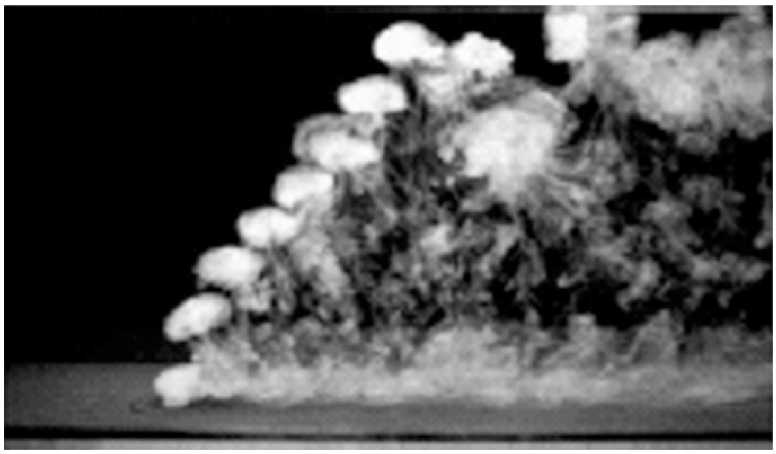

Figure 1.2. Smoke visualization of a forced nitrogen jet in crossflow at $r_{mean} \approx 2.6$ taken from M'Closkey *et al.* (2002). The jet is acoustically forced with a 110 Hz sine wave through a loud speaker. Crossflow is left to right. Reprinted with permission from Cambridge University Press.

used PLIF to visualize the unsteady flowfield and a chemical reaction technique where an acid solution in the crossflow reacted with a pH indicator in the jet to measure mixing rates and mixing lengths. They observed that forcing results in the ejection of distinct vortex structures that penetrate into the crossflow and are then convected downstream. Johari *et al.* (1999) claims that the penetration increases by a factor of 5 for certain conditions and under most forcing conditions the mixing rate doubled. Eroglu and Breidenthal (2001) observed that penetration increases up to 70% and mixing lengths decreased by 50%. Another work by Johari (2006) identifies different flow regimes for non-reacting forced JICF the can be mapped according to the stroke ratio, L/d, where L is the stroke length, or length of the fluid slug ejected during one cycle and d is the jet diameter. For forced JICF with vortical ejections that do not interact with each other, four flow regimes exist—*distinct vortex rings* ($L/d<4$), *vortex rings/puffs with a trailing column* ($4<L/d<20$), *turbulent puffs* ($20<L/d<75$), and *steady jet segments* ($L/d>75$). The vortex ring with a trailing column regime is characterized by two distinct trajectory branches from the high momentum vortex rings and the low momentum trailing column. In the turbulent puff regime, the trailing column momentum is sufficiently high, and therefore only a single trajectory exists. For periodically forced jet flames, the stroke ratio can be defined as

$$\frac{L}{d} = \frac{U_{j,peak}}{fd} \tag{1.3}$$

where f is the forcing frequency (Lakshminarasimhan *et al.* 2006). In this definition, the stroke ratio is simply the inverse of the Strouhal number based on maximum jet exit velocity, $U_{j,peak}$.

Studies of axisymmetric jet flames have shown that forcing strongly influences the fluid dynamics in the near region of the jet. Oh and Shin (1998) visualized a forced laminar jet flame using Mie scattering images and found that the ejected vortex structures promote intense mixing just downstream of the nozzle. Other studies have shown that sufficiently large perturbations can draw ambient fluid into the nozzle and promote in tube premixing of the fuel and air. Muramatsu and Era (2003) using a concentration probe to make point measurements in a pulsed CO_2 jet cited in-tube mixing of about 10%. Using acetone PLIF, Lakshminarasimhan *et al.* (2007) imaged in-tube mixture fraction of a forced turbulent jet at a Reynolds number of 1820. In their study, they forced the jet by using a solenoid valve to drive a quartz resonance tube at 250 Hz. Figure 1.3 shows phase-averaged mixture fraction inside the fuel delivery tube. Forcing at sufficiently large amplitudes draws ambient air into the nozzle and effectively partially premixes the resultant ejected fuel—mixture fraction of the fuel exiting the fuel delivery tube is approximately 0.45.

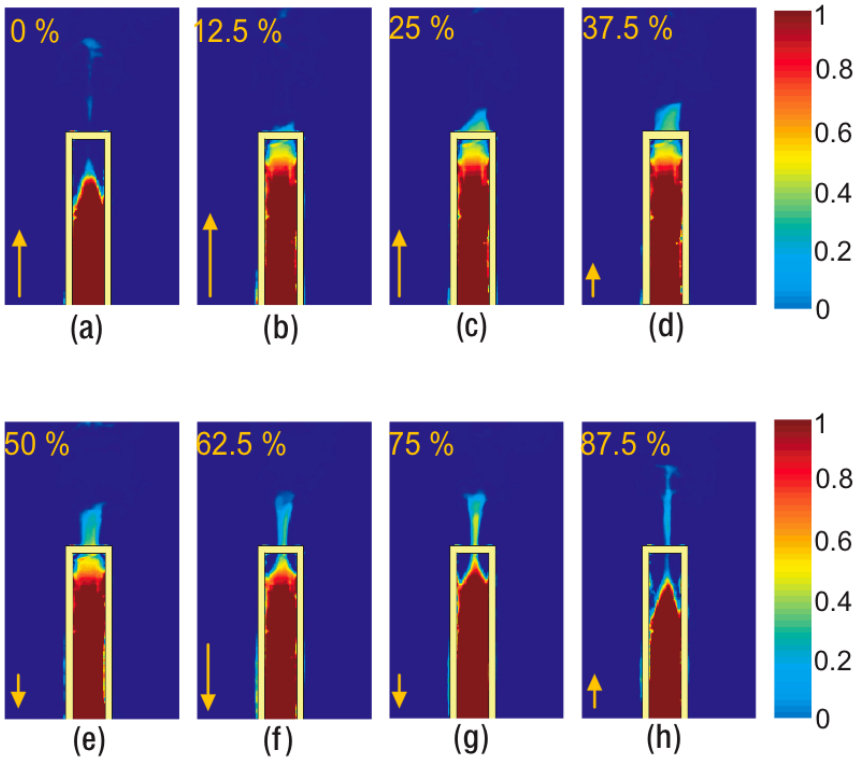

Figure 1.3. Sequence of phase-averaged in-tube mixture fraction images of a resonantly forced air jet with a mean Reynolds number of 1820 forced at 250 Hz taken from Lakshminarasimhan *et al.* (2007). Each of the images (a-h) is taken at eight equally spaced time locations within a single forcing cycle. The arrows indicate the relative magnitude and direction of the jet exit velocity. Reprinted with permission from Elsevier.

1.3.3 Combustion Characteristics of Forced Jet Flames

In addition to increasing local mixing near the jet exit, studies have also observed that high-frequency pulsing affects combustion characteristics such as flame lengths and species emissions. Several studies observed reduced flame lengths (as much as 70-80%) as a result of high-frequency forcing (Lovett and Turns 1993, Chao *et al.* 1996, Hermanson *et al.* 2004, Lakshminarasimhan *et al.* 2006); however, there is no consensus

on whether forcing reduces pollutant emission such as nitrogen oxides (NOx), carbon monoxide (CO) and unburned hydrocarbons (UHC). Chao *et al.* (1996) found that high frequency acoustic excitation (3 KHz) of a partially-premixed jet flame reduced NOx without increasing CO. They conclude that the reduction in NOx is a due to enhanced upstream premixing which results in a lean premixed condition and reduced residence time; however, they did not fully quantify the excitation strength or amplitude ratio. Kim *et al.* (2009) found that acoustic forcing applied to the coaxial air of a hydrogen/coaxial air jet flame reduced flame length and NOx emissions approximately 15% and 25%, respectively. A series of studies investigated the emissions of NOx, CO and UHC for fully modulated jet flames which operate in the high-amplitude, low-frequency limit by switching the fuel flow rate on and off (Hermanson *et al.* 2004, Fregeau and Hermanson 2009). In general, their measurements show that fully modulated jet flames reduce NO emissions and increase CO and UHC, but at specific forcing conditions, CO and UHC emissions remained relatively low. Lovett and Turns (1993) considered a wide range of forcing frequencies (2 to 1340 Hz) and found that NOx emissions were largely unaffected by pulsing despite the fact that the flames were pulsed strongly enough to become effectively partially premixed. The amplitude ratios they considered were much lower than those considered by Fregeau and Hermanson (2009). Clearly, the effect of forcing on pollutant species depends on forcing conditions; however, none of the previous works clearly identify physical mechanisms for pollutant species production.

The most similar study to the current work investigated acoustic excitation of stack flares in crossflow (El Behery *et al.* 2005). The presence of the stack can

substantially influence the flame characteristics since the tube wake acts as a flame holder (El Behery *et al.* 2005). Their measurements showed reductions in NOx, CO and UHC; however, limited flow field measurements did not enable them to identify the physical mechanisms responsible for the reduced pollutants although enhanced mixing was believed to be a cause.

1.4 JET FLAME POLLUTANT EMISSIONS

As discussed above, several studies observed modification of pollutant emissions species due to forcing. Pollutant species production in flames is a complex process that depends on several different factors, namely residence time for species formation, flame radiation, and local quenching. The roles of each of these mechanisms in forced flames have not been clearly identified. Because studies observed that forcing results in effective partial premixing, a brief discussion of partially-premixed flames is warranted. Also, significant work directed toward developing a universal NOx scaling law for non-premixed jet flames has proven to be useful in identifying NOx production mechanisms. The following sections review literature pertaining to emissions from partially-premixed jet flames and simple NOx scaling laws.

1.4.1 Partially-Premixed Jet Flame Pollutant Emissions

In an experimental study, Turns *et al.* (1993) made various flame measurements to characterize the effect of partially premixing. They considered three hydrocarbon fuels—methane, ethylene, propane—and increased the jet equivalence ratio by adding air

to a fixed amount of fuel. As the level of partially premixing increased, the jet Reynolds number increased as well. Their measurements showed that increasing air dilution resulted in reduced flame lengths, residence times and radiant fractions and higher flame temperatures compared to the non-premixed jet flame for all three fuels. The NOx emissions followed a non-monotonic trend and initially increased and then decreased as more air was added to the jet.

Studies by Gore and Zhan (1996) and Lyle *et al.* (1999) studied laminar and turbulent partially-premixed flames, respectively. In their studies, both groups held the heat release rate constant by fixing the fuel mass flow rate while increasing the air dilution. Both studies identified minimum NOx emissions at burner equivalence ratios of approximately 2 for laminar flames and 1.5 for turbulent flames. Furthermore, both studies showed that CO and UHC decrease as partial premixing increases. Another study also identified minimum NOx emissions at burner equivalence ratios of 2.2 for ethane/air mixtures (Kim *et al.* 1995). None of the studies give a definitive explanation for the NOx trend; however, Gore and Zhan suggest that the existence of minimum NOx is due to a competition between the thermal and prompt NO mechanisms. Furthermore, no studies have considered the affect of a crossflow on partially-premixed jet flames.

1.4.2 Simple EI_{NOx} Scaling

Development of a simple scaling law for NOx production in non-premixed turbulent flames has been well documented by many studies. Specific results from theses studies will not be presented here. A review paper by Turns (1995) gives an excellent

overview of results from NOx scaling literature. In the studies summarized by Turns, NOx emissions measurements did not collapse with simple scaling due to the complex dependence of NOx formation on several parameters. Turns identified four major factors relevant to NOx scaling—the relative importance of NOx formation pathways, the relationship between flame strain and NOx yield, the effect of superequilibrium radical concentrations and temperature, and the importance of flame radiation. Although simple scaling does not collapse NOx emissions measurements in turbulent jet flames, scaling analysis has been useful in identifying important NOx mechanisms.

The simple NOx scaling presented in Turns' review is based upon analysis from Peters and Donnerhack (1981) where the NOx emissions index, EI_{NOx}, is given by

$$EI_{NOx} = \frac{\dot{m}_{NOx}}{\dot{m}_f} = \frac{\dot{m}_{NOx}}{\rho_f U_f \pi d^2 / 4}, \tag{1.4}$$

where $\dot{m}_f$ is the mass fuel flow rate of the jet and ρ_f, U_f, and d are the jet fluid density, exit velocity and diameter. If only thermal NOx production is considered the NOx mass production rate, $\dot{m}_{NOx}$, is obtained by integrating the NOx volumetric production rate, $\dot{w}_{NOx}$, over the flame volume, V_f. For simplicity, the integral of $\dot{w}_{NOx}$ can be interpreted as the product of the mean NOx volumetric production rate and the flame volume, $\overline{\dot{w}_{NOx}} V_f$. A scaling relationship for EI_{NOx} can be written as follows:

$$EI_{NOx} \sim \overline{\dot{w}_{NOx}} \left(\frac{V_f}{\rho_f U_f d^2} \right) \tag{1.5}$$

The parameter $V_f / U_f d^2$ can also be viewed as global flame residence time. For turbulent jet flames, the jet can be viewed as a self-similar cone, so V_f is expected to scale with the cube of the flame length, l_f. Assuming $\overline{\dot{w}_{NOx}}$ is constant, Eq. 1.5, can be simplified to

$$EI_{NOx} \sim \frac{l_f^{\,3}}{\rho_f U_f d^2} \tag{1.6}$$

Note that the scaling is strictly for thermal NOx—prompt NOx and N_2O pathways are neglected.

1.5 LIFTED TURBULENT FLAME STABILITY

Despite the presence of high strain vortical structures, forced flames are observed to be surprisingly stable (Lakshminarasimhan *et al.* 2007). Few studies have considered the stabilization characteristics of forced flames. Furthermore, there have been no studies on the impact of a crossflow on the stability of forced flames. Stability of lifted turbulent flames, however, has been studied extensively by several groups, and several stability theories have been proposed. An overview of these theories is presented below.

1.5.1 Flame Stability in Forced Flames

The stability of forced flames has been studied by several groups. Lakshminarasimhan *et al.* (2007) used OH PLIF to mark the reaction zone of a forced axisymmetric non-premixed jet flame, and observed that the OH zones showed little correlation with the phase of forcing. They also found that an OH structure exists just downstream of the head of the vortical structure, which bridges the reaction zone on either side of the flame. They suggest that this flame "bridge" plays an important role in the flame stability. Chao *et al.* (2002) studied the acoustic excitation of a circular methane flame using several laser diagnostic techniques. They found that the potential core of the acoustically excited jet flame was shorter and the flame base was located farther upstream compared to the unexcited case. They suggest that the enhanced stabilization is the result of the upstream portion of vortex thickening the flammability layer, which promotes flame propagation. Demare and Baillot (2004) also investigated an acoustically forced jet flame and found that forcing disorganizes the jet structure and homogenizes the fluid mixture. They showed that the scalar dissipation rate decreases, which results in a thicker flammability layer. In addition to measuring NOx and flame lengths, Kim *et al.* (2009) also studied the flame-vortex interaction of an acoustically forced coaxial hydrogen jet flame. From simultaneous PIV/OH PLIF measurements, they observed that the vortex stretches the flame and increases the flame surface. In a review paper on vortex-flame interactions, Renard *et al.* (2000) explains that compressive strain in the upstream portion of the vortex results in flame thickening and extensional strain in the downstream portion of the vortex results in flame thinning.

1.5.2 Lifted Flame Stabilization Theories

Significant amount of research has been directed toward flame stability of lifted turbulent jet flames. Review papers by Pitts (1989) and Lyons (2007) provide excellent summaries of efforts made toward understanding lifted flame stabilization mechanisms. Lyons categorized the various stabilization theories into five categories—*Premixed Flame Theory*, *Critical Scalar Dissipation Concept*, *Turbulent Intensity Theory*, *Large Eddy Concept*, and *Edge-Flame Concept*. In *Premixed Flame Theory*, Vanquickenborne and Van Tiggelen (1966) proposed that lifted flames stabilize where the average local fluid velocity entering the flame base equals the premixed turbulent burning velocity; however, this theory does not account for the effect of large-scale jet structures. Peters and Williams (1983) argued that the mixture upstream of the leading edge of the flame is not significantly premixed and proposed the *Critical Scalar Dissipation Concept*. Here, the turbulent flame stabilizes where the scalar dissipation rate falls below a critical value. Criticism of this theory points out that partial premixing is ignored and differentiating between regions of mean scalar dissipation and shorter-lived high scalar dissipation is critical. The *Turbulent Intensity Theory* discussed by Kalghatgi (1984) states that the turbulent burning velocity, which is related to the turbulence intensity at the leading edge, determines flame propagation. The *Large Eddy Concept* (Broadwell *et al*. 1984) highlights the importance of large-scale structures where the flame leading edge propagates upstream with large eddy motions. This theory implies that it is necessary for hot products to be transported upstream by large structures near the jet edge, which, as Lyons observed, is unsupported by experimental results. Details of the *Edge-Flame*

Concept is discussed in a review paper by Buckmaster (2002). In the *Edge-Flame Concept*, the flame leading edge is assumed to be partially premixed, and therefore can propagate upstream against the local flow at the premixed laminar flame speed. Flame stabilization is dictated by triple or tribrachial flame structure, which is made up of three branches—a diffusion flame, a lean premixed flame, and a rich premixed flame—that meet at a single point or triple point (Figure 1.4). Triple flames have been identified in lifted laminar flames using modern laser diagnostics (Amantini *et al*. 2004), but the three distinct branches have yet to be directly observed in lifted turbulent flames with modern imaging techniques. Muñiz and Mungal (1997) suggested that the three branches may not always exist in a turbulent flame due to flame wrinkling. Instead, the flame structure is characterized by a premixing region followed by a diffusion tail. The existence of triple flames structure in turbulent flames has been inferred using simultaneous Rayleigh imaging and CH-PLIF (Watson *et al*. 2000). The review by Pitts concluded that no satisfactory flame stabilization theory exists; however, Pitts did not include a discussion on the *Edge-Flame Concept*. Lyons, in his review, offered a slightly different view stating that the five categorized theories are not necessarily independent and cited that most experiments support more than one category.

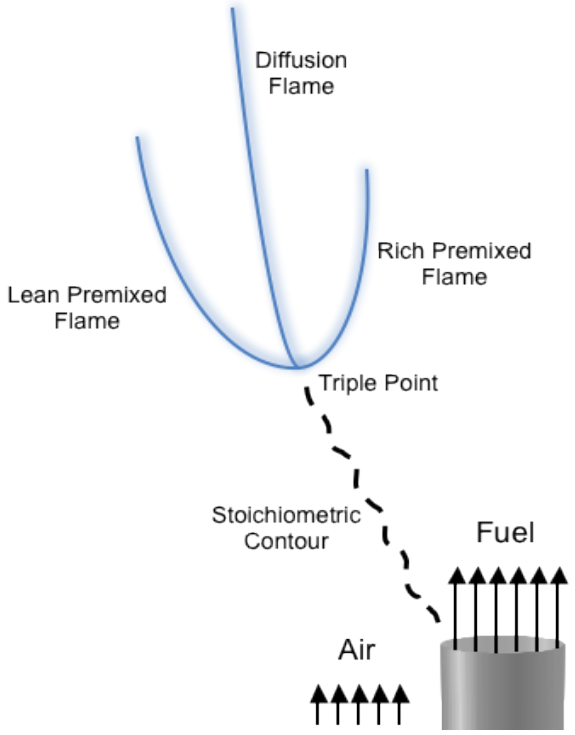

Figure 1.4. Schematic of triple flame structure in a lifted non-premixed jet flame.

1.5.3 Flame Propagation Velocity

The *Edge-Flame Concept* has been gaining more traction over the past decade. One aspect of the *Edge-Flame Concept* is that the heat release effects on the flowfield are not neglected. Streamlines have been found to diverge ahead of the edge flame in numerical simulations of laminar triple flames in coflow (Ruetsch *et al.* 1995) and experimental work in lifted turbulent flames (Upatnieks *et al.* 2004). Also, analysis shows that edge flames can have either positive or negative propagation velocities (Buckmaster 2002).

Experiments by Muñiz and Mungal (1997) used PIV to measure the velocity field at the base of lifted turbulent flames. They considered methane and ethylene flames over a range of Reynolds numbers from 3800 to 22,000. Alumina particles or fog particles were used to seed the flow. Although, simultaneous CH or OH PLIF imaging was not used to mark the reaction zone, the thermal boundary was identified from the abrupt decrease in seed density of alumina particles, or evaporation of fog particles, across the flame front. They found that the instantaneous flame base anchored in low velocity regions. The mean local gas velocity conditioned at the flame base location was near the laminar flame speed, S_L; the instantaneous local gas velocity did not exceed $3S_L$. The value $3S_L$ was also suggested to be the critical coflow velocity for flame blowout. Streamlines were observed to diverge upstream of the flame front suggesting triple flame-like behavior. Hasselbrink and Mungal (1998) used a similar experimental method to investigate the flowfield of the stabilization region of a lifted jet flame in crossflow. In their study, they considered a Re=6950 methane jet issuing perpendicularly into a 1.9 m/s crossflow (r =10). Glycerol fog was used to seed the flow and the evaporation marked the outline of the thermal preheat zone of the flame. Instantaneous velocity samples were conditioned at the flame base in both the windward and lee sides of the flame and were found to be larger than the $3S_L$ limit observed in coflowing flames. The mean velocity normal to the flame at both the windward and lee side location was found to be near $3S_L$. Hasselbrink and Mungal suggested that the discrepancy may have been due to significant three dimensionality in the crossflow case compared to the coflow, which would complicate the interpretation of planar velocity measurements. They further commented

that flame propagation velocity, or relative velocity of the flame and fluid, is the more relevant parameter. Their experimental configuration, however, was unable to acquire velocity of the flame motion.

In order to measure flame propagation velocity, both the local gas velocity and flame velocity must be known. The studies by Muñiz and Mungal (1997) and Hasselbrink and Mungal (1998) used a 10 Hz PIV system and were unable to sufficiently track the time evolution of the flame. Upatnieks *et al.* (2002, 2004) used a cinema PIV technique to study lifted turbulent non-premixed jet flames. Their study considered two jets—a 77% methane/23% nitrogen jet at Re=4200 and a pure methane jet at Re=8500. They used two high repetition rate Nd:YAG lasers operating at 4 kHz to acquire sequential PIV velocity fields 250 μs apart, which allowed them to resolve the flame motion sufficiently. Similar to previous studies, they seeded the flow with ceramic particles and used the decrease in seed density to mark the thermal boundary of the flame. From the time history of the flame, they extracted flame velocities, and hence flame propagation velocities. In their first study, the measured flame propagation velocities were found to be similar to the laminar flame speed. They also observed appearances of isolated islands of flame upstream of the previous flame base suggesting azimuthal wrinkling of the flame. In the second study, they noted that the propagation speed of the flame base was not significantly correlated with local turbulence intensity or large eddy motions suggesting that stabilization theories based on turbulent flame propagation were not valid for jet flame at Reynolds numbers below 8500. They concluded that despite large turbulence levels and velocities in the jet, edge flames create their own low-velocity, low-turbulence

region and remain nearly laminar with a propagation velocity that is matched to the local gas velocity. Their study, however, did not extend to the crossflow configuration.

1.6 OBJECTIVE

While there have been a number of studies on jet flames in both coflow and crossflow, few have considered the effects of forcing on JFICF. Various studies have investigated the resultant emissions from forced flames, but none have adequately detailed the physical mechanisms behind pollutant species formation, in particular NOx. Furthermore, detailed measurements of the fluid mechanics of forced JFICF have not been made. As such, much remains to be understood about the impact of high amplitude forcing on pollutant emissions for this complex combustion system. For harmonic forcing considered in this study, the term *high amplitude forcing* refers to maximum velocity fluctuations greater than 15% of the mean velocity (Lakshminarasimhan 2006).

Interestingly, the main focus of forced jet flame studies in both vertical and crossflow geometries have been on global combustion characteristics. Little attention has been directed toward flame stability—one of the more interesting aspects of forced flames. Lakshminarasimhan *et al*. (2006, 2007) showed that despite the large strain rates induced by the high amplitude forcing, the flame is lifted only several diameters downstream of the jet exit and remains relatively stable. Several theories of flame stabilization have been proposed for lifted non-premixed turbulent jet flames; however, these theories have not been generalized to forced flames.

The objective of the current investigation is to gain an improved understanding of how strong pulsations of varying amplitude affect the mixing characteristics, flow structure, and global emissions of JFICF. Identifying the physical mechanisms that affect pollutant production and understanding the effects of forcing on flame stability are essential in future development of any forced jet flame engineering applications. In the present study, the jet fuel flow is forced with a sinusoidal acoustic wave to produce a nearly harmonic velocity variation at the jet exit. Laser diagnostics and high-speed imaging are used to study the flow structure and mixing characteristics of forced JFICF, while global NOx, CO and UHC emissions are measured in the exhaust gases.

Chapter 2: Experimental Setup

The experimental facility was located in the W. R. Woolrich Laboratories at the University of Texas at Austin. The following sections include details of the facility and a discussion of experimental techniques.

2.1 CROSSFLOW FACILITY

The experimental facility was designed specifically to study non-reacting and reacting jet in crossflow geometries and consisted of a horizontal wind tunnel and a pulsed jet apparatus designed to provide variable amplitude ratios.

2.1.1 Horizontal Wind Tunnel

The wind tunnel, shown in Figure 2.1, was driven by a variable-speed 1.5 hp centrifugal blower, which provided freestream crossflow velocities of up to 4 m/s in the test section. The crossflow air passed through a series of flow conditioning elements consisting of two sets of perforated plates (cell size about 3.2 mm), a honeycomb flow-straightening element (cell size about 3.2 mm, 25 mm thick) and three layers of fine wire-mesh of decreasing size (from 18 to 30 mesh per inch) prior to the 1 m long test section with a cross-section of 0.4 m × 0.4 m. The test section was equipped with optical access on the sidewalls and the top wall. The sidewalls have interchangeable panels so that entire test section can be viewed by rearranging the window panel. Although the crossflow facility was not designed with a contraction—it was conditioned only by the

described flow conditioning elements—the flow quality achieved in test section was acceptable for the purpose of the study. The flow velocity profile was measured with a calibrated hot-film anemometer (TSI model 1051-2 mounted with a model 1210 probe) in the center-plane of the test section along a vertical line coincident with the jet exit, and was found to be uniform to within 2% in the freestream. The turbulence intensity across the whole test section is less than 0.5%, and the boundary layer thickness was about 7 mm at the jet centerline.

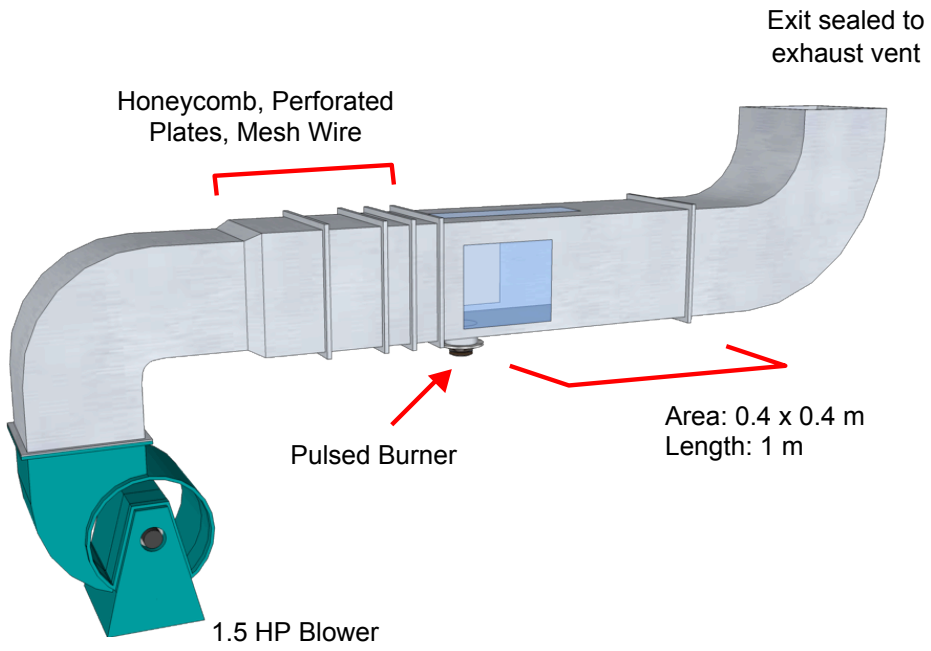

Figure 2.1. Schematic of the crossflow wind tunnel.

2.1.2 Pulsed Jet Apparatus

The pulsed jet apparatus, shown in Figure 2.2, consisted of an axisymmetric plenum that was flush mounted to the floor of the test section. At the top of the chamber, the jet fluid was accelerated through a round contour nozzle with a 6.35 mm exit diameter. The 144:1 area ratio nozzle contraction provided a top hat velocity profile at the nozzle exit. A honeycomb flow straightening element and wire mesh was used to condition the flow upstream of the nozzle. A 140W, 6.5 in loudspeaker (Audiobahn ABC600T) was mounted to the bottom of the plenum, and the speaker cone was sealed with a thin layer of silicon sealant to insure that fluid did not leak through the porous cone. A sinusoidal signal was generated by a harmonic generator and amplified by an

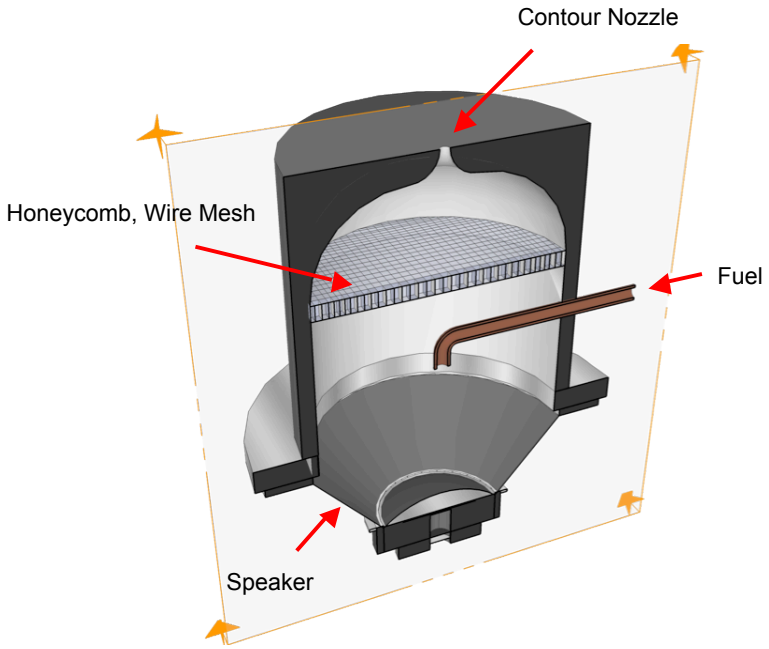

Figure 2.2. Schematic and cross-section of the acoustically pulsed jet apparatus

audio amplifier. The amplified signal was sent through the speaker, which induced pressure fluctuations that modulated the jet fluid. The resulting jet velocity profile was uniform across the exit and had a nearly harmonic flow velocity time variation. The forcing strength or amplitude could be adjusted by varying the voltage amplitude of the signal. The nozzle chamber was supplied with fuel through a metering system consisting of three individual fuel lines. Two lines were metered using flow controllers (Omega FMA-2600 series), and the third line used a combination of a needle valve and a flow meter (Omega FMA-1600 series). The lines were combined into a plenum located between the flow meters and the nozzle chamber, which allowed for various mixtures of both non-premixed and premixed fuels. To prevent backflow between fuel lines, 10 psi check valves were place just downstream of each flow controller or meter. The plenum also served as a dampener for any perturbations that may be induced by the speaker.

The advantage of using a speaker driven system is that forcing strength can be adjusted by varying the amplitude of the harmonic signal. In the current study, the strength of the forcing is defined by the *amplitude ratio*, or the peak-to-mean jet velocity ratio, $U_{j,peak}/U_{j,mean}$. The response of the pulsed jet to the speaker system was determined by measuring the exit velocity of an air jet with a calibrated hotwire. The amplitude ratio is dependent on the voltage amplitude of the harmonic signal, the forcing frequency, and the mean fuel flow rate. Figure 2.3 shows a plot of amplitude ratio with respect to voltage amplitude at several forcing frequencies for a 20 lpm air jet. As voltage amplitude increases, amplitude ratio increases linearly and then saturates once a critical voltage is reached. A forcing frequency of 270 Hz resulted in both the largest attainable amplitude

ratio and the largest amplitude ratio at a given voltage. Figure 2.4 shows the amplitude ratio response at different mean flow rates. As the fuel flow rate increases, the maximum attainable amplitude ratio and the amplitude ratio at a given voltage decrease. For an unsteady JFICF or JICF, a *mean blowing ratio*, r_{mean}, and a *peak blowing ratio*, r_{peak}, can be defined based on the respective mean and peak jet velocities. At a $Re_{j,mean}$ of 3250, the speaker system is able to force the fuel jet at amplitude ratios of up to 4.8, which corresponds to a $Re_{j,peak}$ of about 15,600. The peak Reynolds number, not mean Reynolds number, is a more appropriate measure of the turbulent state. For clarity, test cases for both forced and unforced non-premixed jets are identified by $Re_{j,mean}$ and amplitude ratio.

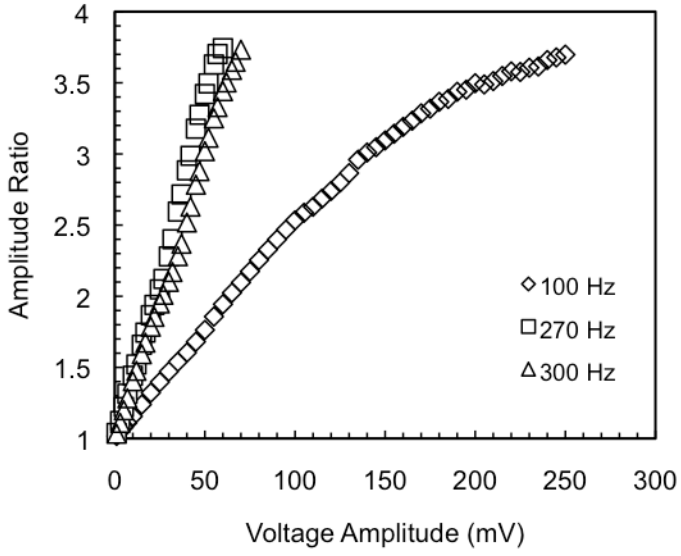

Figure 2.3. Amplitude ratio response of the pulsed jet to the voltage amplitude of the speaker at forcing frequencies of 100, 270 and 300 Hz. Jet flow rate of 20 lpm is shown.

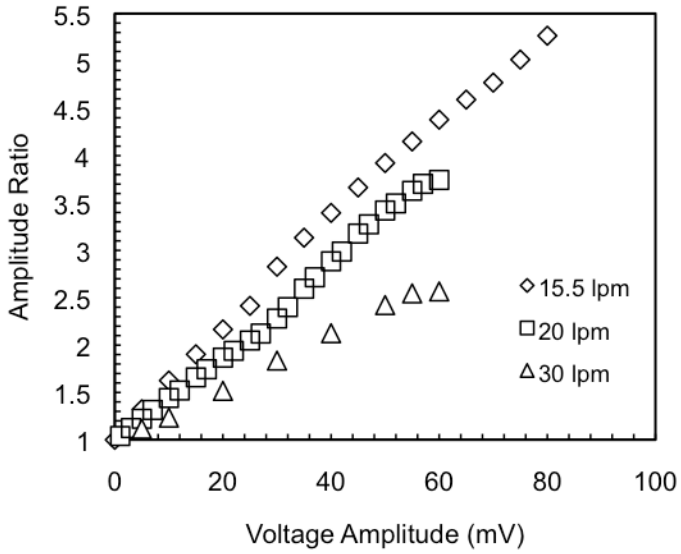

Figure 2.4. Amplitude ratio response of the pulsed jet to the voltage amplitude of the speaker at mean fuel flow rates of 15.5, 20 and 30 lpm. Forcing frequency of 270 Hz is shown.

2.2 EMISSIONS AND FLAME LUMINOSITY MEASUREMENTS

The majority of the experimental techniques employed in the present study are laser-based diagnostics; however, non-laser techniques were also utilized. Simultaneous pollutant measurements of NOx, CO, and UHC were made using three separate gas analyzers—one for each pollutant species. Time-resolved luminosity images were taken using a high-speed camera.

2.2.1 Pollutant Emissions Measurements

NOx, CO and UHC concentrations were measured simultaneously using a chemiluminescent analyzer (Rosemount Analytical model 951A), a non-dispersive infrared (NDIR) analyzer (Rosemount Analytical model 880A), and a hydrocarbon

analyzer (Rosemount Analytical model 400A). The analyzers were calibrated using zero grade air and appropriate span gases—11.06 ppm NO_2 in balance air, 30 ppm CO in balance nitrogen, and 51 ppm CH_4 in balance air. At the specified span gas range, the instrument error was specified by the manufacture as 0.1 ppm for the NOx analyzer, 0.3 ppm (1% of 30 ppm fullscale) for CO, 1 ppm (1% of 100 ppm fullscale) for UHC. The exhaust gas was sampled through an un-cooled quartz probe similar to Drake *et al*. (1987) using a 1/8 HP oil-less diaphragm vacuum pump motor. The sample line was then sent through three rotameters to meter the flow into each analyzer. Each analyzer line was also filtered using 2 μm inline filters. The *L*-shaped probes were made in-house at a glass blowing shop from 6.35 mm O.D. (4 mm I.D.) quartz tubes that were tapered to approximately 1 mm at the tip. The purpose of the taper was to allow the gas to expand, and thus quenching any further reactions in the sample volume. The probe was oriented perpendicular to the exhaust flow and placed far enough downstream (approximately five flame lengths based on the unforced steady JFICF) where water-cooled probes were unnecessary (Drake *et al.* 1987). Radial emission profiles taken at the sample location showed that the combustion products were well mixed, and therefore, single point measurements were sufficient to determine the global emissions. Here, emissions are reported in terms of an emissions index, *EI*, or the grams of emissions species produced per kilogram of fuel burned. In general, *EI* for a particular species is found by measuring both CO and CO_2 (Bandaru and Turns 2000); however, a CO_2 analyzer was not available, and therefore to calculate *EI*, the amount of air dilution must be known. The formal derivation of *EI* is discussed in Section 4.1.1. To ensure that there was no exchange of the

wind tunnel air with ambient air upstream of the sampling location, the wind tunnel outlet was sealed to the inlet of the exhaust hood.

Tables 2.1-2.3 summarize the experimental conditions considered for emissions measurements. Both forced and unforced JFICF at non-premixed and partially-premixed conditions for two fuels—a 70% methane/30% hydrogen blend and propane—were considered. For the forced non-premixed JFICF, the fuel flow rate was held constant and 270 Hz acoustic perturbations were applied to the nozzle chamber. The range of amplitude ratio was limited by the response of the pulsed jet apparatus at the particular fuel flow rate. For the unforced partially-premixed JFICF, the fuel flow rate was held constant and air dilution was added and mixed in the plenum upstream of the pulsed jet apparatus. The maximum amount of air dilution is limited by blowout of the flame.

Fuel	d (mm)	Q_f (lpm)	U_{cf} (m/s)	$\mathrm{Re}_{\mathrm{j,mean}}$	$U_{j,peak}/U_{j,mean}$
70% CH_4/	6.35	20	1.7	3200	1-5.8
30% H_2	6.35	30	1.7	4850	1-3.8
C_3H_8	6.35	10	1.7	7400	1-12.2
	6.35	15.5	2.0	11500	1-7.1

d : jet exit diameter
$\mathrm{Re}_{\mathrm{j,mean}}$: mean jet Reynolds number
$U_{j,peak}/U_{j,mean}$: peak-to-mean jet velocity ratio
U_{cf} : crossflow velocity

Table 2.1. Experimental conditions for forced non-premixed JFICF emissions measurements. The forcing frequency was 270 Hz. For partially-premixed JFICF, fuel flow rate remained constant as air dilution was added. Percent air dilution refers to the percent volume of air in the jet fluid.

Fuel	d (mm)	Q_f (lpm)	U_{cf} (m/s)	Re	% Air Dilution
70% CH_4/	6.35	20	1.7	3200-12300	0-67
30% H_2	6.35	30	1.7	4350-14000	0-57
C_3H_8	6.35	10	1.7	7400-10100	0-71
	6.35	15.5	2.0	11500-14200	0-66
	9.53	10	1.5	4800-8100	0-78

d : jet exit diameter
Q_f : fuel flow rate
Re: jet Reynolds number
U_{cf} : crossflow velocity

Table 2.2. Experimental conditions for unforced partially-premixed JFICF emissions measurements. Fuel flow rate remained constant as air dilution was added. Percent air dilution refers to the percent volume of air in the jet fluid.

Fuel	d (mm)	Q_f (lpm)	U_{cf} (m/s)	$Re_{j,mean}$	$U_{j,peak}/U_{j,mean}$	% Air Dilution
C_3H_8	6.35	10	1.7	7600	1-5.8	50
	6.35	10	1.7	9400	1-3.8	67

d : jet exit diameter
$U_{j,peak}/U_{j,mean}$: peak-to-mean jet velocity ratio
Q_f : fuel flow rate
$Re_{j,mean}$: mean jet Reynolds number
U_{cf} : crossflow velocity

Table 2.3. Experimental conditions for forced partially-premixed JFICF emissions measurements. The forcing frequency was 270 Hz. Percent air dilution refers to the percent volume of air in the jet fluid.

2.2.2 Flame Luminosity Imaging

High-speed imaging of flame luminosity was used to track the flame base of the forced non-premixed JFICF. Although flame luminosity imaging is a relatively simple, integrated line-of-sight technique, it provides a better marker for the flame base than more advanced planar imaging diagnostic. Planar imaging used to mark reaction zones, such as OH PLIF, is not able to capture out-of-plane flame regions and may not

accurately identify the true flame base. Images of the side-view were taken at 10 kHz using a high-speed 512 x 512 pixel CMOS digital camera (Photron Fastcam Ultima APX) and a 50-mm f/1.2 lens (Canon). The camera was placed perpendicular to the flow direction and internally triggered via the camera software—the lack of additional cameras or lasers made external timing circuitry unnecessary. The exposure time, 100 μs, was determined by the 10 kHz frame rate.

Time-resolved luminosity images of forced methane JFICF at $Re_{j,mean}$=4230 and 6340 were taken at amplitude ratios of 4.8 and 3.3, respectively. To phase lock the image acquisition, a 250 Hz forcing frequency was chosen. The crossflow velocity was 1.7 m/s. Methane was chosen because the flame base regions of the methane flames did not soot, and hence filters were not necessary to isolate CH* luminosity from soot luminosity.

2.3 LASER DIAGNOSTIC TECHNIQUES

Laser diagnostics were applied to both the non-reacting JICF and the reacting JFICF at steady and forced conditions. Mixing characteristics of non-reacting JICF were quantified using acetone PLIF. The temporal evolution of JFICF was studied using 5 kHz simultaneous planar laser Mie scattering (PLMS) and CH* chemiluminescence imaging and 5 kHz stereo PIV. In the PIV experiments, evaporation of fog particles (seeded in the crossflow) and pyrolysis of olive oil particles (seeded in the jet) was used to mark the flame. The validity of this approximation was tested using simultaneous PLMS/OH PLIF imaging.

2.3.1 Nonreacting Mixture Fraction Imaging

Mixture fraction imaging of non-reacting JICF was made using acetone planar laser-induced fluorescence. Acetone is a broadband absorber with absorption bands between 225 and 320 nm, and the resultant fluorescence emits between 350 and 550 nm with peaks at 445 and 480 nm (Lozano *et al.* 1992). Acetone has been used as a fluorescent tracer molecule in several jet studies (Smith and Mungal 1998, Tsurikov 2003, Lakshminarasimhan *et al.* 2006). Although, several properties can be measured using laser-induced fluorescence, acetone PLIF is used to image mixture fraction in this study. The fluorescence equation for a single absorbing and emitting species is as follows (Lozano *et al.* 1992):

$$N_e(x,y,t,\lambda) = \int N_i(y,z,t) e^{-\sigma(\lambda)\int C(x,y,z)dx} \sigma(\lambda) C(x,y,z) \phi(T,P,\lambda) dz \qquad (2.1)$$

where $N_e(x,y,t,\lambda)$ is the total number of photons emitted per unit area, $N_i(y,z,t)$ is the incident photon flux, $\sigma(\lambda)$ is the molecular absorption cross-section of the tracer, $C(x,y,z)$ is the concentration of the absorbing species and $\phi(T,P,\lambda)$ is the species quantum efficiency for emission for the particular transition. For acetone (CH_3-CO-CH_3), ϕ is independent of temperature, T, and pressure, P, and can be assumed to be a function of wavelength, λ, only. For an optically thin medium, where absorption is negligible, the emitted photon flux is directly proportional to species concentration of the tracer molecule. For a nonreacting flow, acetone is a conserved scalar, and therefore mixture fraction can be directly related to the concentration, and hence fluorescence signal. In this

study, 2-D phase-averaged and time-averaged mixture fraction, ζ, fields were extracted from the fluorescence images. For the steady and forced JICF, $Re_{j,mean}$ was 4800 and the crossflow velocity was 2.0 m/s (r_{mean}=4.6). The jet was forced at an amplitude ratio of approximately 5.3 ($Re_{j,peak}$=25,000, r_{peak}=24.1). For both steady and forced JICF, ζ is determined by normalizing the image by the image intensity of the steady jet potential core.

Figure 2.5 shows a schematic of the acetone PLIF measurement system. The jet fluid consisted of air seeded with acetone vapor (26% by volume). Air was chosen

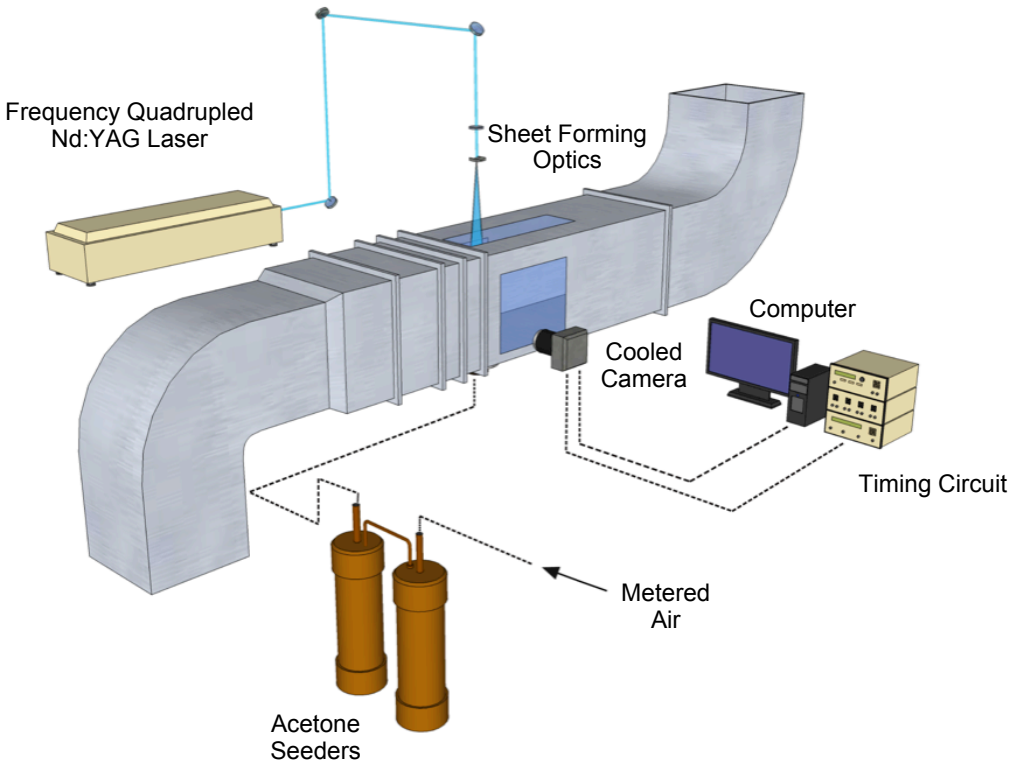

Figure 2.5. Schematic of the crossflow facility setup for acetone PLIF.

because the presence of oxygen quenches the phosphorescence of acetone. The acetone seeder was a multi-stage system designed by Tsurikov (2003) to ensure that the flow exiting the seeder was saturated with acetone vapor. In the first stage, air was injected at the bottom of the acetone reservoir, and effectively acted as a liquid bubbler. Acetone-seeded air was then passed through subsequent stages, which were not filled with liquid acetone. To prevent re-condensation of the acetone vapor, room temperature water was circulated through copper coils in each stage. The acetone molecules were excited by a frequency quadrupled Nd:YAG laser (Spectra-Physics GCR-150), which operated at 10 Hz and emitted approximately 45 mJ/pulse of 266 nm ultraviolet light. The laser was expanded into a sheet using standard sheet forming optics (plano-convex spherical lens and a cylindrical lens) and brought in from the top of the tunnel in order to image the side-view plane-of-symmetry (streamwise-transverse plane). The resultant fluorescence was imaged through a 50-mm f/1.2 lens (Canon) coupled to a cooled, back-illuminated CCD camera (Cyrocam S5) with 512 x 512 pixel resolution. The camera and laser were synced and triggered using a pulse generator (BNC Model 500). To acquire phase-locked images, the camera and laser were triggered at specific time intervals within the forcing cycle. In physical space, the imaging window is approximately 115 x 115 mm^2, or 18d x 18d, where d is the jet diameter. The PLIF images were corrected for background levels, laser sheet non-uniformities and laser absorption. The laser absorption correction followed the Beer-Lambert correction for an expanding sheet detailed by Smith (1996). In this study, the absorption coefficient was found from imaging the potential core of the steady JICF. Details of the correction scheme are referenced in Appendix A. After

applying the correction scheme, the uniformity of the potential core was within 97%. A reasonable estimate of the error introduced by the absorption correction is approximately 3%.

2.3.2 Simultaneous Planar Laser Mie Scattering/CH* Chemiluminescence Imaging

Simultaneous planar laser Mie scattering and CH* chemiluminescence imaging were used to visualize the unsteady nature of forced JFICF. A schematic of this setup is not shown, but is similar to Figure 2.5. The side-view plane-of-symmetry of the flow was illuminated using a high-repetition rate, diode-pumped, frequency-doubled 527 nm Nd:YLF laser (Coherent Evolution-90) operating at 5 kHz that is expanded into a thin sheet. The laser provided 60 W of power, equivalent to about 12 mJ per pulse. Alumina (Al_2O_3) tracer particles were seeded into the jet fuel flow using a fluidized bed and passed through a cyclone separator to separate out only the smallest particles. Alumina particles have a high melting point (about 2300 K) and can to survive the high temperature reaction zone. The seeded jet flow was imaged with a high-speed, 512 x 512 pixel CMOS digital camera (Photron Fastcam Ultima APX). The camera was shuttered down to 10 μs to effectively minimize background flame luminosity.

CH* chemiluminescence was captured using an intensifier (Hamamatsu V6887U) coupled to a second CMOS digital camera. Because the CH* radical emits at a characteristic wavelength of 431 nm, a narrow bandpass filter centered at 430 nm (10 nm FWHM, 40% peak transmittance) was placed in front of the lens to capture only the CH* emission. Images were taken for the CH_4/H_2 forced non-premixed flame cases shown in

Table 2.1. Images were not taken for unforced non-premixed JFICF (both fuels) and forced non-premixed propane JFICF because the 430 nm bandpass filter was unable to discriminate the soot luminosity from the CH* emission. The intensifier frame rate was limited by the phosphor decay rate of 1 kHz. To achieve higher repetition rate (5 kHz) imaging, the intensifier was operated in a continuous mode where the shutter was kept open while the digital camera, shuttered to 50 μs, acquired images. Although this resulted in slight smearing in the luminosity images, the images were sufficient for flow visualization purposes. For CH* chemiluminescence images taken at less that 1 kHz, image smearing was not an issue. Both cameras were synced to the laser and externally triggered using a 4-channel pulse/delay generator (SRS DG535). The PLMS and chemiluminescence images were aligned using commercial imaging software (LaVision DaVis 7.2). Spatial dimensions of the imaging plane were obtained from reference grid images taken with each camera.

2.3.3 Stereoscopic Particle Image Velocimetry

PIV is a common measurement technique used to extract planar velocity fields in fluid mechanics. Technical aspects of the methodology are discussed in Raffel *et al*. (2007). In standard PIV, the flow is seeded with tracer particles and is illuminated twice with two laser pulses within a small time interval (typically on the order of microseconds). Laser scatter from the two laser pulses is captured using a camera on a single frame (single-frame, double-exposure PIV) or subsequent frames (double-frame, single-exposure PIV). Displacement of the particles is determined statistically by dividing the image into smaller regions or interrogation windows and applying an auto-correlation (single-frame) or cross-correlation (double-frame). In-plane velocity vectors are calculated for each window from the measured displacements and the time interval between laser pulses. Stereoscopic PIV extracts the additional out-of-plane velocity component by simultaneously imaging two different perspectives of the same imaging field of view with a pair of cameras. Two-component PIV is carried out with each camera image resulting in two velocity field projections of the same field of view. The out-of-plane component is calculated from the 2-D projections using a geometric reconstruction, where out-of-plane velocities are calculated from knowledge of the exact geometry of the camera setup, or a calibration-based reconstruction, where out-of-plane velocities are determined from calibration of target images. The advantage of calibration-based reconstruction is that it can correct for image distortion and does not require *a priori* knowledge of the exact geometric configuration of the cameras.

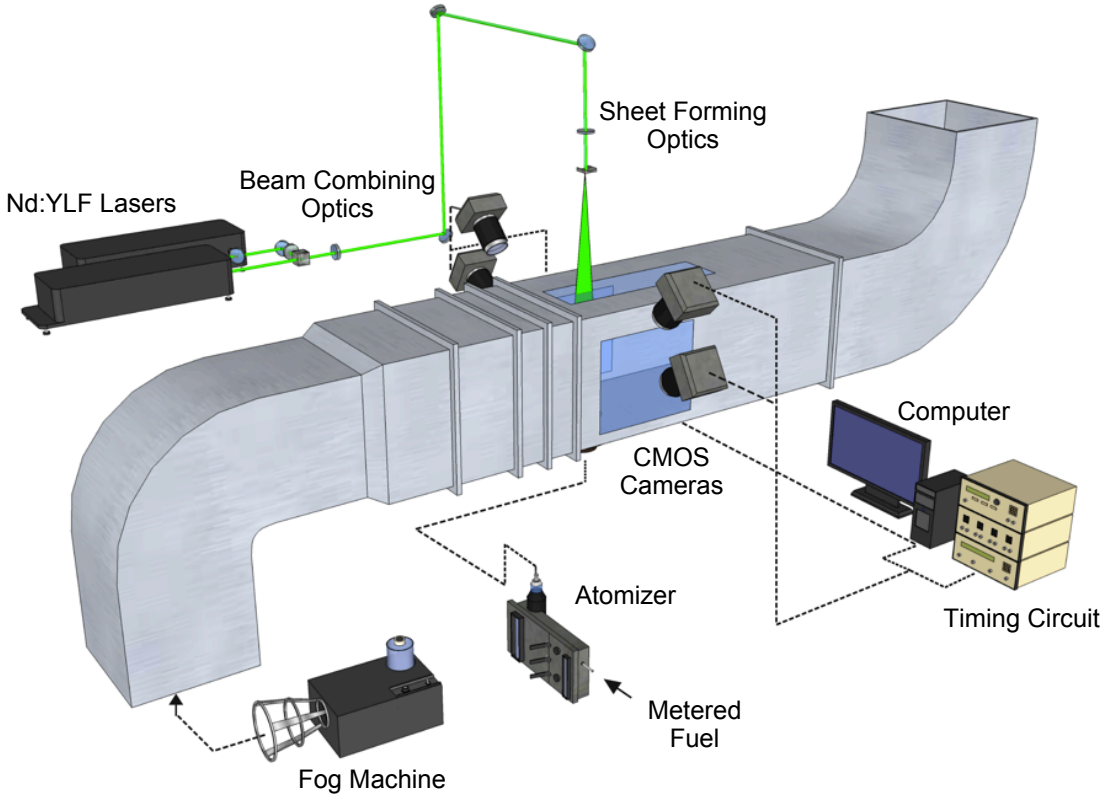

Figure 2.6. Schematic of the crossflow facility setup for stereoscopic PIV.

The stereoscopic PIV system, shown in Figure 2.6, operated in a double-frame, single-exposure mode and was used in previous work described in Gamba (2009). Here, an overview of the system will be presented. The crossflow was seeded using a water-based (glycol) fog machine (Rosco Model 1600) that produced 0.25-60 μm diameter fog particles. Even at the lowest output setting, the fog machine produced enough fog to saturate the crossflow, which prevented individual particles from being discerned. To reduce the fog density, the fog machine was aimed away from the intake of the blower

and allowed to mix with room air prior to entering the crossflow. The jet was seeded using a six-jet atomizer (TSI Model 9306) that generated 0.3 μm diameter olive oil particles placed downstream of the flow meters. The seed density of the fuel jet was varied by turning on and off individual atomizer jets and using a bypass valve to adjust the ratio between unseeded and seeded fuel. Both the glycol fog (boiling point of ~450 K) and olive oil (boiling point of 573 K) are consumed and disappear at sufficiently high temperatures. Although the evaporation temperature is lower than the flame temperature, the disappearance of particles has been used to approximate the location of the flame zone in jet flame studies (Hasselbrink and Mungal 1998, Muñiz and Mungal 1997). Figure 2.7 shows an example of a raw particle image. Note the disappearance of particles in the hot fluid region. An alternative method commonly used in high-speed imaging is to seed the flow with ceramic particles (often alumina) that survive high flame temperatures. In this methodology, the flame location is marked by the abrupt decrease in seed density. Several studies tracked the flame motion by defining isolines where particle density is half the seed density of the 300 K freestream (Steinberg *et al.* 2008, Upatnieks *et al.* 2002, 2004). Assuming that the PIV seed particle density is proportional to the gas density, this isoline corresponded to a 600 K isotherm. Simultaneous imaging with CH PLIF showed that the CH layer typically lies within 2 mm of the 600 K isotherm (Watson *et al.* 1999). This methodology relies on uniform seeding of the flow in order to extract the isotherm accurately. In this study, PIV seeding using alumina particles was attempted, but uniform seeding was difficult to attain—sufficient particle density in the crossflow was difficult to achieve due to the physical size and large flow rate, and uniform seeding

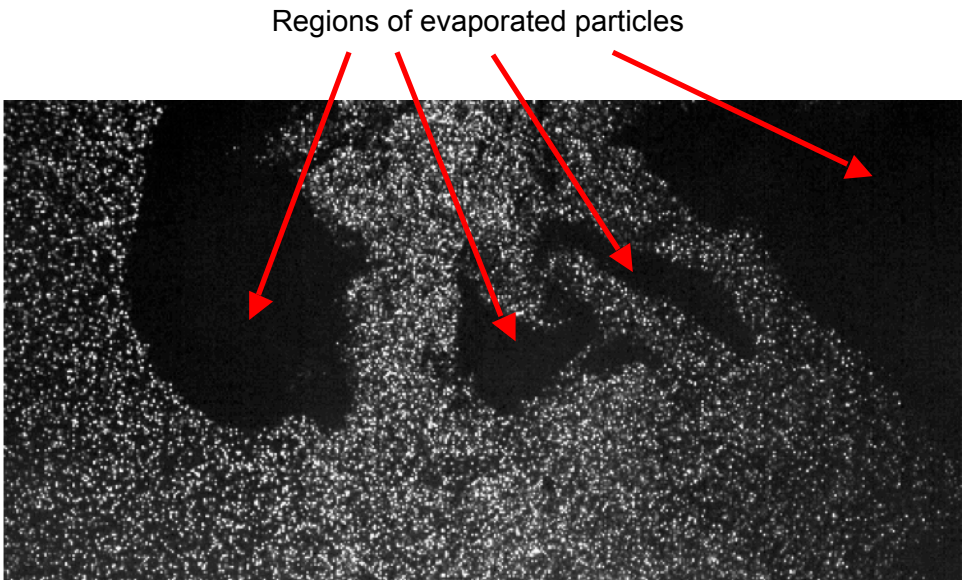

Figure 2.7. Image of the flowfield seeded with fog and olive oil particles. The dark regions where particles have evaporated indicate high temperature regions. Crossflow is left to right.

between jet and crossflow was unable to be maintained due to difficulties in generating consistent seeding. Regardless of seeding method, tracking the flame from both particle seeding techniques has an inherent bias error. In the case of highly wrinkled flames, this bias error may be quite large. Also, recirculation regions of high temperature fluid may lead to incorrect identification of the flame. Therefore, when using particle seeding to mark the flame, care must be taken when interpreting results. In practice, the best method of marking the reaction zone is to use CH or OH PLIF; however, a high-speed PLIF system was not available for this study.

The flow was illuminated using two high repetition rate Nd:YLF lasers (Coherent Evolution). The lasers were the same as those used in the PLMS imaging discussed in

Section 2.3.2. The laser operated at 5 kHz with each providing one of the required laser pulses, *pulse A* and *pulse B*. The beams were combined using a polarizing beam-splitter cube. Normally, a beam-splitter is used to split an incoming beam in to a horizontal-polarized component that passes through the cube and a vertical-polarized component that is reflected 90°. The beam-splitter cube was used in reverse to combine two orthogonally polarized beams—the polarization of *pulse A* was rotated 90° with a half-wave plate—into a single cross-polarized beam. A second half-wave plate was placed after the cube to adjust the polarization angle of the cross-polarized beam so that the scattering signal from both laser pulses were similar. In order to adjust the collinearity of the beams, two laser mirrors were used to direct *pulse A* into the output face of the beam-splitter and provided nearfield (2^{nd} mirror) and farfield (1^{st} mirror) adjustments. Good beam overlap is particularly important in stereoscopic PIV—misalignment can lead to significant loss of out-of-plane velocity correlation. Beam overlap was determined by measuring the beam thickness and location using a knife-edge scanning technique similar to Gamba (2009). Figure 2.8 shows the laser sheet overlap between *pulse A* and *pulse B* at locations corresponding to the top (y=63 mm above the tunnel floor) and bottom (y=25 mm) of the imaging field of view. The laser sheet thickness for each beam, defined as the full-width at $1/e^2$ of the measured laser sheet profile, was approximately 1 mm. The exact measurements are recorded in Table 2.4.

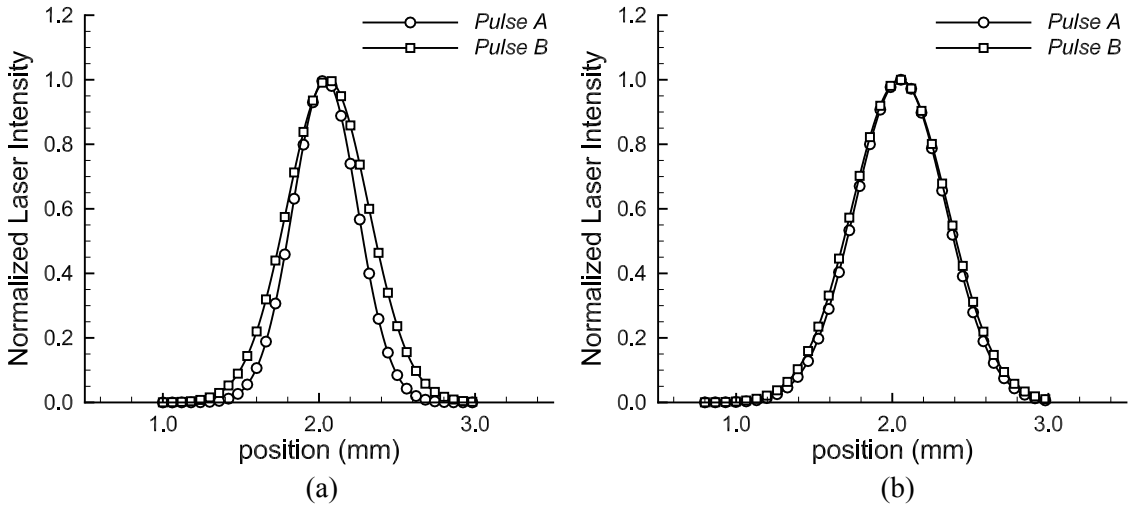

Figure 2.8. Normalized laser sheet intensity profiles for *pulse A* (○) and *pulse B* (□) measured using a knife-edge technique. Profiles were measured at the top (a) and bottom (b) of the imaging field of view. The top and bottom profiles were located y=63 mm and y=25 mm above the tunnel floor, respectively.

Laser Pulse	Top (y=63 mm)	Bottom (y=25 mm)
Pulse A	0.83 mm	1.17 mm
Pulse B	1.05 mm	1.22 mm

Table 2.4. Laser sheet thickness for *pulse A* and *pulse B* measured using a knife-edge technique. Profiles were taken at y=63 mm and y=25 mm above the tunnel floor, which corresponded to the top and bottom edges of the field of view. Sheet thickness is determined by the full-width at $1/e^2$ of the measured laser sheet profile.

Particle images were captured at 10 kHz using four high-speed CMOS cameras (Photron Fastcam Ultima APX)—two sets of stereoscopic camera pairs were used to double the field of view. At 10 kHz, each camera is limited to 512 x 256 pixel resolution, which in physical space corresponds to approximately 50 mm in crossflow streamwise direction, x, and 25 mm in the perpendicular direction, y. Using two camera pairs with a

slight overlap in the *y*-direction, the total field of view was approximately 50 x 40 mm. Both pairs of cameras were fitted with 105-mm f/2.8 lenses (Nikkor) and oriented in a backscattering configuration. A stereoscopic camera pair consisted of a camera on either side of the tunnel angled down toward the floor of the tunnel at approximately 30-35° with respect to the vertical *y*-axis. As discussed in Section 2.3.2, the Nd:YLF lasers emit low energy per laser pulse, and a large aperture was necessary to collect enough light. The byproduct of using a large aperture is a shorter depth of focus, which led to focusing issues when imaging at an angle. Scheimpflug adapters were used to adjust the angle of the lens to focus the image plane properly.

The PIV images were taken in a double-frame, single exposure manner. The images were acquired by frame straddling, where the cameras were triggered at 10 kHz and the lasers were triggered at 5 kHz such that the laser pulses would expose, or "straddle", adjacent camera frames. Although the imaging frame rate was 10 kHz, the PIV acquisition rate was only 5 kHz because *A* and *B* images are taken on consecutive frames. The time delay, Δt, was determined by adjusting the delay between *pulse A* and *B*. Figure 2.9 shows a diagram of the trigger timing. A 4-channel pulse/delay generator (SRS DG535) was used as a 10 kHz master clock, and a frequency divider, made in-house, provided the frequencies required for the lasers (5 kHz) and pulsed jet signal (250 Hz). Initiating recording of the cameras through the software graphical interface was found to introduce delays between the cameras—all four cameras would not begin acquiring images at the same time. Instead, a second pulse/delay generator was used to externally trigger the cameras to begin recording.

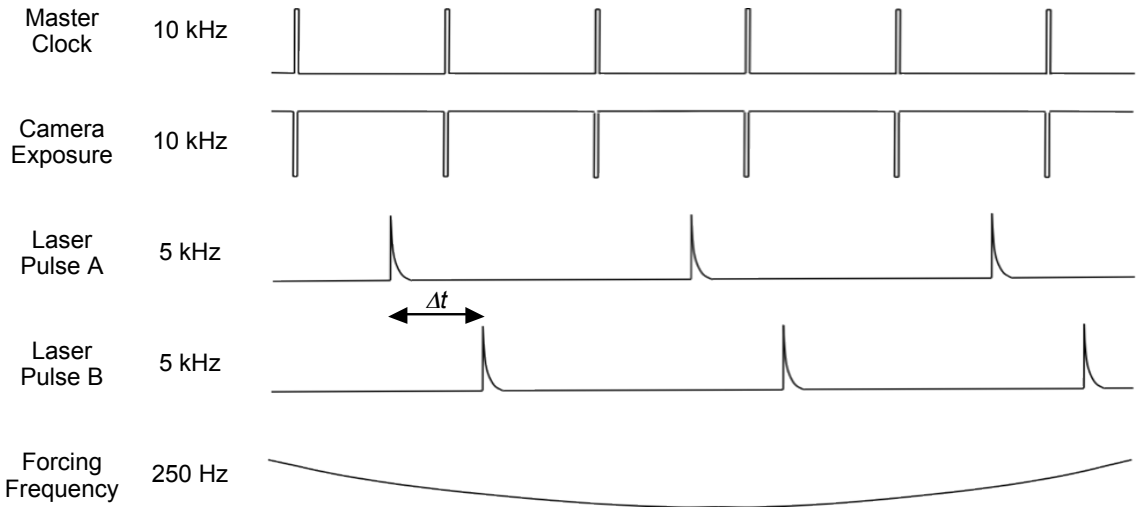

Figure 2.9. Timing diagram of frame straddled, double-frame, single-exposure PIV imaging. A pulse/delay generator was used to initiate the recording for the CMOS cameras. In frame straddling, the time delay between laser pulses, Δt, can be independently adjusted.

Velocity vectors were computed using commercial software (LaVision DaVis 7.2) with an adaptive, multi-grid cross-correlation approach. In this approach, raw particle images were processed using multipass/multistep interrogation from 32 x 32 pixel windows to 16 x 16 pixel windows with 50% overlap. Invalid vectors defined by ratio between the first and second peak correlation were removed for ratios less than 1.2. In general, greater than 97% of the vectors were valid in the crossflow freestream and wake regions; greater than 95% of the vectors were valid in regions near the jet vortical structure. Invalid vectors were removed and replaced using a median filter, and 3x3 Gaussian smoothing was applied in post-processing. The PIV software used a calibration-based reconstruction algorithm to extract the out-of-plane velocity component.

Calibration images were recorded by translating a double-sided target grid along the axis perpendicular to the laser sheet. A self-calibration procedure was applied to reduce bias errors associated with any misalignment between the calibration images and the laser sheet.

Stereoscopic PIV measurements were taken for unforced and forced methane JFICF at $Re_{j,mean}$=6340 and U_{cf}=1.7 m/s (r_{mean}=6.9). The amplitude ratio considered was approximately 3.3 (r_{peak}=30.4), and the forcing frequency was 250 Hz. The total field of view of both camera pairs was too small to image the entire flame base of the forced JFICF; therefore, the windward and lee side were imaged separately. The field of view was large enough to image the unforced flame base because the flame was lifted and stabilized downstream of the jet exit.

2.3.4 Simultaneous Planar Laser Mie Scattering/OH Planar Laser-Induced Fluorescence

As discussed above, extracting the flame base location from seeding images has inherent bias error, which may be quite significant in highly wrinkled flames or recirculation regions of high temperature fluid. In the forced JFICF considered here, forcing induces strong vortex ejections, and interpretation of the evaporation contour may be ambiguous near the vortex region. In order to validate the correlation between the reaction zone and the evaporation contour, simultaneous planar laser Mie scattering and OH PLIF images were taken for forced non-premixed JFICF conditions. A $Re_{j,mean}$=4850

jet in a U_{cf}=1.7 m/s crossflow was considered for a 70% methane/30% hydrogen fuel. The forcing frequency was 250 Hz and the amplitude ratio was approximately 3.7.

Laser-induced fluorescence (LIF) of OH radicals is a laser diagnostic technique that is commonly used to mark reaction zones in flames. Although the OH radical is not immediately quenched outside the reaction zone, the flame can be properly marked by the fluorescence signal if interpreted properly (Donbar *et al.* 2000). In the current study, a tunable dye laser (Lumonics Hyper-Dye 300) pumped by a frequency-doubled Nd:YAG (Spectra-Physics GCR-150) was used to excite the $Q_1(N''=10)$ line of the $A^2\Sigma^+ \leftarrow X^2\Pi$ ($v'=1$, $v''=0$) transition at 284.413 nm. The Nd:YAG provided approximately 300 mJ per pulse at 10 Hz. Rhodamine 590 dissolved in methanol was used as the laser dye medium. The dye laser was tuned to approximately 570 nm and frequency doubled to near 285 nm using a frequency doubler (Inrad Autotracker II) equipped with at KDP type B nonlinear

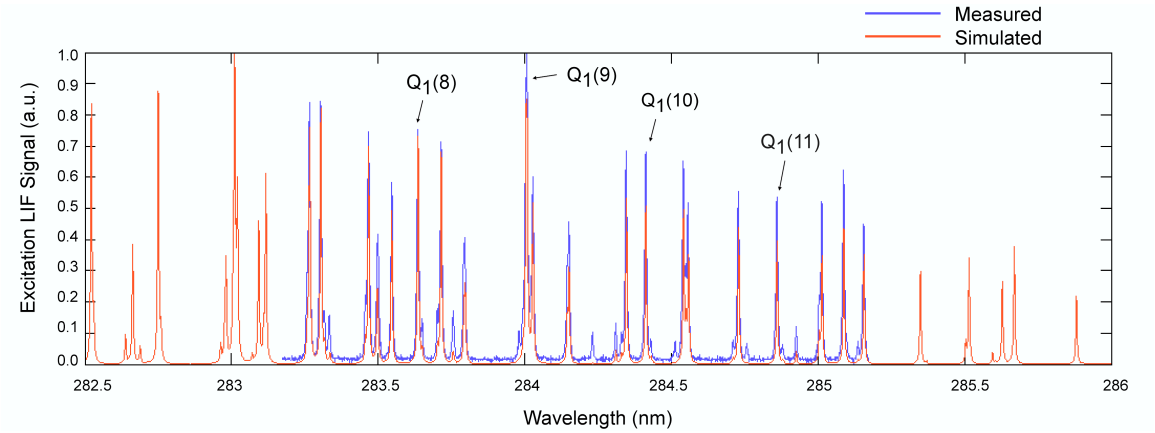

Figure 2.10. Comparison between measured and simulated OH LIF excitation spectrums. The measured and simulated spectrums were aligned by shifting the measured spectrum 0.677 nm to the left. Simulated spectrum was found using LIFBASE[1] software.

[1] LIFBASE is freeware developed by Jorge Luque and is available at http://www.sri.com/psd/lifbase/

crystal. The output energy was approximately 50-60 mJ per pulse at 570 nm and 6-8 mJ at 285 nm. To obtain the wavelength for the $Q_1(N''=10)$ line an OH LIF excitation scan was performed. A laminar methane flame from a Bunsen burner was placed in the UV beam path. As the wavelength was tuned over the range of interest, the resultant broadband fluorescence centered around 308 nm was collected using a PMT. The measured OH LIF spectrum was compared to a spectrum simulated using LIFBASE (Figure 2.10). A 0.677 nm bias was observed between the measured and simulated spectrum.

Figure 2.11 shows a schematic of the PLMS/OH PLIF setup. The crossflow and jet were seeded with fog and olive oil particles in the exact same manner as discussed in the PIV setup in Section 2.3.3. Both wavelengths emitted from the dye laser and doubling crystal were used—570 nm for laser Mie scattering and 285 nm for OH PLIF. The two wavelengths were separated into two beams using a Pellin-Broca prism and directed into the test section along separate paths using wavelength appropriate laser mirrors. Prior to the sheet forming optics, the two beams were recombined using a 285 nm dichroic beam-combining mirror, where the visible beam was transmitted through the mirror and the UV beam was reflected by the mirror. Laser scattering at 570 nm was imaged with a 1008 x 1018 pixel CCD camera (Kodak Megaplus ES 1.0) and a 105-mm lens (Nikkor). The lens consisted of glass elements, which does not pass UV light; therefore, filters were not necessary to block interference from the UV beam or OH fluorescence. OH fluorescence was imaged with a 512 x 512 pixel gated intensified CCD camera (PI-MAX) and an 100-mm f/2.8 UV lens (Eads Sodeern Cerco). UG-11 and WG-295 filters were used to reject

background light from laser scatter from the visible and UV beams. Four sets of images (200 images per set) were taken at equally spaced time intervals within the forcing period. A pulse/delay generator (SRS DG535) was used to trigger the laser and cameras at the appropriate time. The ICCD trigger delay was determined by monitoring the laser pulse using a photodiode. Because the ICCD acquisition rate was the slowest, the ES 1.0 exposure was triggered using the ICCD exposure output in order to acquire both PLMS and PLIF images simultaneously. Image de-warping and spatial alignment were done in the PIV software using target grid images.

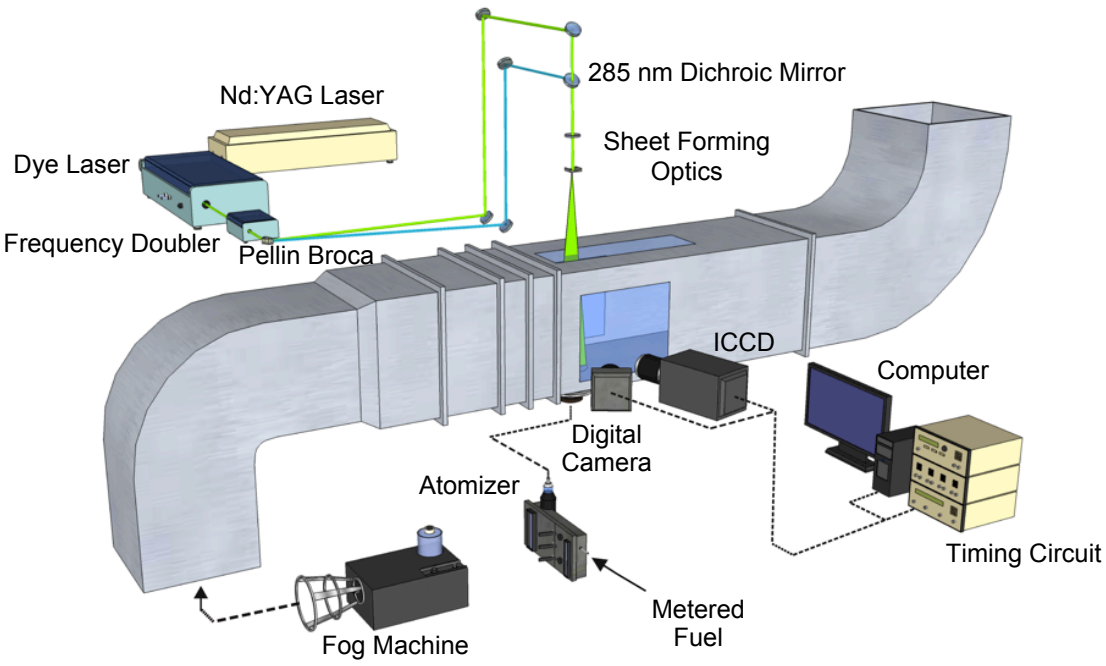

Figure 2.11. Schematic of crossflow facility setup for simultaneous PLMS/OH PLIF.

Chapter 3: Global Effects and Mixing Characteristics

Previous work by Lakshminarasimhan *et al.* (2006, 2007) found that high amplitude forcing led to reductions of flame length and luminosity. These global effects were attributed to enhanced nearfield mixing and in-tube partial premixing of non-premixed fuel and air, which result from the periodic ejection of vortical structures. They concluded that partially premixing of the fuel was the most important mechanism responsible for reductions in flame length and luminosity. Although a relationship between forcing and partially premixing was inferred, a direct comparison between forced non-premixed and unforced partially-premixed flames was not made. Furthermore, the effect of a crossflow was not considered.

This chapter investigates the possible relationship between forced non-premixed JFICF and unforced partially-premixed JFICF by comparing the flame structure and mixing characteristics of forced and unforced flames. A direct comparison of flame luminosity images of forced non-premixed and unforced partially-premixed JFICF is presented. The flow structure of forced JFICF visualized using time-resolved 5 kHz simultaneous PLMS and CH* chemiluminescence imaging is shown. From the CH* chemiluminescence images, flame length and liftoff characteristics are extracted for forced non-premixed JFICF. The latter part of the chapter discusses the mixing characteristics of forced JICF. Mixture fraction fields were measured for the nonreacting JICF using acetone PLIF.

3.1 FLAME LUMINOSITY MEASUREMENTS

Flame luminosity of forced non-premixed and unforced partially-premixed JFICF were imaged using a digital SLR camera (Nikon D80) to investigate the effects of forcing and air dilution on the flame structure. The flame conditions are the same as the experimental conditions for pollutant measurements summarized in Tables 2.1 and 2.2. Figure 3.1 shows images of visible flame luminosity taken with a 1/15 s shutter and f/4 aperture at increasing amplitude ratios and increasing air dilution for 70% CH_4/30% H_2. Forced non-premixed flames at a $Re_{j,mean}$ of 4850 are shown on the left. Unforced partially-premixed flames are shown on the right. The flames have a constant fuel flow rate, and hence constant heat load. Compared to the unforced non-premixed flame, the forced non-premixed flames are less luminous and blue in color indicating a reduction of soot. Similar trends were observed in forced axisymmetric non-premixed jet flames (Lakshminarasimhan *et al*. 2006). Soot reduction is primarily due to the increased oxygen from in-tube partial premixing and enhanced mixing associated with the forcing (Lakshminarasimhan *et al*. 2006, 2007). Forced non-premixed flames also exhibit shorter flame lengths compared to the unforced non-premixed flame. Amplitude ratio, and hence *L/d*, also affects the lifting characteristics of forced JFICF. At lower amplitude ratios, an extinction region develops in the near region of the jet flame on the windward side, while the flame remains attached on the lee side. As the amplitude ratio increases, the flame becomes more compact and fully lifts. The asymmetric lifting is attributed to the presence of the crossflow, where a low momentum wake exists behind the jet. Forced

axisymmetric non-premixed flames, where a crossflow is not present, do not exhibit asymmetric lifting and are always fully lifted (Lakshminarasimhan *et al.* 2006).

Previous studies have suggested that forced non-premixed flames take on partially premixed characteristics (Oh and Shin 1998, Lakshminarasimhan *et al*. 2006, 2007). Figure 3.1 also shows flame luminosity images of unforced partially-premixed JFICF as air dilution increases for 70% CH_4/30% H_2. The percent air dilution is determined by the ratio of the volumetric flow rate of air to the total volumetric flow rate of fluid exiting the jet. Similar to increasing forcing, increasing air dilution results in shorter visible flame lengths and reduced luminosity. The unforced partially-premixed JFICF with 50% dilution shows a similarity to the forced non-premixed JFICF at an amplitude ratio of 3.7—both flames are completely blue in color and asymmetrically lifted. Likewise, the unforced partially-premixed JFICF with 25% dilution is similar to the forced non-premixed JFICF at an amplitude ratio of 2.1, where the flame base is blue, but the tip is yellow; however, the difference between the forced flame (amplitude ratio of 2.1) and the partially-premixed flame (25% dilution) is the breadth of the luminous zone for the forced flame near the wake region behind the JFICF. This difference is likely associated with the vortex mixing mechanism that exists for forced flames. Similar trends are observed for propane JFICF shown in Figure 3.2. Note that larger amplitude ratios can be reached for propane JFICF compared to CH_4/H_2 JFICF because the fuel flow rate is lower for the propane flames. For propane JFICF, larger amplitude ratios and air dilution are required for the flame to be completely blue in color because propane produces more soot than CH_4/H_2.

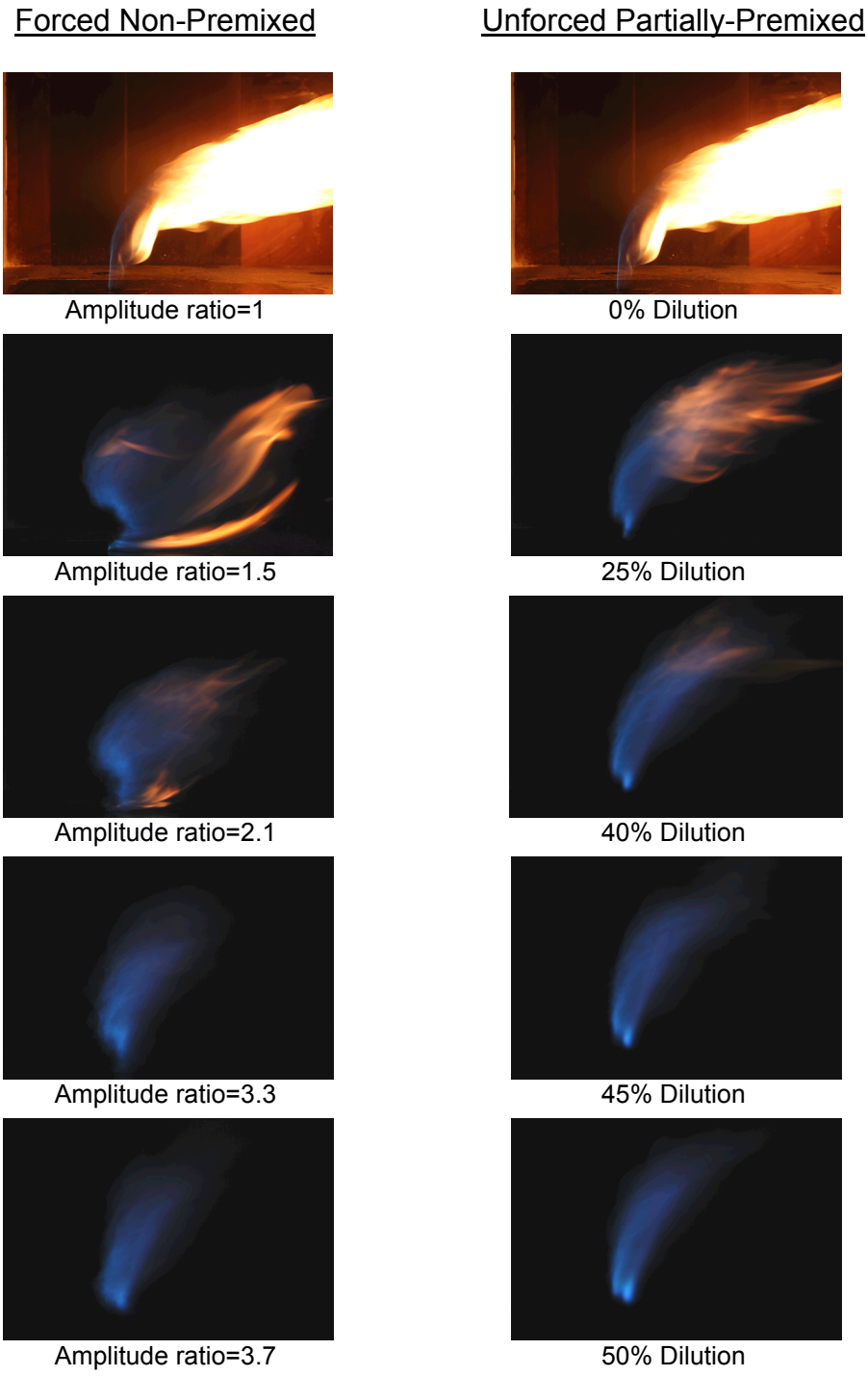

Figure 3.1. Visible flame luminosity for $Re_{j,mean}$=4850 forced non-premixed (*left*) and Q_f=30 lpm unforced partially premixed (*right*) JFICF for CH_4/H_2. The unforced non-premixed JFICF (amplitude ratio=1, 0% dilution) is shown at the top of both columns. Fuel flow rate of CH_4/H_2 is constant for all images. Crossflow is left to right.

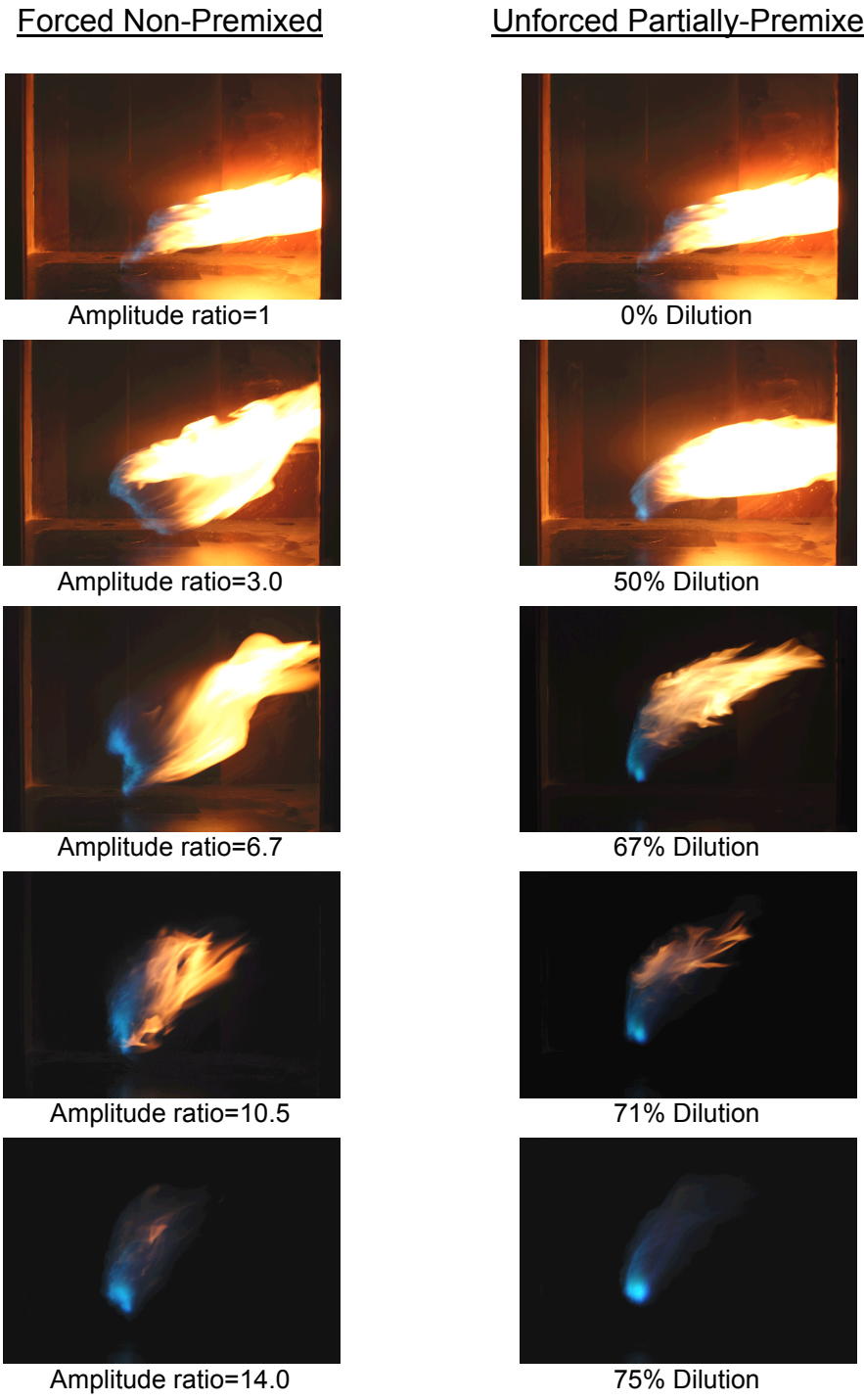

Figure 3.2. Visible flame luminosity for $Re_{j,mean}$=7400 forced non-premixed (*left*) and Q_f=10 lpm unforced partially premixed (*right*) JFICF for propane. The unforced non-premixed JFICF (amplitude ratio=1, 0% dilution) is shown at the top of both columns. Fuel flow rate of propane is constant for all images. Crossflow is left to right.

3.2 SIMULTANEOUS PLMS AND CH* CHEMILUMINESCENCE IMAGES

Simultaneous PLMS and CH* chemiluminescence images were taken to visualize forced non-premixed CH_4/H_2 JFICF at various amplitude ratios for $Re_{j,mean}$=3250 and 4850 flames with a crossflow of 1.7 m/s. Propane JFICF were not imaged because the 430 nm bandpass filter was unable to remove soot radiation completely. PLMS imaging was used to visualize alumina tracer particles seeded into the jet, and CH* chemiluminescence imaging was used to mark the flame.

Figure 3.3 shows a time sequence of PLMS and CH* chemiluminescence images for forced non-premixed JFICF at $Re_{j,mean}$=3250 and amplitude ratios of 4.8. Forced non-premixed JFICF at $Re_{j,mean}$=4850 (not shown) exhibited similar characteristics. Time-resolved images were acquired at 5 kHz; however, for brevity every other image is shown. The flame was forced at a frequency of 250 Hz so that the time interval between images would be equally spaced throughout the forcing period. The phase τ=0 corresponds to the maximum acceleration and zero velocity at the jet exit. The phase τ=0.1, then, corresponds to 0.4 ms later. The white reference contour shown is 15% of the maximum CH* chemiluminescence signal. The image sequence shows an ejection cycle of the vortical structures induced by forcing. The vortical structure issues nearly vertically and penetrates several jet diameters into the crossflow. Although the PLMS images do not give a quantitative measure of mixture fraction, they do show relative changes. The concentration of seed particles in the vortical structure decreases as air is drawn into the core of the structure, which rapidly mixes with the jet fuel. At later phases (τ=0.8 and τ=0.9), the entire fluid column is relatively uniform and well mixed. Despite

the highly unsteady fluid motion, forcing does not seem to significantly perturb the flame base location—the CH* chemiluminescence contour remains relatively stationary throughout the forcing cycle. OH PLIF imaging of the reaction zone of high-frequency forced axisymmetric non-premixed jet flames taken by Lakshminarasimhan *et al.* (2007) also showed that the flame base remains relatively stationary a few jet diameters downstream of the jet exit. This suggests that global features of high-frequency forced flames are not sensitive to individual vortex ejections, but rather to the integrated effect of vortical structures ejected over multiple forcing periods.

Figure 3.4 shows instantaneous (a-c) and mean (d-f) PLMS and CH* chemiluminescence images of forced non-premixed JFICF at $Re_{j,mean}$ of 3250 at amplitude ratios of 2.7, 3.7 and 4.8. The instantaneous images are taken at a vortex ejection phase ($\tau \approx 0.3$), and mean images are an average of 1638 sequential instantaneous images. The CH* chemiluminescence contours reveal significant differences in the flame characteristics. At an amplitude ratio of 2.7 (Figure 3.4a,d), the trailing column's vertical momentum is sufficiently low and jet fuel is convected downstream in the jet wake, which results in an attached reaction zone on the lee side of the nozzle. As amplitude ratio increases to 3.7 (Figure 3.4b,e), the trailing column's vertical momentum increases and the column fluid penetrates deeper into the crossflow causing the lee side of the flame to lift. The lee-side liftoff height, however, is lower than the windward-side liftoff height resulting in an asymmetric lifted flame. As amplitude ratio increases further (Figure 3.4c,f), the lee-side flame liftoff height increases and approaches the windward-side liftoff height. For fully lifted flames, the nearfield region of the jet is exposed to the

crossflow, which allows seed particles to be convected downstream without passing through a reaction zone.

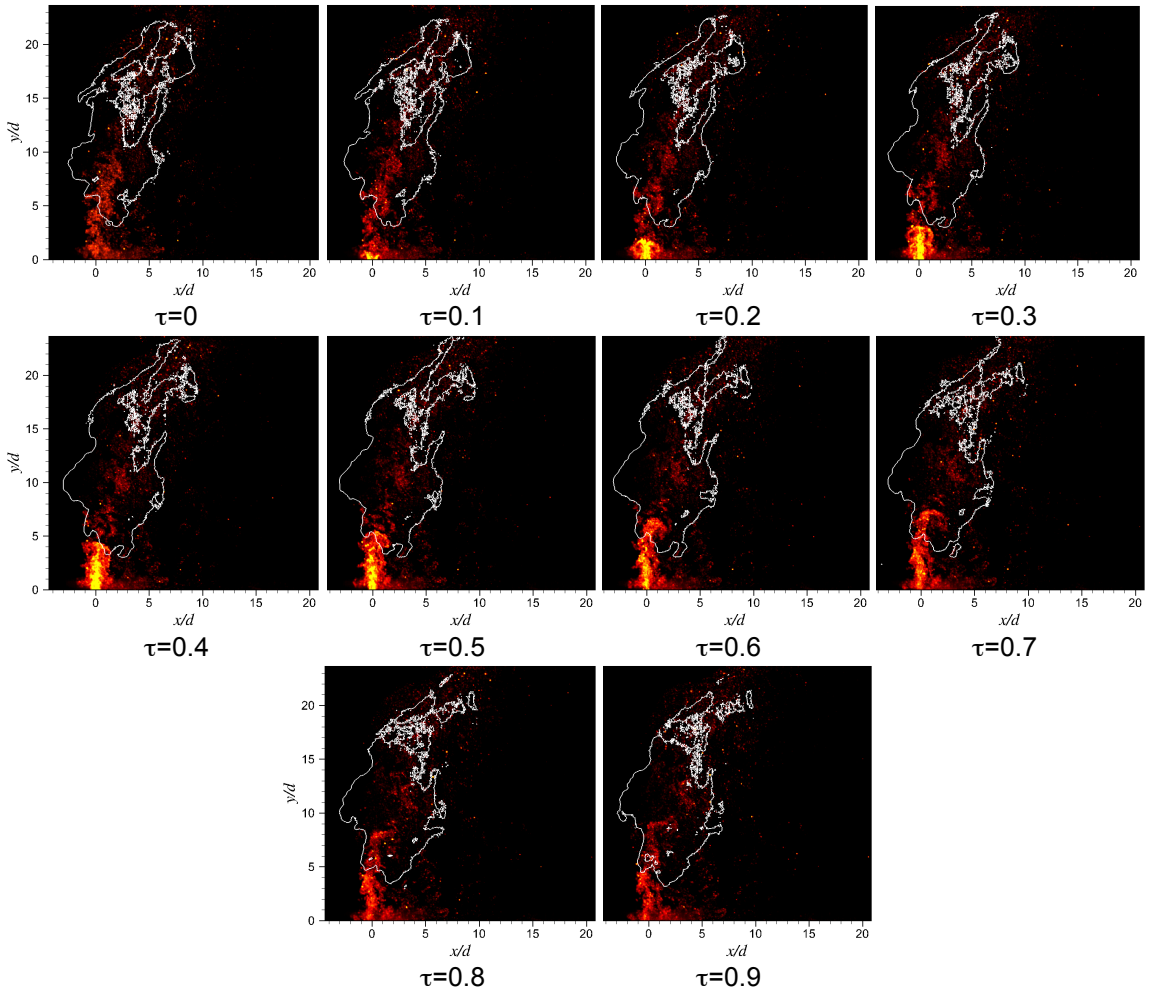

Figure 3.3. Time sequence of PLMS/CH* chemiluminescence images for a $Re_{j,mean}$=3250 forced non-premixed JFICF at an amplitude ratio of 4.8. Fuel jet is imaged by PLMS technique. The 15% maximum CH* chemiluminescence contour is shown in white. At τ=0, the acceleration at the jet exit is a maximum and the exit velocity is zero. Crossflow is left to right.

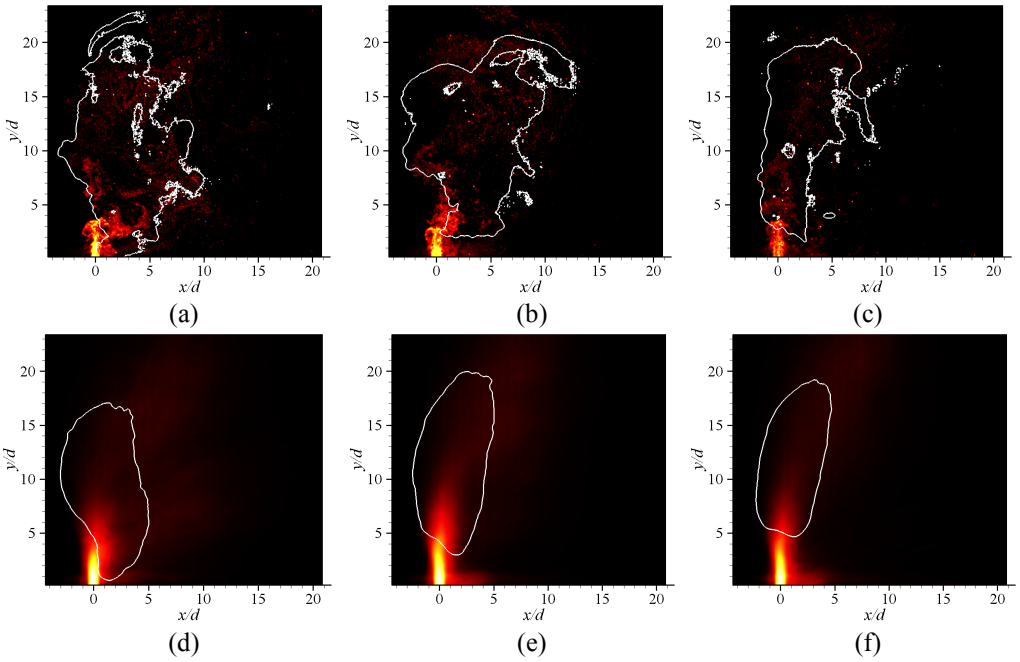

Figure 3.4. Instantaneous *(top)* and mean (*bottom)* flame structure and flow visualization of $Re_{j,mean}$=3250 forced JFICF at amplitude ratio of 2.9 (a,d), 3.7 (b,e) and 4.8 (c,f). Instantaneous images (a-c) are taken at τ=0.3 Fuel jet is imaged by PLMS technique. The 15% maximum CH* chemiluminescence contour is shown in white. Crossflow is from left to right.

Nine additional mean CH* chemiluminescence images were taken at amplitude ratios between 1.9 to 5.7 at both $Re_{j,mean}$=3250 and 4850. Figure 3.5 shows flame lengths and windward and lee-side flame liftoff heights measured from mean CH* chemiluminescence images plotted with respect to L/d. The flame length, l_f, is determined by the maximum straight-line distance between the jet orifice and the 15% maximum luminosity contour, the windward-side liftoff height, $h_{lift,wind}$, is the vertical distance from the flame base, also defined by the 15% maximum luminosity contour, to the upstream edge of the jet orifice, and the lee-side liftoff height, $h_{lift,lee}$, is determined from the downstream edge of the jet orifice. As L/d increases, flame length and windward-side

liftoff height show a relatively flat trend; however, lee-side liftoff occurs at an L/d>20, which is analogous to the boundary between the *turbulent puffs* and *vortex rings with trailing column* flow regimes found in forced JICF. This asymmetric lifting is a unique characteristic of the crossflow configuration. At lower amplitude ratios (low L/d), the wake region behind the jet stabilizes the flame. As amplitude ratio increases, strain rates due to the vortical ejections become strong enough to lift the entire flame base.

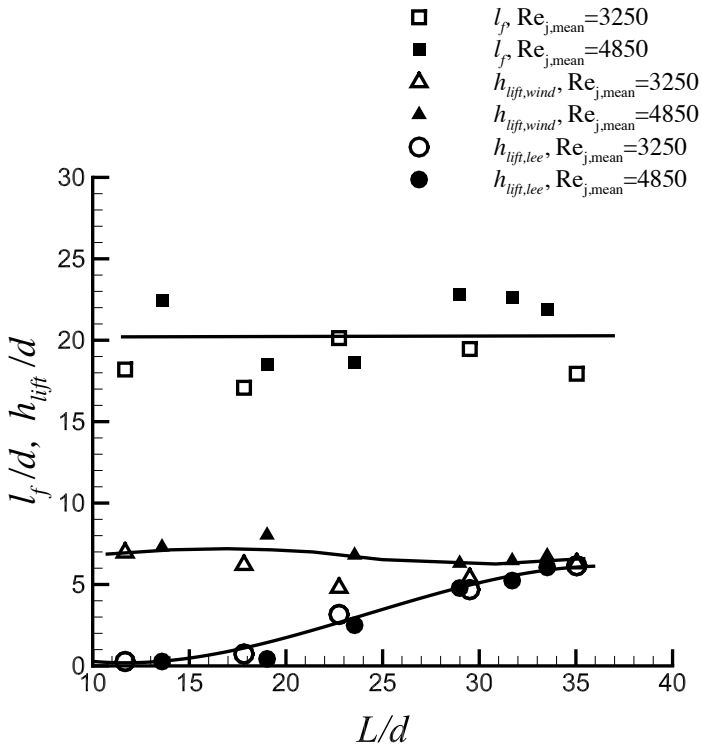

Figure 3.5. Flame length and liftoff height for forced 70% CH_4/30% H_2 JFICF at $Re_{j,mean}$=3250 and 4850 plotted with respect to stroke ratio, L/d. Flame length (*squares*), windward liftoff height (*triangles*) and lee liftoff height (*circles*) are determined by the 15% CH* chemiluminescence contour.

3.3 NONREACTING MIXTURE FRACTION FIELDS

PLMS/CH* chemiluminescence images show that vortical structures ejected during the forcing cycle influences the mixing characteristics of the forced non-premixed JFICF. Quantitative measurements of seed particle concentration cannot be extracted from the PLMS images because of non-uniformities in the jet seeding. In order to quantify the effects of forcing on the nearfield mixing, acetone PLIF was used to image nonreacting JICF at forced and unforced conditions. Because the flame is lifted or partially lifted at the forcing conditions considered, the nearfield mixture fraction fields of nonreacting forced JICF can provide valuable insight in to the mixing characteristics upstream of the flame base for the reacting case.

3.3.1 Acetone PLIF Image Corrections

In order to extract quantitative mixture fraction fields from acetone PLIF images, a series of image corrections must be applied. Detailed steps of the correction procedure are discussed in Appenidx A. Here, a brief overview of the correction scheme is discussed.

As discussed in Section 2.3.1, acetone vapor was seeded into the jet and excited with a 266 nm laser pulse, and the resultant fluorescence was captured using a cooled, back-illuminated camera. Because the fluorescence signal is directly proportional to the concentration of acetone, mixture fraction can be directly extracted from the PLIF images in an isothermal flow; however, several corrections are necessary to reduce measurement uncertainty. First, to reduce background scattering from walls and windows, background

images were subtracted from the fluorescence images of the jet. Background images were taken with the laser running and the crossflow on, but with no jet flow. Second, a laser sheet correction was necessary to correct for non-uniformities in the laser sheet. The laser sheet correction image was acquired by placing a sealed cell with trace amount of acetone in the test section of the tunnel. The camera exposure was set to one second and acquired ten laser pulses per image. Background images with the cell evacuated of acetone were also taken in the same manner and subtracted from the sheet images. Twenty-five sheet images corrected for background were averaged to obtain the laser sheet correction image. The background-corrected jet images were then divided by the averaged laser sheet correction image to obtain corrected fluorescence images of the jet. To obtain mixture fraction images, the corrected fluorescence images were normalized by the signal of the potential core at the exit of an unforced JICF. Note that because forced JICF eject partially-premixed fuel, the forced JICF were normalized by the signal of the potential core of the unforced JICF.

The concentration of acetone (26% by volume) was not negligible, and therefore an absorption correction was required to account for laser energy absorbed by the acetone molecules. For collimated laser sheets, the absorption correction is straightforward, where the fluorescence signal can be corrected along ray paths that follow pixel rows or columns of the image. In the current study, the laser sheet was allowed to expand in order to image a larger field of view, and rays were not coincident with pixel rows or columns. The ray paths were determined by placing a comb in the laser sheet path and imaging the acetone cell. The rays were visualized by the shadows that result from portions of the

laser sheet being blocked by the teeth of the comb. Once the ray paths were determined, absorption along the rays was corrected using the correction scheme detailed in Appendix A. The absorption correction scheme follows the Beer-Lambert correction for an expanding sheet detailed by Smith (1996). In this study, the absorption coefficient was found from imaging the potential core of the unforced JICF. After applying the correction scheme, the uniformity of the potential core was within 97%; therefore, a reasonable estimate of the error introduced by the absorption correction is approximately 3%.

3.3.2 Nearfield Mixing Characteristics

Mixture fraction images were extracted from corrected PLIF images of an unforced (amplitude ratio of unity) and forced (amplitude ratio of 5.8) JICF at $Re_{j,mean}$ of 4800. Forced JICF images were acquired in two ways—at specific time intervals within the forcing cycle (phase-locking), and at random intervals throughout the forcing cycle. For phase-locked imaging, the laser and camera were synced to the forcing frequency by sending the 270 Hz forcing signal to a frequency divider, which provided the 10 Hz trigger for the laser. The 10 Hz signal was also used to trigger the camera exposure. The specific time interval, or phase, was determined by delaying the 10 Hz trigger to the laser and camera using a pulse delay generator. For non-phase-locked imaging, the laser and camera triggers were not synced to the forcing frequency, and images were acquired at random phases throughout the forcing cycle. The unforced JICF was also imaged in the non-phase-locked manner. Figure 3.6 shows instantaneous mixture fraction fields obtained from the PLIF images at four phases of the forcing cycle. The phase τ=0 has

been chosen such that the acceleration at the jet exit is a maximum. The phase τ=0.250, then, corresponds to the phase where the jet velocity is a maximum, and τ=0.750 corresponds the minimum jet velocity.

Figure 3.7 shows phase-averaged mixture fraction fields at eight phases of the forcing cycle. Each phase-averaged mixture fraction field is obtained from an average of 100 phase-locked instantaneous PLIF images. The arrows indicate the relative magnitude and direction of the exit velocity. As the vortical structure is initially ejected and convected downstream, the vortex pair entrains ambient air. At τ=0.375, the vortex head leading edge is well mixed and begins to pinch off and separate from the trailing fluid column. The downstream edge of the fluid column then rolls up resulting in two distinct vortical structures. As these vortical structures continue to mix with ambient air, their vertical convection slows. During the next cycle, the ejected vortex ring catches up with the remnants of the vortical structures from the previous period. This interaction between the vortical structures generated at different cycles results in an interesting mixing process where in a very short distance the fluid goes from being fuel rich to uniformly mixed. Furthermore, the ejected fluid is not pure jet fluid—at τ=0.125, the mixture fraction of the ejected fluid is approximately 0.8. During phases toward the end of the cycle, forcing induces reverse flow at the jet exit and draws ambient air into the nozzle. Entrainment of air into the jet nozzle was also observed in forced axisymmetric jets (Lakshminarasimmhan *et al.* 2007).

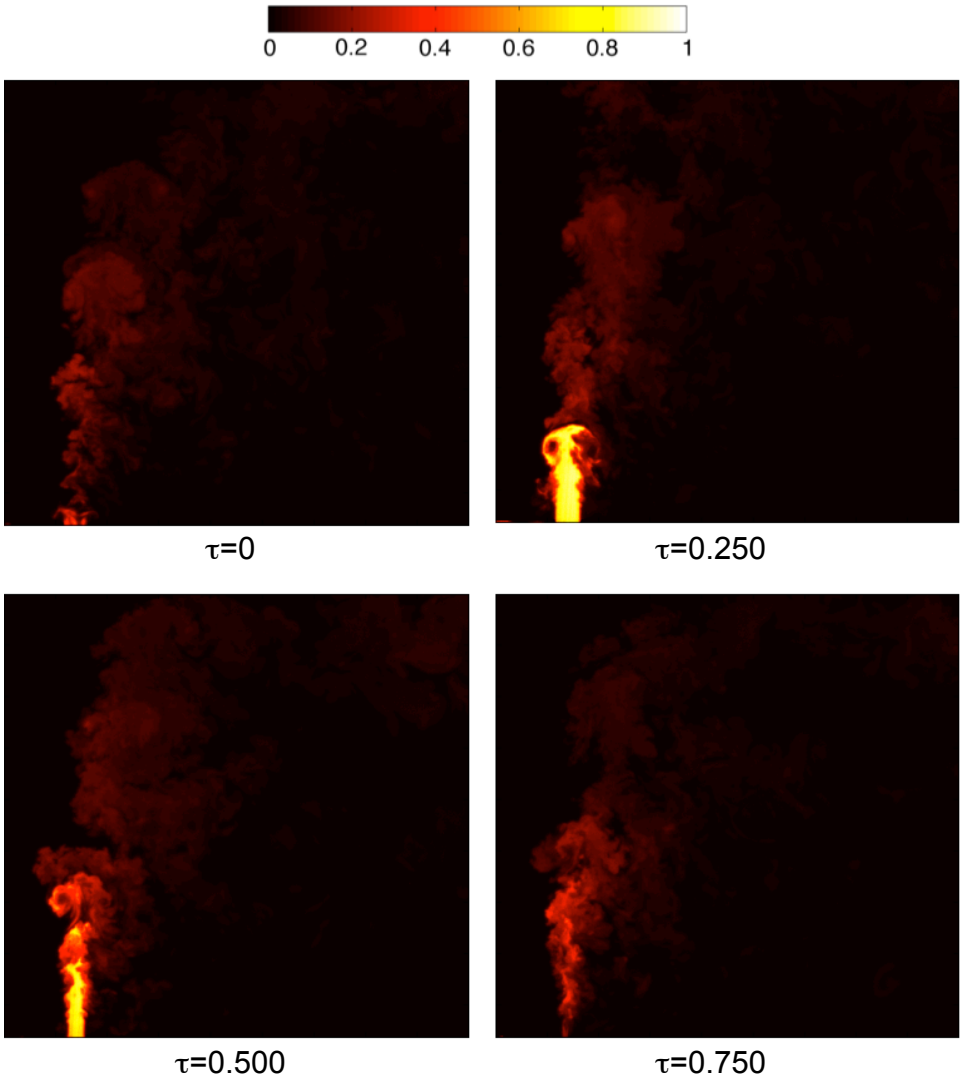

Figure 3.6. Instantaneous mixture fraction field for a forced non-reacting JICF at $Re_{j,mean}$=4800. Amplitude ratio=5.8. The phase, τ, is referenced from the beginning of the sinusoidal exit velocity profile. Arrows indicate relative direction and magnitude of the jet exit velocity. Crossflow is from left to right. Field of view is approximately 18*d* x18*d*.

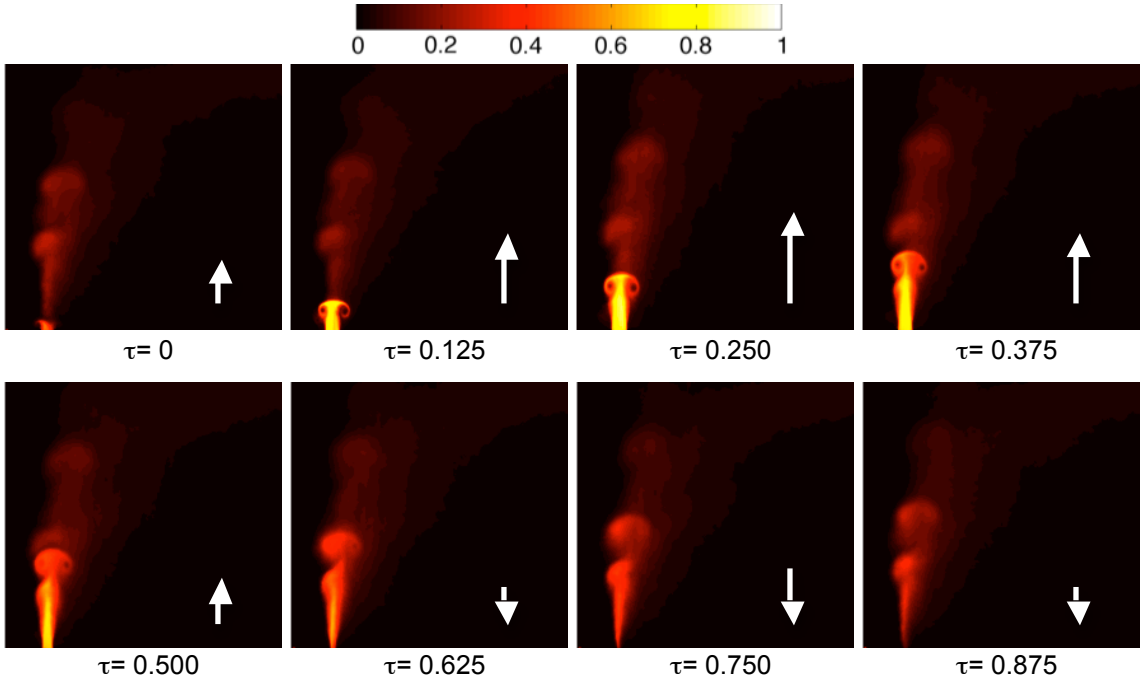

Figure 3.7. Phase-averaged mixture fraction field for a forced non-reacting JICF at $Re_{j,mean}$=4800. Amplitude ratio=5.8. The phase, τ, is referenced from the beginning of the sinusoidal exit velocity profile. Arrows indicate relative direction and magnitude of the jet exit velocity. Crossflow is from left to right. Field of view is approximately 18*d* x18*d*.

From the flame luminosity photographs of the forced non-premixed JFICF, shown in Figures 3.1 and 3.2, and the CH* chemiluminescence images, shown in Figure 3.4, high frequency forcing does not seem to significantly perturb the flame base location. OH PLIF imaging of the reaction zone of high-frequency forced axisymmetric non-premixed jet flames taken by Lakshminarasimhan *et al.* (2007) also showed that the flame base remains relatively stationary a few jet diameters downstream of the jet exit. This suggests that global features of high-frequency forced flames are not sensitive to individual vortex ejections, but rather to the integrated effect of vortical structures ejected over multiple

forcing periods. Figure 3.8 shows time-averaged mixture fraction fields for the unforced and forced JICF obtained from 400 images taken at random phases throughout the forcing cycle. The unforced jet mixture fraction field exhibits the well-defined characteristics of JICF (Smith and Mungal 1998, Hasselbrink and Mungal 2001a). As expected, the mixture fraction in the potential core is uniform (ξ=1), and as the jet penetrates the crossflow and bends, ambient air mixes with the jet fluid and ξ gradually decays. Forced JICF exhibit different characteristics compared to their unforced counterparts. Consistent with previous studies, forcing results in increased jet penetration into the crossflow (M'Closkey *et al.* 2002, Johari *et al.* 1999). Furthermore, unlike the unforced JICF where the mixture fraction in the potential core is unity, the fluid just downstream of the jet exit is partially premixed (ξ=0.65).

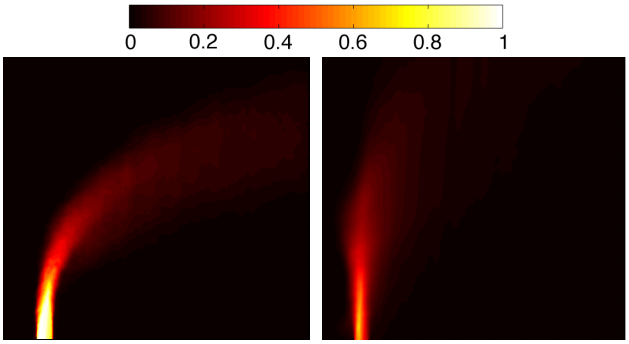

Figure 3.8. Time-averaged mixture fraction fields for $Re_{j,mean}$=4800 unforced JICF (*left*) and forced JICF (*right*) at amplitude ratio=5.3. Crossflow is from left to right. Field of view is approximately 18*d* x 18*d*.

Figure 3.9 shows the jet trajectories extracted from the time-averaged unforced and forced JICF mixture fraction fields. The jet trajectory is determined from the locus of points defined by the maximum concentration along a line perpendicular to the local jet trajectory and extracted from the mixture fraction field using a marching algorithm (Smith 1996). Curve fitting the unforced JICF trajectory points yields power law coefficients of A=1.9 and B=0.36, which are well within the range reported in the literature (Hasselbrink and Mungal 2001a). To determine the trajectory of the current forced JICF, the same marching algorithm used for the unforced JICF was applied. If the forced JICF trajectory is scaled with $r_{peak}d$, the trajectory points show good agreement with the rd-scaled unforced jet suggesting that forced JICF are characterized by r_{peak}. This result may seem counterintuitive because the forced jet is unsteady and the r at a particular phase is always less than or equal to r_{peak}. Mixture fraction images were not obtained at other forcing conditions. To confirm the r_{peak} scaling, multiple forced JICF at various conditions should be considered.

Figure 3.10 shows mean mixture fraction decay along the jet trajectory plotted on a log-log plot for both the unforced and forced JICF. Again, the unforced jet is scaled by $r_{mean}d$ and the forced jet is scaled by $r_{peak}d$. Typically, mean ξ profiles are best plotted with respect to the distance along the trajectory path, s. The trajectory points extracted from the ξ-field are noisy, so a curve is fitted to the trajectory points to enable a more accurate determination of the path length. For the unforced jet, the trajectory follows power law scaling and the curve fit obtained above is sufficient. It is unclear from Figure 3.9 whether the forced JICF follows a power law scaling because the trajectory does not

extend far enough downstream where power law scaling is strictly applicable; however, in the region of interest, a power law fit was found to yield a reasonable trajectory. This curve was found by setting the *B* coefficient to 0.36 (taken from the unforced jet) and iterating on the *A* coefficient until a curve fit was found that was consistent with the previous definition of jet trajectory. The unforced JICF mean centerline mixture fraction was found to decay as $s^{-1.3}$, which agrees with the nearfield decay rate found by Smith and Mungal (1998). For the forced jet, the mixture fraction begins to decay immediately downstream of the jet exit, whereas in the unforced case, it decays only after a few diameters. Furthermore, the forced jet centerline mixture fraction was found to decay at a faster rate of $s^{-2.4}$ indicating that forced jets entrain air at a faster rate than unforced jets. As amplitude ratio decreases toward unity, the entrainment rate is expected to approach the unforced jet rate suggesting that the jet entrainment can be controlled by varying amplitude ratio.

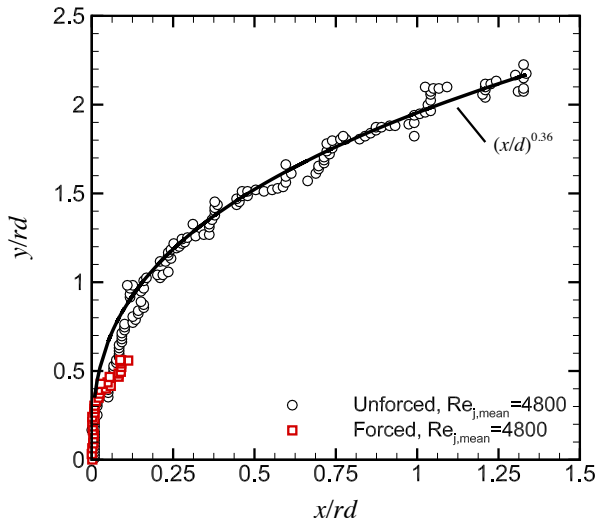

Figure 3.9. Jet trajectory for $Re_{j,mean}$= 4800 unforced JICF and forced JICF at amplitude ratio=5.3. Solid line indicates the power law scaling for the unforced JICF.

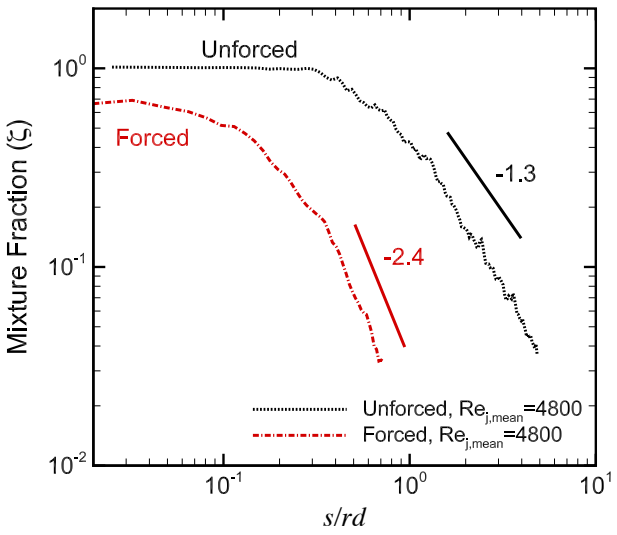

Figure 3.10. Mixture fraction profile along the trajectory path for $Re_{j,mean}$=4800 unforced JICF and forced JICF at amplitude ratio=5.3.

Figure 3.11 shows ζ profiles extracted from the phase-averaged mixture fraction fields. For clarity, only four phases are shown. The phases not shown exhibit similar trends. Mixture fraction is plotted with respect to the path coordinate along the curve fit trajectory found previously from the time-averaged ζ field. The effect of the in-nozzle partial premixing can be clearly seen. Mixture fraction profiles at τ=0.125 and τ=0.375 begin at a mixture fraction of approximately 0.8. The in-nozzle partial premixing observed in this study is significantly less than that found by Lakshminarasimhan *et al.* (2007) in axisymmetric forced jets. Their study considered higher amplitude ratios (approaching seven), which yield stronger reverse flow at the nozzle exit enabling mixture fractions as low as ζ=0.45. Also, in the case of axisymmetric jets, the jet issues into nearly stagnant ambient air compared to the crossflow configuration where the jet

issues into a crossflow velocity field. At τ=0.125 (similarly at τ=0.375) the partially premixed fuel in the vortical head and column encounters the well-mixed state from the previous cycle, which results in a sharp "step-like" decrease in the mixture fraction profile. This "step-like" feature plays an important role in the enhanced mixing characteristics exhibited by the forced JICF. In later phases (τ=0.625, 0.875) the mixture fraction decreases as ambient air is entrained by the vortical structure, and as a result, the step discontinuity is smeared out and the fluid is well-mixed along the entire trajectory. It is not known how the presence of a flame would change the mixture fraction field; however, CH* chemiluminescence images (Figure 3.3) show that the flame tends to stabilize just downstream of the region where vortex head pinches off from the trailing fluid column. Therefore, similar mixing dynamics would be present in the nearfield, resulting in partially-premixed fuel at the flame base.

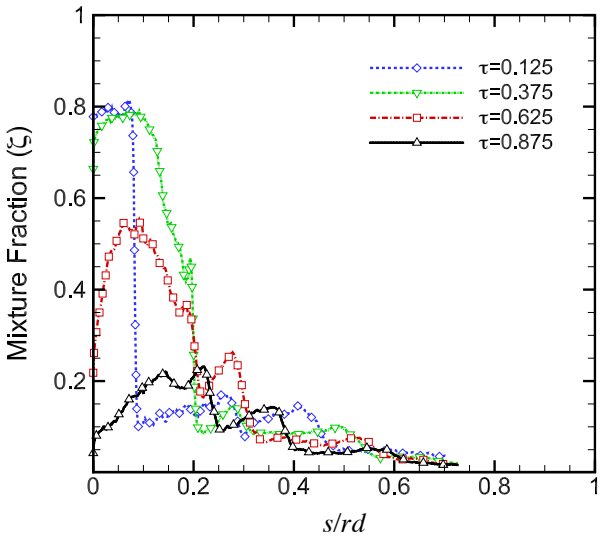

Figure 3.11. Phase-averaged mixture fraction profiles along the trajectory path for a non-reacting forced JICF at $Re_{j,mean}$=4800 and amplitude ratio=5.3. Only four phases are shown.

3.4 SUMMARY

In this chapter, forcing was shown to have significant effects on flame structure and mixing characteristics of JFICF. Several experimental techniques were used to visualize flame and jet structure. From images of visible flame luminosity, forced non-premixed JFICF exhibit similar flame structure to unforced partially-premixed JFICF. As forcing or air dilution is increased, the flame becomes more compact and blue. Time-resolved simultaneous images of the jet visualized by planar laser Mie scattering and the flame marked by CH* chemiluminescence, show that forcing results in periodic ejections of vortical structures, which rapidly mix air and fuel below the flame base. Despite the high frequency forcing, the flame base is relatively stationary a few diameters downstream of the jet exit. Flame length and liftoff heights were measured from CH* chemiluminescence images. Unlike forced axisymmetric non-premixed flames, forced non-premixed JFICF lift asymmetrically, where the windward-side liftoff is higher than the lee-side liftoff. The asymmetric lifting is attributed to the presence of the crossflow.

The partially-premixed character exhibited by forced non-premixed JFICF is the result of rapid mixing in the nearfield of the jet and in-nozzle mixing of fuel and air. Mixture fraction fields of nonreacting JICF show that rapid entrainment of ambient air by vortical structures results in "step-like" ξ-profiles where fluid just downstream of a fuel rich vortex head is well mixed. Also, air is drawn into the nozzle during non-ejection phases of the forcing cycle and mixes with jet fuel in the nozzle, which results in discharges of partially-premixed fluid during ejection phases. Time-averaged mixture fraction fields show that the forced jet is effectively partially-premixed. Mixture fraction

profiles along the jet trajectory show that the mixture fraction of the forced JICF decays faster than that of the unforced JICF.

Chapter 4: Pollutant Emissions

As discussed in Chapter 3, forced non-premixed JFICF appear to take on a partially-premixed character as a result of enhanced nearfield mixing and in-nozzle partial premixing. This chapter investigates this relationship further by measuring pollutant emissions of nitrogen oxides (NOx), carbon monoxide (CO), and unburned hydrocarbons (UHC) for *forced non-premixed* and *unforced partially-premixed* JFICF at experimental conditions summarized in Tables 2.1 and 2.2. Pollutant emissions were also taken for *forced partially-premixed* JFICF conditions summarized in Table 2.3. NOx scaling analysis is presented for forced non-premixed and unforced partially-premixed flames, and NOx formation mechanisms are discussed.

4.1 Pollutant Emissions Indices

Pollutant emissions were measured for non-premixed and partially-premixed JFICF at unforced and forced conditions for CH_4/H_2 and propane. For forced non-premixed flames, the fuel mean flow rate was held constant and forcing was applied at 270 Hz. For unforced partially-premixed flames, air was added to a constant fuel flow rate in a plenum upstream of the nozzle chamber. For forced partially-premixed flames, air dilution was added to the fuel flow rate and forcing was applied. NOx, CO and UHC concentrations were sampled in the center of the exhaust duct well downstream of the flame. At each experimental condition, ensemble averages of six time-averaged measurements were obtained. Each measurement consisted of 4000 samples acquired at

100 Hz. The precision uncertainty of the ensemble averaged measurements is determined by the 95% confidence interval based on a student t-distribution and shown as error bars in Figures 4.1-4.3.

4.1.1 Emissions Index

Pollutant concentrations sampled from the exhaust gas are dependent on the amount of fuel burned in the flame. In order to compare pollutant emissions for different flames, the pollutant concentrations of NOx, CO and UHC are reported as *emissions indices*, *EI*. Emissions index for a species *i* is defined as grams of emissions species produced per kilogram of fuel burned. Because pollutant measurements are made in the post flame exhaust gas, the measured species concentration is affected by ambient air entrained by the jet flame or ventilation system upstream of the sample location—the measured species concentration is the mole fraction of the species in the exhaust gas which includes entrained air. In other studies of hydrocarbon jet flames (Bandaru and Turns 2000, Fregeau and Hermanson 2009), the hydrocarbon fuel is assumed to form CO and CO_2, and *EI* is calculated directly from concentrations of CO and CO_2 measured in the post flame exhaust gas. In the current study, a CO_2 analyzer was not available, and therefore an alternative method of calculating *EI* was used. By conservation of mass, the total mass flow rate of the exhaust gas at the sample location is equal to the sum of the mass flow rate of the jet fluid and the total mass flow rate of air entrained. If the total amount of air entrained is known, *EI* can be calculated directly from the mass fraction of fuel, Y_f, and the species mass fraction, Y_i, and EI_i can be written as

$$EI_i = 1000\left(\frac{Y_i}{Y_f}\right) \quad [g/kg] \tag{4.1}$$

where the constant of 1000 is a conversion factor. Note that Y_f is the mass fraction of fuel of the total amount of fluid entering the exhaust vent, which includes the post combustion gases from the flame and any excess air entrained into the exhaust vent. The wind tunnel exit was sealed to the inlet of the exhaust vent, and therefore the total amount of air entering the exhaust duct was equivalent to the mass flow rate of the crossflow, $\dot{m}_{cf}$. The mass fraction of fuel is calculated by dividing the mass flow rate of fuel, $\dot{m}_f$, by the sum of $\dot{m}_{cf}$ and $\dot{m}_f$. The species mass fraction is determined by dividing the species mole fraction, χ_i, and the species molecular weight, MW_i, by the sum of the mole fraction of each product, χ_j, and their molecular weights, MW_j. Since the mole fractions of the emissions species are much less than the major combustion products, only CO_2, H_2O, O_2 and N_2 are included in the summation of products. In the current study where the tunnel exit was directly connected to the exhaust vent inlet, EI_i for a non-premixed flame is as follows:

$$EI_i = \frac{1000\left(\dot{m}_f + \dot{m}_{cf}\right)\chi_i MW_i}{\dot{m}_f \sum_j \chi_j MW_j} \quad [g/kg] \tag{4.2}$$

For partially-premixed flames, the total mass flow rate includes the mass flow rate of the dilution air in the jet, $\dot{m}_a$; therefore, EI_i for a partially-premixed flame is give by

$$EI_i = \frac{1000\left(\dot{m}_f + \dot{m}_a + \dot{m}_{cf}\right)\chi_i MW_i}{\dot{m}_f \sum_j \chi_j MW_j} \quad \left[g/kg\right] \tag{4.3}$$

4.1.2 Pollutant Emissions Measurements

Figure 4.1 shows NOx, CO and UHC emissions for non-premixed JFICF at varying amplitude ratios (unforced cases have an amplitude ratio of unity). Data are shown for CH_4/H_2 and propane fuels. For CH_4/H_2, NOx emissions decrease as amplitude ratio increases. At an amplitude ratio of 1.5, EI_{NOx} is reduced by about 10% for both $Re_{j,mean}$ of 3250 and 4850. As amplitude ratio is increased further, EI_{NOx} decreases further. At an amplitude ratio of 5.7, EI_{NOx} is approximately 53% lower than the unforced case. For propane, EI_{NOx} initially increases, reaches a maximum and then decreases as amplitude ratio increases. The maximum EI_{NOx} peaks at an amplitude ratio near 6 and is approximately 21% and 35% larger than the unforced case for $Re_{j,mean}$ of 7400 and 11,500, respectively. EI_{NOx} for forced non-premixed propane JFICF does not decrease below EI_{NOx} for the unforced non-premixed JFICF until the amplitude ratio reaches 12. NOx formation is dependent on competing effects—forcing reduces the flame length and residence time for NOx formation, but also suppresses soot, which increases the flame temperature and thermal NOx production rate. To get a reduction in NOx, the amplitude

ratio must be sufficiently large so that the residence time is small enough to overcome the increase in thermal NOx production. Amplitude ratios required to reduce global NOx emissions for propane flames are higher than for CH_4/H_2 because propane produces more soot.

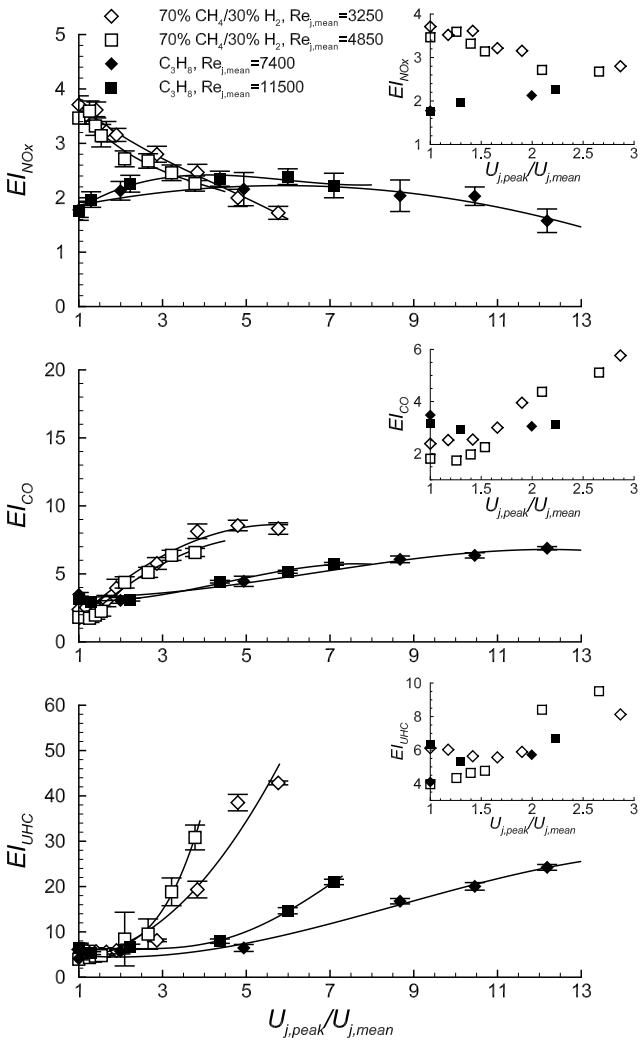

Figure 4.1. NOx, CO and UHC emissions for forced non-premixed JFICF at various amplitude ratios for 70% CH_4/30% H_2 (*open symbols*) and C_3H_8 (*closed symbols*). Inserts on the right show enlarged views of emissions at lower amplitude ratios. The unforced cases have an amplitude ratio of unity.

CO and UHC emissions show a different trend—increasing amplitude ratio results in increasing EI_{CO} and EI_{UHC}. For both fuels, large amplitude forcing can increase EI_{CO} by a factor of 2-3 and EI_{UHC} by a factor of 6-7. At lower amplitude ratios (less than 2 for CH_4/H_2 and less than 5 for propane), EI_{CO} and EI_{UHC} increase only by about 30-40% and 20-30%, respectively. The increase in CO is likely the result of quenching from the rapid mixing of fuel and cold air due to the ejection of intense vortical structures (Hermanson *et al.* 2004). At sufficiently large amplitude ratios, CO emissions saturate once the flame becomes fully quenched. Quenching may explain to some degree the increase in UHC, but a deeper explanation of the UHC evolution requires an evaluation of the flowfield dynamics. A sharp increase in UHC occurs at critical amplitude ratios near 3 for the CH_4/H_2 fuel and 6 for propane. At amplitude ratios greater than the critical value, the flame is fully lifted, which exposes the nearfield of the jet to the crossflow and allows unburned fuel to escape. In the PLMS/CH* chemiluminescence images in Figure 3.4 (b,c,e,f) the flame base is fully lifted and particles seeded in the jet can be seen escaping below the flame. At amplitude ratios less than the critical value, the flame is lifted on the windward side but is attached to the lee side. Figure 3.4 (a,d) shows that a reaction zone envelops the wake region behind the jet, which inhibits the fuel stripping mechanism. El Beherey *et al.* (2005) found that forcing led to decreasing CO and UHC. Interestingly, they noted that CO and UHC were reduced only until the flame detached from the fuel nozzle. In the current work, it would not be possible to achieve the high pulsing amplitudes used by El Beherey *et al.* without significant flame quenching at the base. The difference appears to be that in the study by El Beherey *et al.*, the fuel tube extended into

the crossflow and the wake of the tube acted as a flame holder. It is likely that their configuration could sustain higher strain rates without extinction. In the current study, this lack of stabilization produced a locally extinguished zone where the fluid dynamics drive CO and UHC emissions.

Figure 4.2 shows EI_{NOx}, EI_{CO} and EI_{UHC} for unforced partially-premixed JFICF for CH_4/H_2 and propane fuels. As air dilution increases, EI_{NOx} decreases monotonically for the CH_4/H_2 fuel and non-monotonically—EI_{NOx} first increases then decreases—for propane. These trends are similar to forced non-premixed JFICF because the mechanisms for NOx formation are the same, where shorter residence times compete with higher temperature associated with reduction in soot radiation. Studies of unforced axisymmetric partially-premixed jet flames indicate there is a minimum in the NOx emission index for fuel-air equivalence ratios between 1.5 and 3 (Kim *et al.* 1995, Lyle *et al.* 1999). A local minimum could not be verified for the unforced partially-premixed JFICF considered in this study because jet exit conditions close to the stoichiometric equivalence ratio could not be realized owing to flame blowout. Similar to increasing amplitude ratio in forced non-premixed JFICF, increasing air dilution leads to increased EI_{CO} and EI_{UHC} for CH_4/H_2 and propane fuels.

Emissions measurements were also made for *forced* partially-premixed JFICF. Because forcing and partial premixing are analogous methods for reducing NOx, forcing a partially-premixed flame may yield lower NOx emissions than forcing or partial premixing alone. Figure 4.3 shows the effect of forcing on EI_{NOx}, EI_{CO} and EI_{UHC} for partially-premixed propane-air JFICF with jet exit fuel-air equivalence ratios of

approximately 12 and 24. Indeed, forcing a partially-premixed JFICF leads to lower NOx than forcing a non-premixed JFICF or adding air dilution to an unforced JFICF. At a constant heat load (same fuel flow rate), forcing a partially-premixed propane JFCIF at an amplitude of 5.8 results in NOx emissions that is approximately half as low as the minimum NOx for a forced non-premixed JFICF and 16% lower the minimum NOx for an unforced partially-premixed JFICF. It is important to note that forcing was applied to a partially-premixed flame that has little or no soot loading. Because the maximum amplitude ratio is limited by the forcing system and not flame blowout, it is possible that further increasing forcing may result in even lower NOx emissions. CO and UHC emissions profiles for forced partially-premixed JFICF show similar trends to forced non-premixed JFICF—as forcing increases, CO and UHC also increase—and the magnitude of CO and UHC emissions are similar to CO and UHC emissions from forced non-premixed and unforced partially-premixed flames.

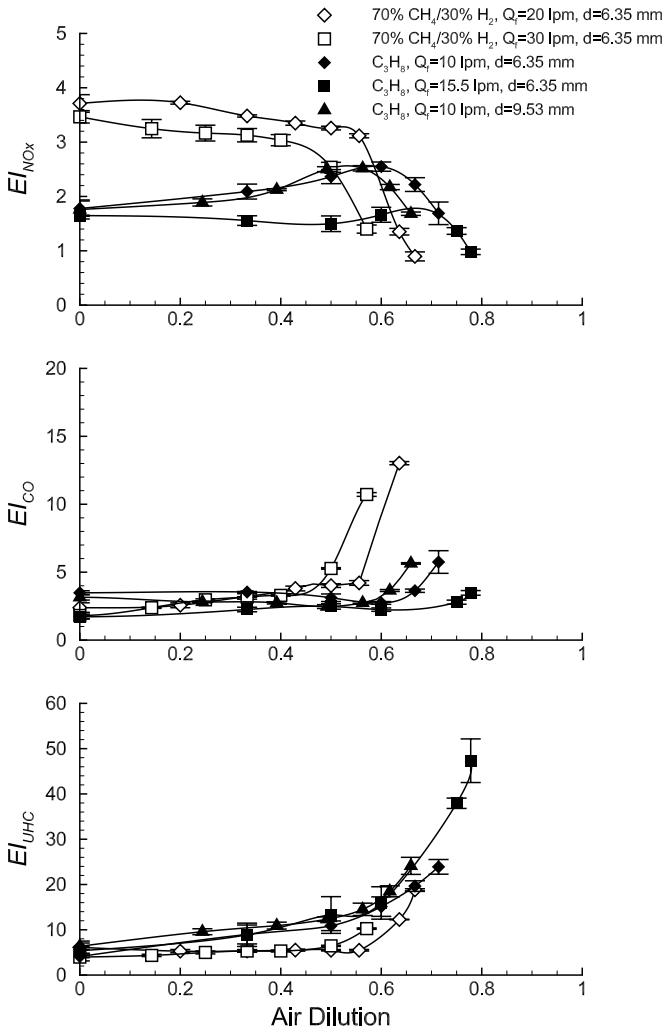

Figure 4.2. NOx, CO and UHC emissions for unforced partially-premixed JFICF at various levels of air dilution for 70% CH_4/30% H_2 (*open symbols*) and C_3H_8 (*closed symbols*). Flow rate of fuel, Q_f, is held constant as air dilution is increased. *d* is the jet exit diameter.

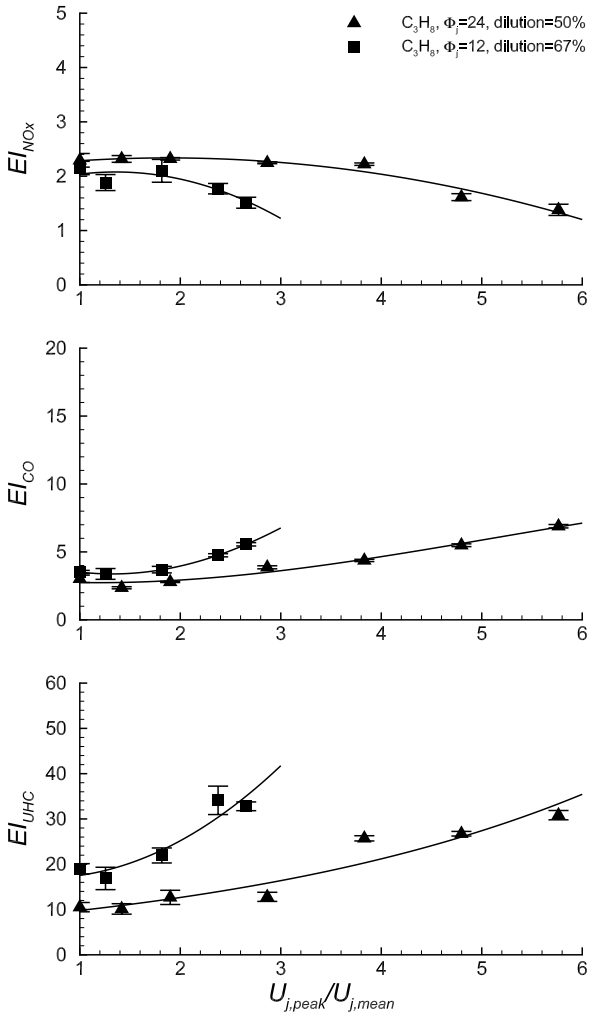

Figure 4.3. NOx, CO and UHC emissions for forced partially-premixed propane-air JFICF at various amplitude ratios for Φ_j=12 (*squares*) and 24 (*triangles*). The unforced cases have an amplitude ratio of unity.

4.1.3 Similarity of Forced and Partially-Premixed Flame Emissions

As discussed above, forcing and partial premixing results in reduced NOx emissions, but at the expense of increased CO and UHC. Because forced and partially-premixed flames have fundamentally different flowfields, comparisons of emissions characteristics based on fluid mechanical properties are difficult to interpret. A more meaningful metric may be to compare flame emissions with respect to a particular pollutant species. For example, the difference in CO trends between forced non-premixed and unforced partially-premixed flames are more easily quantified by comparing flames with similar NOx emissions. To show quantitative comparisons between the emissions characteristics of forced non-premixed and unforced partially-premixed JFICF, plots of EI_{CO} *vs* EI_{NOx}, EI_{UHC} *vs* EI_{NOx}, and EI_{UHC} *vs* EI_{CO} for CH_4/H_2 flames are shown in Figure 4.4. Such comparisons are meaningful when the independent variable—in this case, NOx or CO—can be easily related to forcing or partial premixing. Plots similar to Figure 4.4 are not shown for propane because soot radiation effects complicate NOx emissions, and therefore, EINOx is not a suitable basis for flame comparisons.

For forced non-premixed and unforced partially-premixed CH_4/H_2 flames with comparable NOx emissions, CO emissions are also similar—in fact, when plotted with respect to $EI_{NOx,}$ EI_{CO} is nearly linear and collapses for both flame types—which provides further support that a forced non-premixed flame can be related to an unforced partially-premixed flame. Because both NOx reduction methods increase the strain rate—in the forced case, momentum of the ejected fluid increases and in the partially-premixed case, additional air is added—the residence time for NOx formation and quenching are

inversely related. Interestingly, for flames with similar EI_{NOx}, the peak Reynolds number of the forced non-premixed flame is larger than the Reynolds number of the unforced partially-premixed flame. EI_{CO} is not as large as $Re_{j,peak}$ would suggest because forced flames are unsteady, and high strain rates induced by forcing are not continuously sustained. The effective strain rate is smaller than the peak strain rate and is likely related to the time history of the local strain rate in the flame. Similar to EI_{CO}, EI_{UHC} increases as EI_{NOx} decreases. At large EI_{NOx}, EI_{UHC} for forced non-premixed and unforced partially-premixed flames collapse; however, at EI_{NOx} of approximately 2.5, the UHC emissions from forced non-premixed flames increase sharply, whereas UHC emissions from unforced partially-premixed flames do not. At EI_{NOx} of 2, EI_{UHC} for forced non-premixed flames are nearly four times larger than EI_{UHC} for unforced partially-premixed flames. UHC production is dependent on two mechanism—quenching and flame liftoff conditions. Although the effective quenching for both flames are similar, as suggested by the CO emissions, the larger UHC emissions of the forced non-premixed flame is related to liftoff characteristics. UHC emissions of forced non-premixed and unforced partially-premixed flames diverge at a critical condition where the local strain rate in the nearfield of the jet becomes large enough to lift the flame on both the windward and lee sides. This critical condition is also observed in the plot of EI_{UHC} *vs* EI_{CO}. EI_{CO} is directly related to quenching, which scales with an effective strain rate of the flame, and therefore, the *x*-axis can be interpreted as an effective strain rate. The critical effective strain rate at which the flame lifts is lower for forced non-premixed flames than unforced partially-premixed flames, which leads to additional UHC emission from forced flames.

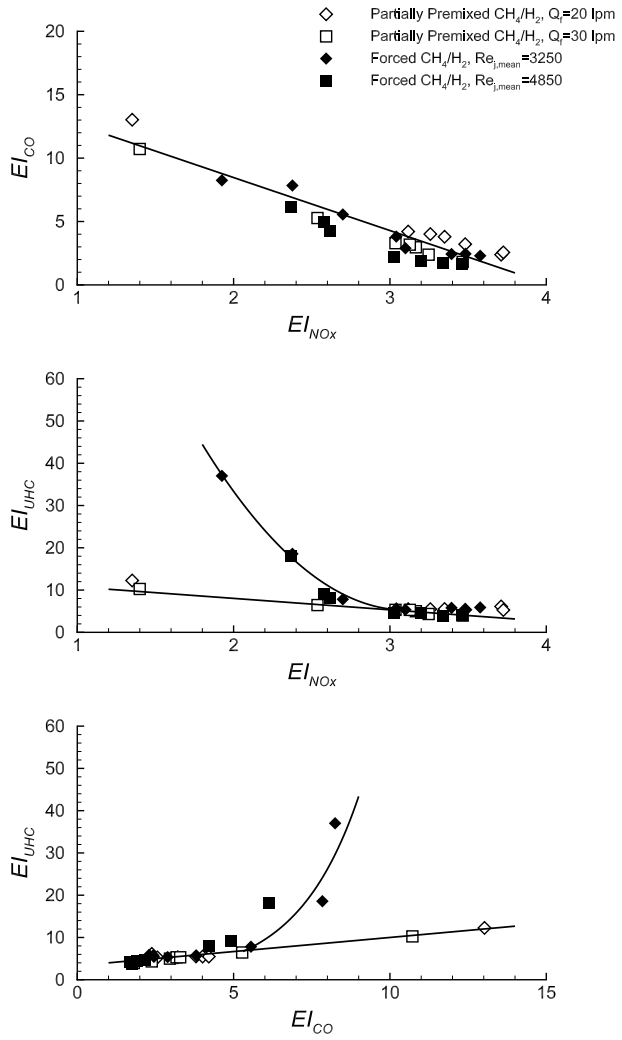

Figure 4.4. Plots EI_{CO} *vs* EI_{NOx}, EI_{UHC} *vs* EI_{NOx}, and EI_{UHC} *vs* EI_{CO} for forced non-premixed (*closed symbols*) and unforced partially-premixed (*open symbols*) 70% CH_4/30% H_2 JFICF.

4.2 NOx Production Mechanisms

NOx, CO and UHC production mechanisms in jet flames have a complex dependence on both fluid mechanics and chemical kinetics. CO and UHC emissions, in particular, are dependent on the quenching and flame liftoff characteristics, which requires detailed velocity and scalar measurements and knowledge of the reaction zone location. The current study does not include these types of measurements, and therefore detailed discussion of CO and UHC scaling is not presented. The role of quenching and extinction in NOx production is less important, and therefore NOx scaling is less complicated. Although a universal NOx scaling law has yet to be proposed, scaling analysis is useful in identifying important NOx mechanisms.

4.2.1 Scaling Analysis

As discussed in Section 1.4.2, simple scaling analysis for NOx emissions results in Eq. 1.6, which is rewritten below:

$$EI_{NOx} \sim \left(\frac{l_f^{\,3}}{\rho_f U_f d^2} \right) \tag{4.4}$$

Recall that the right-hand side of Eq. 4.4 is proportional to $V_f / U_f d^2$, which can also be viewed as the global flame residence time, τ_G.

In most NOx studies, the flame length is a measured quantity; however, for partially-premixed and forced flames, the scaling relationship between premixing or

forcing conditions and flame length is not well developed. Therefore, it is useful to discuss scaling laws in terms of primary jet variables. From self-similarity scaling for axisymmetric nonreacting jets, the mixture fraction scales as

$$\xi(y) \sim \left(\frac{y}{d^*}\right)^{-\beta} \tag{4.5}$$

where the effective diameter, $d^* = \sqrt{\rho_j / \rho_a}\, d$, accounts for the difference in density between the jet fluid, ρ_j, and ambient air, ρ_a, and the constant β is related to the exponential decay of the conserved scalar. For unforced jets, β=1. The flame length scales with the axial position, y, where the mixture fraction is stoichiometric, and therefore the stoichiometric mixture fraction, ξ_s, can be related to l_f as follows (Dahm and Mayman 1990):

$$\xi_s \sim \left(\frac{l_f}{d^*}\right)^{-\beta} \tag{4.6}$$

Similarly, flame length scaling arguments can be applied to unforced partially-premixed and forced non-premixed JFICF. As discussed previously, *rd*-scaling is more appropriate for jet in crossflow configurations (Smith and Mungal 1998); however, increasing air dilution or amplitude ratio results in large momentum ratios—peak momentum ratio in the forced case—that approach the vertical jet limit. For high momentum JFICF, d^*-

scaling would be more applicable and allows for direct comparison to existing axisymmetric jet flame data. Also, the effect of radiant fraction on NOx production is less important because soot has been reduced significantly. Without complications from soot radiation, simple scaling laws should provide a better description of NOx emissions in this high momentum ratio regime. For unforced partially-premixed JFICF where the jet mixture fraction is less than unity, flame length scales with the ratio of the stoichiometric mixture fraction for the particular fuel, ξ_s, and the mixture fraction of the partially-premixed jet fluid exiting the nozzle, ξ_j. Partial premixing of the jet fluid can be accounted for by substituting ξ_s/ξ_j for ξ_s in Eq. 4.6 as follows:

$$\frac{\xi_s}{\xi_j} \sim \left(\frac{l_{f,premix}}{d^*} \right)^{-\beta} \tag{4.7}$$

Note that for a non-premixed jet, ξ_j is unity. The subscript *premix* is appended to l_f to differentiate from the forced case. Eq. 4.7 can be rearranged in terms of $l_{f,premix}$ as

$$l_{f,premix} \sim \left(\frac{\xi_s}{\xi_j} \right)^{-1/\beta} d^* \tag{4.8}$$

For forced non-premixed JFICF, forcing results in the ejection of partial premixed fuel from the jet exit. In forced axisymmetric turbulent flames, Lakshminarasimhan *et al.* (2006) found that reduction in luminous flame length—a direct indication of increased

mixing—is linearly proportional to amplitude ratio. Therefore, it is reasonable to assume that for the forced non-premixed flame, the effective mixture fraction of the fuel exiting the nozzle, and hence ξ_s/ξ_j, can be assumed to have a linear relationship with amplitude ratio as follows:

$$\frac{\xi_s}{\xi_j} \sim \frac{U_{j,peak}}{U_{j,mean}} \tag{4.9}$$

Substituting Eq. 4.9 into Eq. 4.8, the flame length scaling for forced flames, $l_{f,forced}$, can be written as

$$l_{f,forced} \sim \left(\frac{U_{j,peak}}{U_{j,mean}}\right)^{-1/\beta} d^* \tag{4.10}$$

Recall that for unforced jets, β=1. In the forced case, the conserved scalar decays at a higher rate than the unforced jet. The constant β should also be a function of the amplitude ratio, but its value is not well established. For simplicity, β for forced flames is assumed to be a constant. In Figure 3.10, *rd*-scaling shows that for the forced JFICF, mixture fraction scales as $s^{-2.4}$. In the high forcing limit, the trajectory, *s*, approaches the vertical *y*-axis, and therefore a reasonable value for β in Eq. 4.10 is 2.4.

4.2.2 EI_{NOx} Scaling

Figure 4.5 shows EI_{NOx} scaling for unforced partially-premixed JFICF detailed in Eq. 4.4 and 4.8. Note that the NOx scaling in Eq 4.4 is for thermal NOx, and prompt NOx production is neglected. NOx emissions data for axisymmetric partially-premixed jet flames from Turns *et al.* (1993) are also plotted with respect to the scaling parameter $l_{f,premix}$ defined in Eq. 4.8. Simple scaling does not collapse EI_{NOx} for unforced partially-premixed flames for JFICF in this study or axisymmetric jet flames in Turns *et al* (1993). The failure of simple NOx scaling for unforced partially-premixed flames is not surprising—NOx scaling also has been shown to fail for unforced non-premixed axisymmetric jet flames (Turns 1995, Chen and Driscoll 1991, Peters and Donnerhack 1981)—as simple scaling does not account for several NOx production mechanisms, namely flame radiation and nonequilibrium effects. Decreasing air dilution corresponds to increasing l_f and global flame residence time, τ_G. As τ_G increases, residence time for NOx formation increases. At a critical flame residence time, $\tau_{G,crit}$, soot radiation becomes important. For $\tau_G > \tau_{G,crit}$, heat loss to soot radiation reduces thermal NOx, which results in a net decrease in NOx. This radiation effect is most clearly seen in ethylene flames, where increasing air dilution does not decrease NOx because the flame blows out before soot can be sufficiently suppressed. For $\tau_G < \tau_{G,crit}$, soot has been suppressed and the effect of soot radiation is expected to be small. In addition to soot radiation effects, superequilibrium radical (OH and O) concentrations and temperatures contribute to NOx formation, which are neglected in this simple scaling analysis.

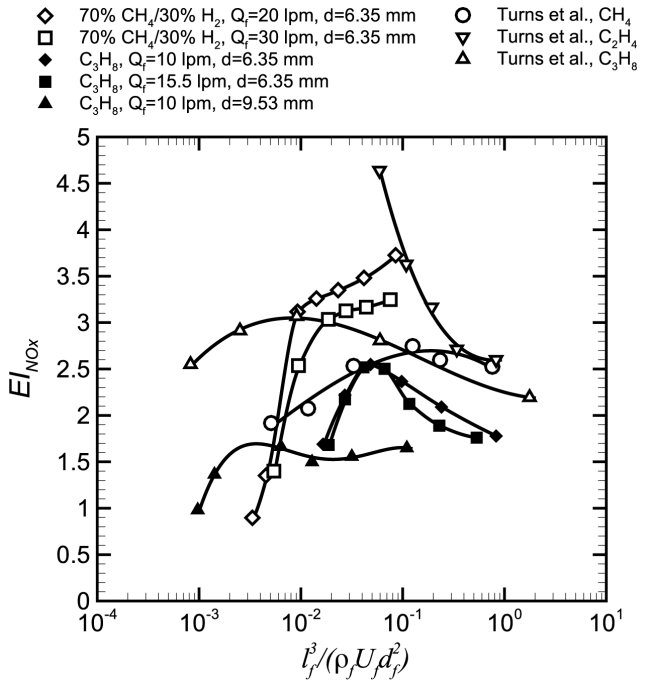

Figure 4.5. EI_{NOx} scaling for unforced partially-premixed JFICF for 70% CH_4/30% H_2 and C_3H_8. EI_{NOx} data for axisymmetric unforced partially-premixed jet flames from Turns *et al.* (1993) are also shown.

Figure 4.6 shows EI_{NOx} scaling for forced non-premixed CH_4/H_2 and propane JFICF detailed in Eq. 4.10. Increasing amplitude ratio corresponds to decreasing l_f, and hence global flame residence time. At small l_f, amplitude ratio is sufficiently high to suppress soot for both fuels. In this regime, NOx production is dominated by flame residence time, and simple scaling is able to collapse EI_{NOx}. At large l_f, simple scaling does not collapse the data because the scaling neglects soot radiation effects. As τ_G increases, EI_{NOx} for CH_4/H_2 also increases, but EI_{NOx} for propane decreases. Propane has a higher propensity to soot than CH_4/H_2, so $\tau_{G,crit}$ for propane would be less than CH_4/H_2. The soot propensity of CH_4/H_2 is so small that NOx monotonically increases as τ_G increases.

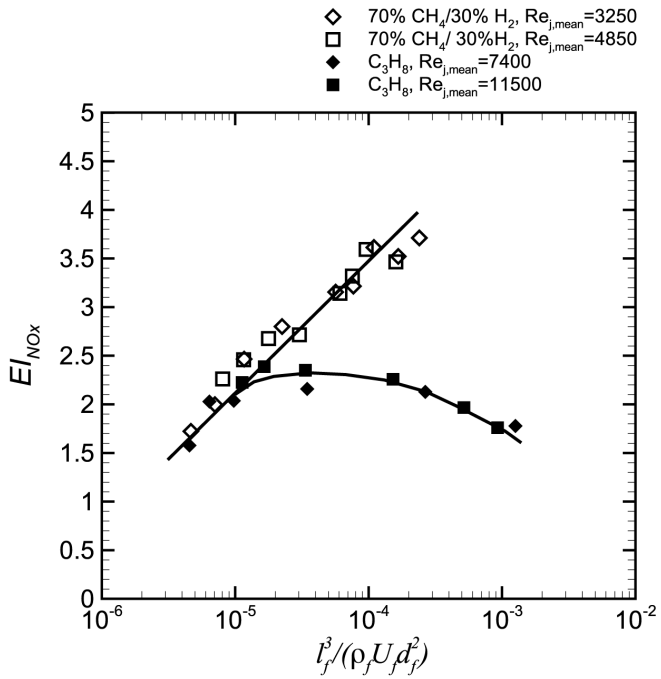

Figure 4.6. EI_{NOx} scaling for forced JFICF for 70% CH_4/30% H_2 (*circles*) and C_3H_8 (*diamonds*).

The success of simple scaling for NOx production in forced flames is rather surprising considering simple scaling fails for unforced partially-premixed and non-premixed flames. Soot radiation is an oft-cited reason for the failure of simple scaling (Turns 1995); however, for unforced partially-premixed flames air dilution is able to suppress soot. A closer look at NOx formation in turbulent jet flames may provide possible explanations for the different scaling behaviors. Figure 4.7a shows a diagram of the flame structure of an unforced partially-premixed jet flame based on the model of Broadwell and Lutz (1998). Their discussion is directed toward non-premixed flames; however, the partially premixed flames in this study are likely to exhibit similar structure because the jet exit fuel-air equivalence ratios are larger than the rich flammability limit.

Broadwell and Lutz observed that although the reaction zone, or flame sheet, is thin, combustion products are not confined to thin regions. Air entrained by large-scale motions mixes with hot products and forms broad high temperature regions downstream of the flame sheet. NOx is not only formed at the flame sheet, but also in these thermal regions. In the downstream region near the flame tip, the flame sheet is drawn toward the jet centerline and broad hot thermal regions, and hence NOx, are more thoroughly distributed throughout the jet volume. In the upstream region of the jet, the flame sheet lies near the periphery. Because the thermal gradients are large, broad thermal regions do not form, and NOx formation is limited to the perimeter of the jet flame. NOx production at the flame sheet can be highly influenced by the global strain rate and superequilibrium radical concentrations (Driscoll *et al.* 1992), which are unaccounted for in simple NOx scaling. Figure 4.7b shows a diagram of the forced flame structure based on simultaneous acetone/OH PLIF images taken by Lakshminarasimhan *et al.* (2007). Acetone seeded into the jet fuel was used to visualize unpyrolized fuel, and OH produced in the flame was used to mark the reaction zone. They found that vortical structures persist downstream despite the presence of the reaction zone. These structures mix entrained air with hot combustion products forming conditions amenable to NOx formation. The resultant NOx regions have long residence times and are less sensitive to global strain rate and nonequilibrium effects. Lakshminarasimhan *et al.* (2007) also observed that the reaction zone closes just downstream of the vortical structures forming a bridge across the centerline. The bridge allows NOx to form in the upstream region of the jet. The difference in scaling behavior for unforced partially-premixed and forced non-premixed

flames can be attributed to two factors. Firstly, in forced flames, broad thermal regions conducive to NOx formation are distributed throughout the flame volume, whereas in unforced flames broad thermal regions are located near the flame tip. Secondly, NOx formed in regions where forcing-induced vortical structures mix hot products and air are less sensitive to strain rate and nonequilibrium effects compared to NOx formed at the flame sheet.

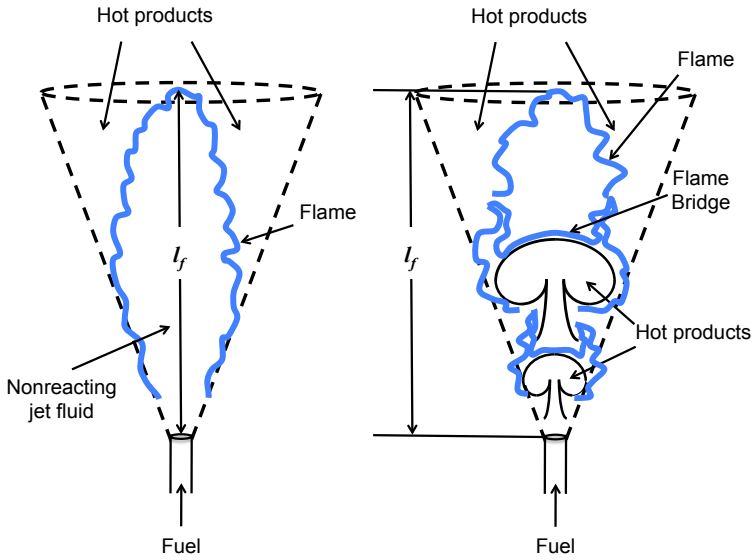

Figure 4.7. Schematic diagram showing the flame structure for unforced partially-premixed jet flame (a) and forced non-premixed jet flame (b). NO forms in hot regions downstream of the flame for both flames. NO formation regions are also located in core regions of ejected vortical structures for forced flames. Approximation of the jet as a cone is indicated by the dotted lines, where the height of the cone is equal to the flame length, l_f.

4.3 SUMMARY

Emissions measurements of NOx, CO and UHC show that forced non-premixed JFICF and unforced partially-premixed JFICF exhibit similar global emissions characteristics. Both forcing and partial premixing are effective methods to reduce NOx, but result in increases in CO and UHC. Forcing a partially-premixed JFICF resulted in even further reductions of NOx. CO and UHC emissions characteristics were compared for forced non-premixed and unforced partially-premixed JFICF by comparing flames with similar NOx emissions. For the CH_4/H_2 flames where soot radiation effects are small, CO trends for forced non-premixed and unforced partially-premixed JFICF are nearly identical and increase linearly as NOx decreases. UHC trends diverge at a critical condition where UHC emissions from forced non-premixed JFICF increase sharply, but UHC from unforced partially-premixed JFICF do not. The sharp increase in UHC occurs when the effective strain rate is sufficiently large and the flame fully lifts.

In order to investigate NOx production mechanisms in forced non-premixed flames, EI_{NOx} for forced non-premixed and unforced partially-premixed flames were scaled according to simple scaling analysis. Emissions indices of NOx for unforced partially-premixed flames did not collapse with simple scaling, whereas EI_{NOx} for forced non-premixed flames did collapse for $\tau_G < \tau_{G,crit}$. For forced non-premixed flames in the $\tau_G < \tau_{G,crit}$ regime, the flame residence time is the dominant NOx mechanism. The success of scaling for forced non-premixed flames is attributed to the flame structure. Well-mixed regions of hot products and air—conditions amenable to NOx formation—are drawn

closer to the centerline of the jet by the ejected vortical structures induced by forcing. Because regions of NOx formation are distributed throughout the flame volume, NOx emissions are more likely to be scaled appropriately by arguments based on flame volume. Furthermore, these NOx formation regions have long lifetimes, and therefore are less sensitive to nonequilibrium effects.

Chapter 5: Flame Stability

The partially-premixed character of forced flames is a result of the periodic formation of vortical structures induced by forcing, which enhances nearfield mixing and in-nozzle partial premixing. Despite the ejection of high momentum vortical structures, forced flames are stable and the flame base is located a few diameters downstream of the jet exit. In forced axisymmetric flames, Lakshminarasimhan *et al.* (2007) observed that the flame closes just downstream of a vortical structure and suggested that the formation of this flame "bridge" plays an important role in forced flame stabilization. Their work, however, did not detail the formation of these "bridges" nor did it consider the interaction between the vortical structure and the flame. Time-correlated imaging is required to characterize the time evolution of the flame base and flowfield in the near region of the jet.

In this study, high-speed imaging techniques are used to investigate the stabilization mechanism of forced non-premixed JFICF. The flame base motion was captured by luminosity images acquired at 10 kHz, and flowfield velocity measurements were acquired at 5 kHz by using high-speed stereoscopic particle image velocimetry.

5.1 Flame Base Response to High-Amplitude Forcing

To track the flame base motion, high speed images of flame luminosity were acquired for forced non-premixed methane JFICF at $Re_{j,mean}$ of 4230 ($r_{j,mean}$=4.6) and 6340 ($r_{j,mean}$=6.9) at a crossflow velocity of 1.7 m/s. Figure 5.1 shows a raw luminosity image

of a $Re_{j,mean}$=4230 JFICF. The $Re_{j,mean}$=4230 and 6240 jet flames were forced at a frequency of 250 Hz and amplitude ratios of 4.8 and 3.3, respectively. Note that at these forcing conditions, the flame is fully lifted. For each experimental condition, 16,384 images were acquired at 10 kHz with a shutter exposure of 100 μs. The images were taken using the same CMOS digital camera (Photron Fastcam Ultima APX) as discussed previously. At 10kHz, the CMOS camera has a resolution of 256 x 512. In physical space, the imaging window is 65 x 130 mm, which results in a spatial resolution of approximately 0.25 mm/pixel. LaVision DaVis imaging software was used to map pixel locations to physical space based on a target grid image. An intensifier and 430 nm bandpass filter were not used, and therefore total visible luminosity was acquired instead of CH* chemiluminescence. High-speed image acquisition with the intensifier could not be achieved because the intensifier gate trigger is limited to a maximum of 1 kHz, since the phosphor decay time is approximately 1 ms. The intensifier can be operated in a continuous mode, where the intensifier shutter remains open; however, this mode of operation resulted in smearing of the luminosity images. For the forcing conditions considered here, the flame near the base is blue in color indicating that the visible luminosity is dominated by CH* emission; therefore, total visible luminosity is a sufficient indicator of the flame base.

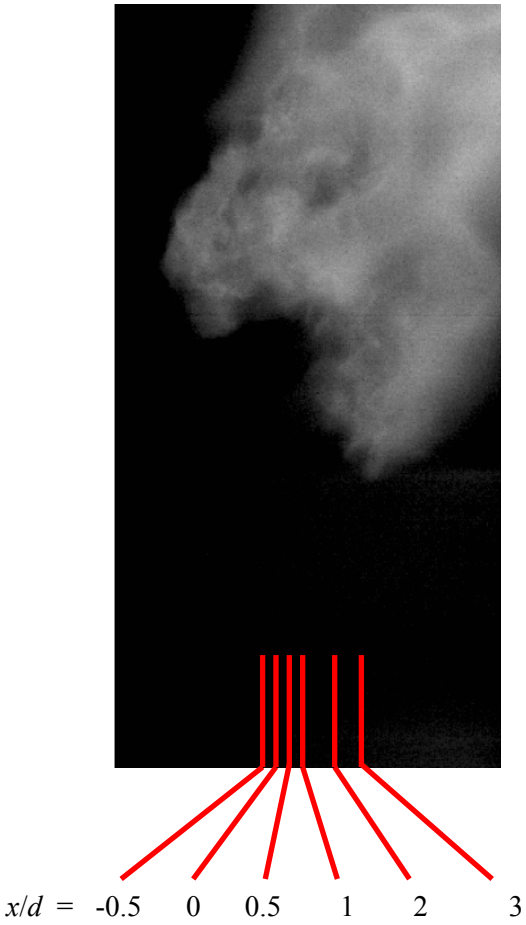

Figure 5.1. Luminosity image of a forced non-premixed methane JFICF at $Re_{j,mean}$=4230 and an amplitude ratio of 3.3. Red lines indicate the *x*/*d* locations where flame base locations are extracted. Crossflow is left to right.

5.1.1 Flame Base Liftoff Location

From the luminosity images, the flame base location was determined at various x (crossflow-streamwise coordinate) locations—x/d=-0.5, 0, 0.5, 1, 2, and 3—as shown in Figure 5.1. The value x/d=0 corresponds to the jet exit centerline, and x/d=-0.5 and 0.5 correspond to the edges of the jet nozzle. In previous definitions of the windward and lee-side liftoff heights, the liftoff heights are determined by the vertical distance from the flame base to the windward or lee-side edge of the nozzle. Similarly, the flame base location is defined as the vertical distance from the jet exit plane to the 20% maximum luminosity contour. A threshold of 20%, compared to 15% in CH* chemiluminescence imaging, was chosen because in several images at x/d>1, background reflections from flame luminosity were larger than 15% of the maximum luminosity signal. Because the reflections were the result of flame luminosity itself, the reflections could not be removed by background subtractions. At x/d=-0.5 where background reflections are not present, the difference between 15% and 20% contours is approximately 0.5 mm. Figure 5.2 shows probability density functions of the flame base location at several x/d locations for the $Re_{j,mean}$=6240 JFICF. Although the flame base of forced non-premixed JFICF is observed to be stable in Figures 3.1 and 3.2, PDFs of the flame base location reveal that, instantaneously, the flame base can be located several diameters away from the most probable flame base location. At x/d=0, the most probable flame base location is approximately eight jet diameters from the jet exit, but instantaneously, the flame base can be located as far as fifteen jet diameters. Also, the shape of the PDF is different at

different x/d locations. The PDFs at x/d of -0.5, 0 and 0.5 are similar; however, at x/d of 1, 2 and 3, the most probable flame base location decreases, the width of the PDF becomes narrower, and the tail on the right-hand side becomes less prominent. The peak of the PDF at x/d=-0.5 is near y/d of 8.5, whereas the peak of the PDF at x/d=3 is near y/d of 6.5. Table 5.1 shows mean y/d locations of the flame base at x/d. The lower flame base location on the lee side of the flame is consistent with the asymmetric flame lifting characteristics discussed in Chapter 3. At x/d=-0.5, the full width at half maximum (FWHM) is approximately three jet diameters and the tail on the right-hand side extends past y/d=15, whereas at x/d=3, FWHM is about two jet diameters and the tail does not extend past y/d=10. The difference in the shape between the windward and lee-side PDFs indicates that the flame base is more variable and dynamic on the windward side of the jet than the lee side. The stability can be attributed to the low momentum wake region behind the jet, which has a stabilizing effect the lee side of the flame. Probability density functions for $Re_{j,mean}$=4230 shown in Figure 5.3 also exhibit similar trends to the PDFs for $Re_{j,mean}$=6240; however, significant changes in the shape of the PDF do not occur until x/d=2.

$Re_{j,mean}$	x/d=-0.5	x/d=0	x/d=0.5	x/d=1	x/d=2	x/d=3
4230	8.93	8.44	7.80	7.31	6.41	6.31
6240	8.82	8.48	8.08	7.59	6.89	6.70

Table 5.1. Mean flame base location, y/d, at several x/d locations for $Re_{j,mean}$=4230 and 6240. Jet exit centerline is at x/d=0.

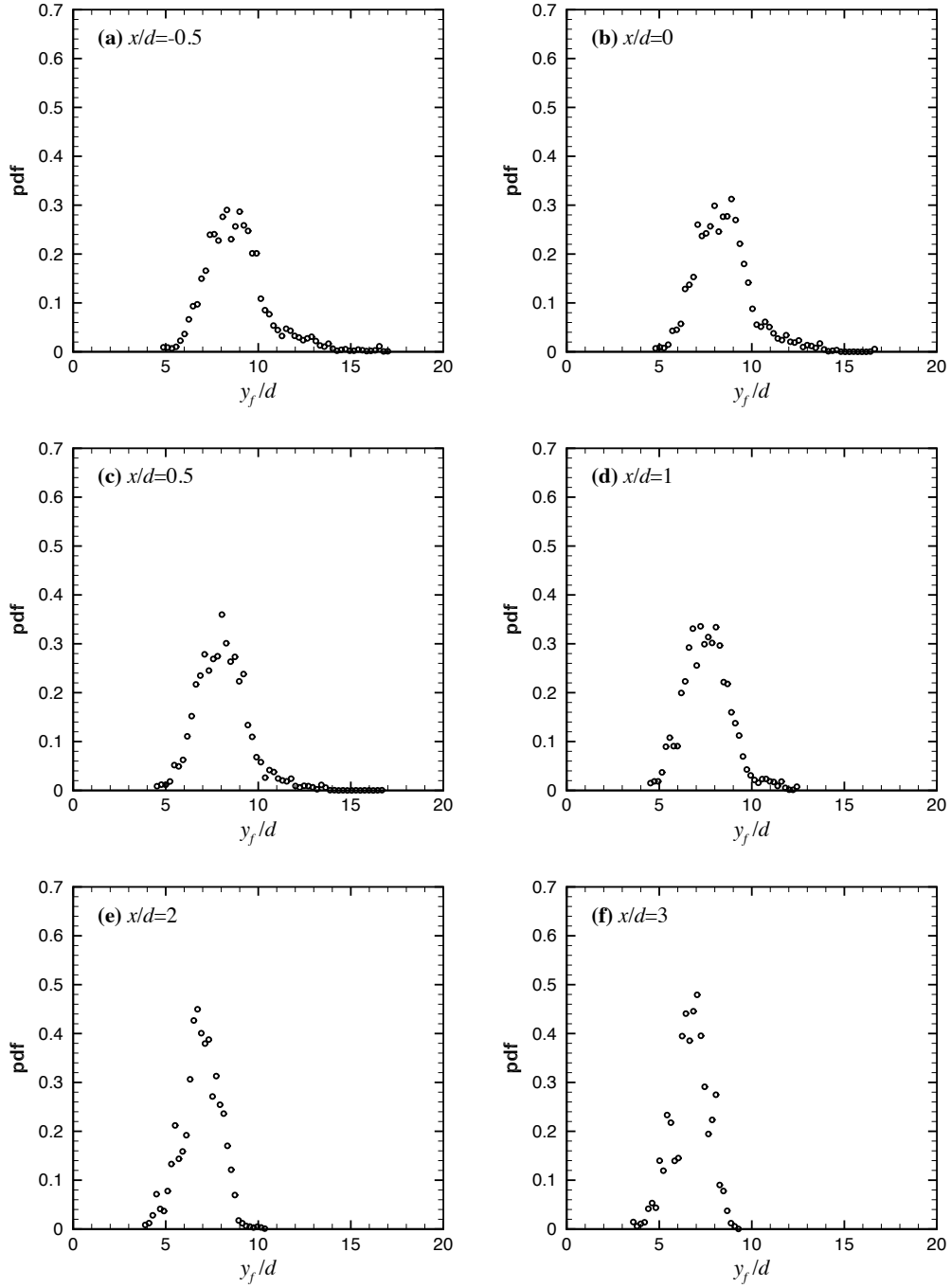

Figure 5.2. Probability density functions of the flame base location, y_f/d, normalized by the jet exit diameter for x/d values of (a) -0.5, (b) 0, (c) 0.5, (d) 1, (e) 2, (f) 3 for a $Re_{j,mean}$=6240 forced non-premixed methane JFICF. Amplitude ratio is 3.3.

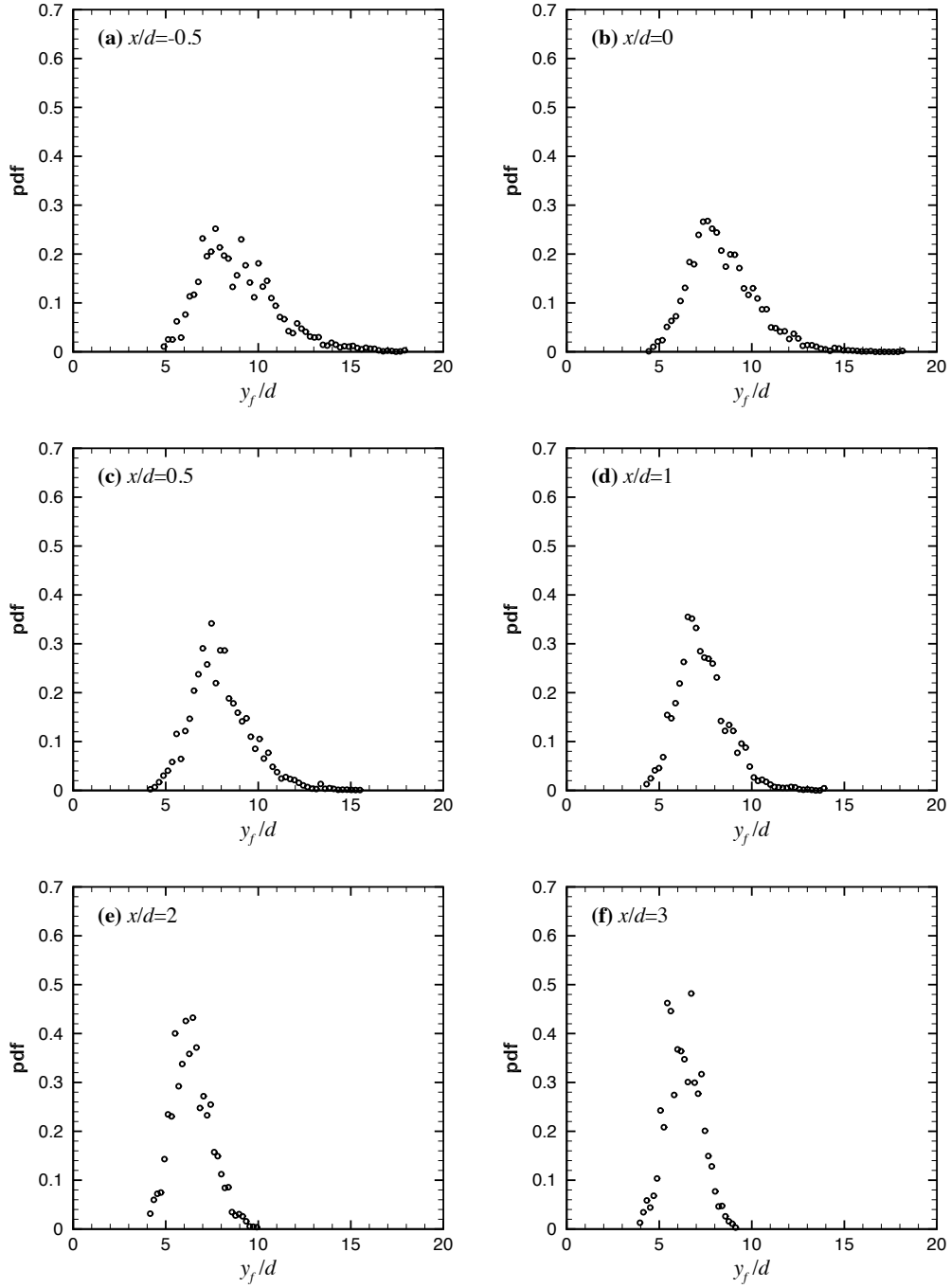

Figure 5.3. Probability density functions of the flame base location, y_f/d, normalized by the jet exit diameter for x/d values of (a) -0.5, (b) 0, (c) 0.5, (d) 1, (e) 2, (f) 3 for a $Re_{j,mean}$=4230 forced non-premixed methane JFICF. Amplitude ratio is 4.8.

5.1.2 Flame Base Frequency Response

To investigate the relationship between the flame base motion and the forcing frequency, power spectral density functions are computed from the time-resolved luminosity movies for flame base locations at x/d=-0.5, 0, 0.5, 1, 2, and 3 for $Re_{j,mean}$=4230 and 6240. The power spectrum of flame base locations for each time series is calculated using Welch's method of modified periodograms. In Welch's method, the power spectral density is estimated by dividing the time series into eight equal segments with 50% overlap, applying a Hamming window to each segment, and averaging the resultant square magnitude of the Discrete Fourier Transform (DFT) of each segment. Figure 5.4 shows the power spectral density (PSD) at the various flame base locations for the $Re_{j,mean}$=6240 JFICF. The PSD plots describe the oscillatory content of the flame motion and show that the flame base is dominated by low frequency motion. At x/d=1, 2, and 3, the PSD plots exhibit a clear peak at 250 Hz forcing frequency, which indicates that the lee-side flame base motion is highly correlated to the forcing frequency; however, at x/d=-0.5, 0 and 0.5, the peak is less prominent and nearly indistinguishable from the PSD noise. The lack of a prominent peak at x/d=-0.5, 0 and 0.5 suggests that the windward-side flame base motion is not as strongly correlated to the forcing frequency as the lee-side motion. Figure 5.5 shows PSD plots of the flame base location for $Re_{j,mean}$=4230. Similar to the larger $Re_{j,mean}$ case, peaks at 250 Hz are observed at x/d locations on the lee side of the flame base. For the $Re_{j,mean}$=4230 JFICF there is no discernable peak at 250 Hz on the windward side of the flame base at x/d=-0.5, 0 and 0.5.

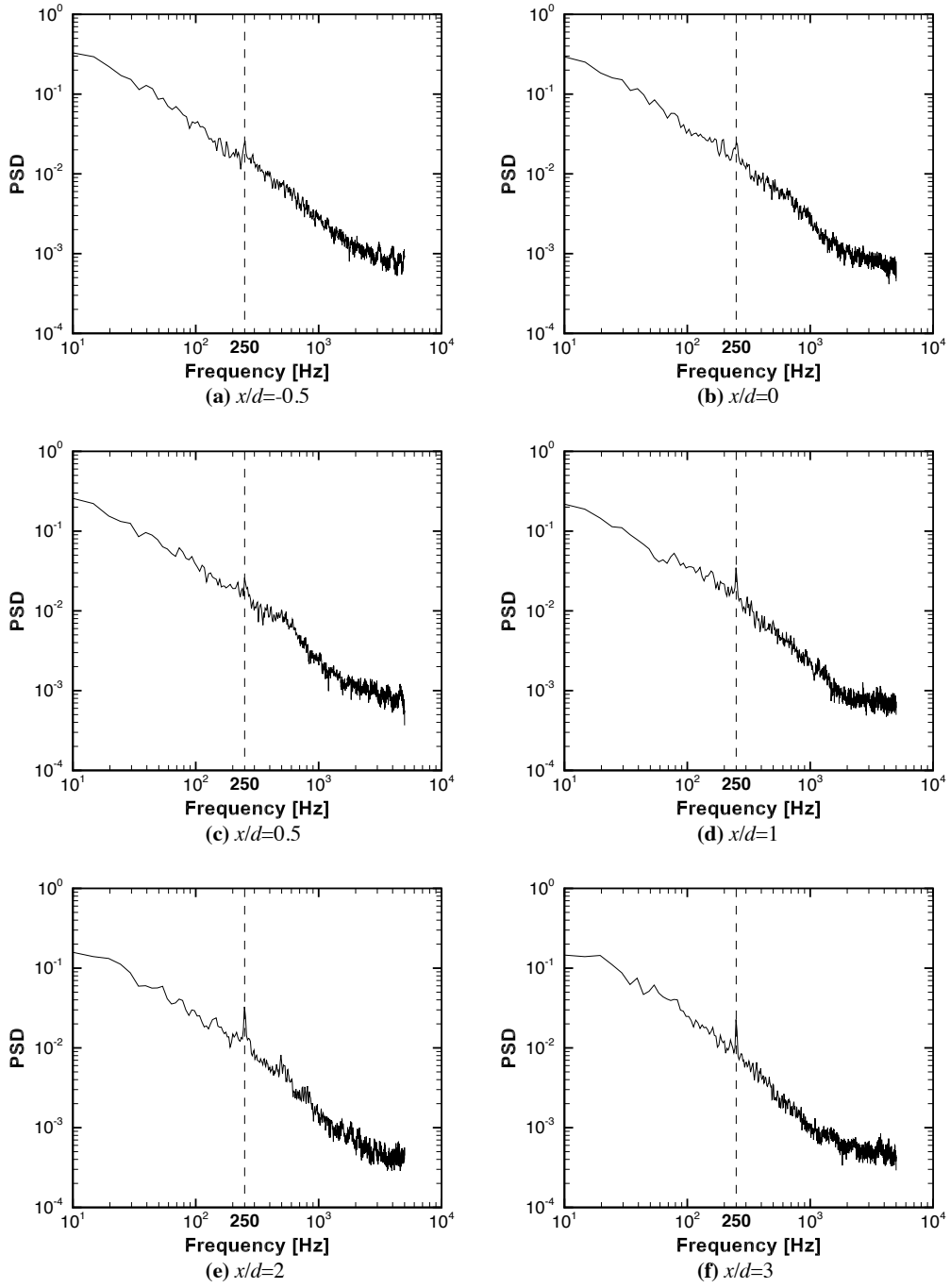

Figure 5.4. Power spectra of the flame base location, y_f/d, at x/d=-0.5 (a), 0 (b), 0.5 (c), 1 (d), 2 (e), 3 (f) for a $Re_{j,mean}$=6240 forced non-premixed methane JFICF. Amplitude ratio is 3.3.

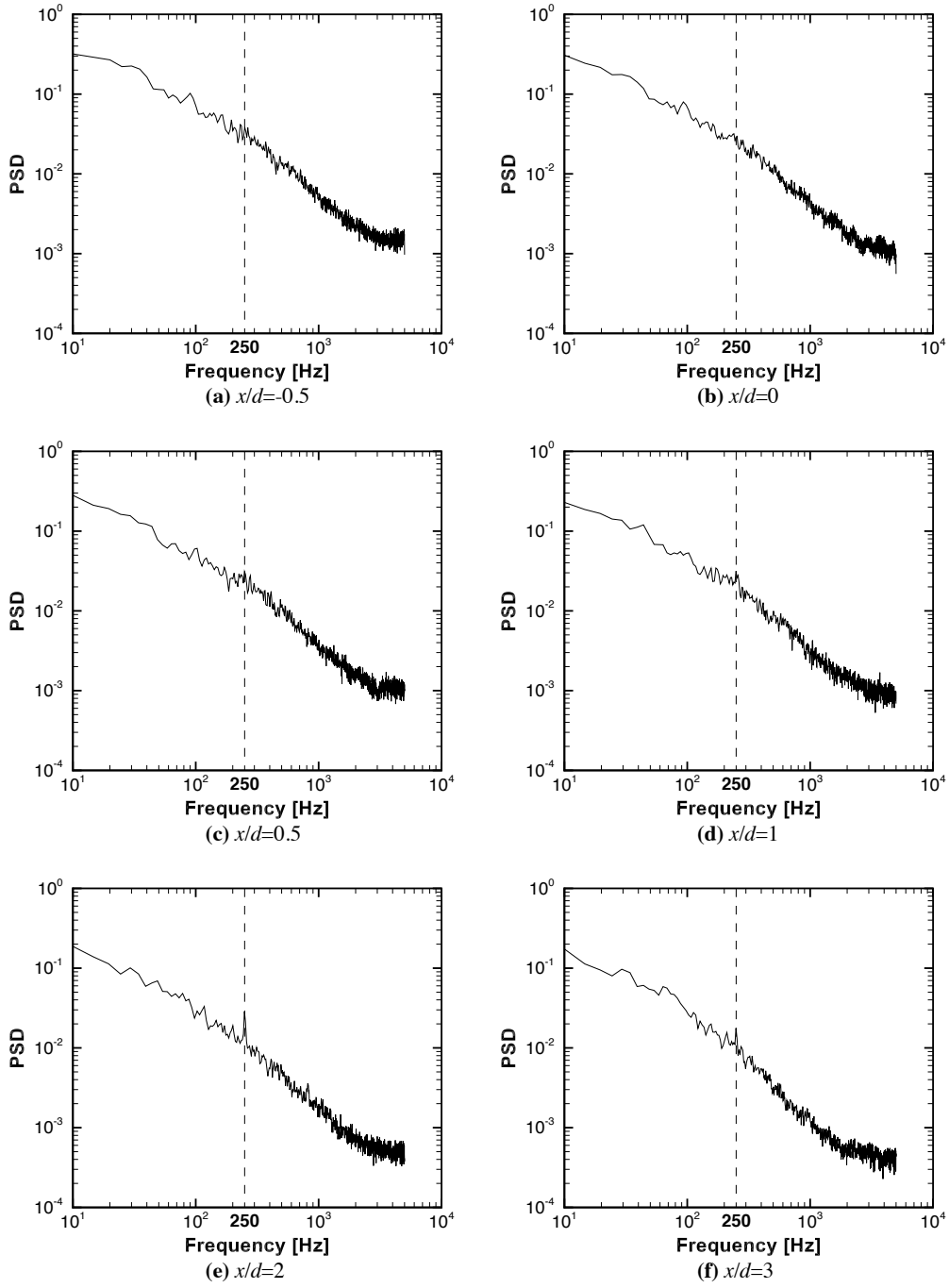

Figure 5.5. Power spectra of the flame base location, y_f/d, at x/d=-0.5 (a), 0 (b), 0.5 (c), 1 (d), 2 (e), 3 (f) for a $Re_{j,mean}$=4230 forced non-premixed methane JFICF. Amplitude ratio is 4.8.

5.2 FLOWFIELD DYNAMICS OF FORCED JET FLAMES IN CROSSFLOW

Time-resolved motion of the flame base extracted from luminosity images of the near region of forced non-premixed JFICF show that the windward and lee-side flame base exhibit different flame stabilization characteristics. To investigate these differences further, high-speed stereoscopic particle image velocimetry was used to obtain time-resolved three-component velocity fields of a non-premixed methane JFICF at $Re_{j,mean}$ of 6340 (U_{cf}=1.7 m/s, $r_{j,mean}$=6.9). Images were taken for the lee-side flame base region of an unforced flame and the windward and lee-side flame base regions of a forced flame. The forced JFICF was forced at a frequency of 250 Hz and amplitude ratio of 3.3. Because the imaging window was limited to 50 x 40 mm (7.9*d* x 6.3*d*), the windward and lee-side flame base regions were imaged separately.

5.2.1 Flame Marking with Seed Particles

To study the stability of the flame base, simultaneous time-resolved imaging of the flowfield and reaction zone is necessary. In jet flame experiments, the reaction zone is often determined from the location of intermediate radical species, namely OH or CH, by either chemiluminescence imaging or laser-induced fluorescence. Chemiluminescence is a line-of-sight integrated technique, and therefore correlations with planar velocity measurements are difficult to interpret. High-speed chemiluminescence and PLIF techniques also require specialized equipment—high-speed intensified camera and, for PLIF, a high-speed tunable dye laser—that was not readily available for this study. An alternative method of marking the reaction zone is to infer the flame location from PIV

images of seed particles. A common method is to seed the flow with ceramic particles, usually alumina, that survive the high temperature reaction zone. The flame is then marked by the abrupt decrease in seed density. Simultaneous imaging with CH PLIF showed that the inferred reaction zone is within 2 mm of the CH layer (Watson *et al.* 1999). The accuracy of the inferred flame location relies on uniform seeding of the flow. In this study, extracting the flame location from PIV seeding images of alumina particles was attempted; however, sufficient seed density was difficult to attain due to the large flow rate and physical size of the crossflow. Instead of seeding the flow with ceramic particles, the crossflow was seeded with fog particles and the jet was seeded with olive oil particles. As shown in Figure 2.7, the flame location is inferred from the disappearance of particles due to evaporation of fog particles and pyrolysis of olive oil particles. This flame marking method has also been used in previous studies (Hasselbrink and Mungal 1998, Muñiz and Mungal 1997), but the accuracy of the inferred flame location has not been quantified.

For ceramic particles and droplets, inferring reaction zones from seed particle images has inherent bias because low density or evaporated particle regions are associated with heated fluid, which does not mark the reaction zone exactly. For ceramic seed particles, the flame is inferred from regions with half the seed density of the 300 K cold flow, which corresponds to the 600 K isotherm (Watson *et al.* 1999). For fog and olive oil particles, seed particles are consumed at temperatures lower than the flame temperature, and so there is an expected difference in the locations inferred from a reaction zone marker and an evaporation technique. For axisymmetric lifted jet flames,

this bias between the preheat zone and the reaction zone is assumed to be small at the flame base (Muñiz and Mungal 1997). A more significant problem is that the interpretation of the reaction zone from seed particle images is complicated by regions of high temperature fluid or extinction, which are indistinguishable from the preheat region of the flame. Proper interpretation of the seed particle contour is essential in determining inferred flame locations. For forced JFICF, strong recirculation regions are induced by the ejection of vortical structures, and therefore, not all evaporated particle regions are expected to be indications of a flame. To assess the validity of inferring flame locations and, more importantly, the flame base from the disappearance of seed particles, OH PLIF and planar laser scattering images of the forced non-premixed JFICF were acquired simultaneously at four equally-spaced time intervals within the forcing cycle. A total of 400 images were acquired of a forced non-premixed 70% methane/ 30% hydrogen JFICF at a $Re_{j,mean}$ of 4850 (U_{cf}=1.7 m/s) and an amplitude ratio of 3.3. Hydrogen was added to the fuel to ensure that the flame base remained in the imaging field of view.

Figure 5.6 shows several representative images of the OH layer and seed particles. The phase τ is defined as before, where the maximum jet exit velocity is attained at τ=0.25. As expected, the OH structures do not correspond with all regions of consumed particles; however, the majority of the uncorrelated regions are downstream of the flame base. At the flame base location, the seed particle contour corresponds well to the OH layer, but there are instances where consumed seed particles are not accompanied by an OH region (Figure 5.6c,d). These uncorrelated regions are the result of interactions between the flame and an ejected vortical structure, where the flame is pulled toward the

vortex core, stretched and eventually extinguished. Misrepresentation of the flame base due to extinction from vortex flame interactions occurs in less than 5% of the images.

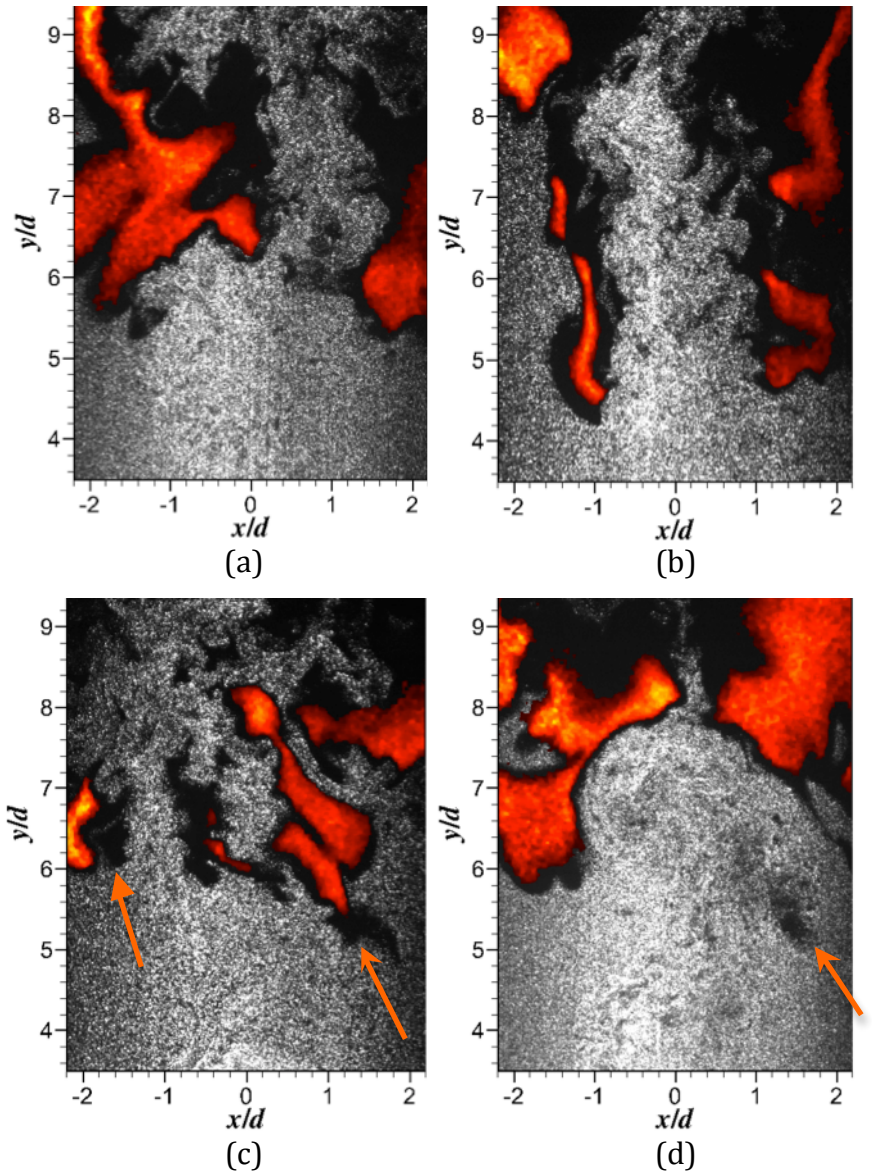

Figure 5.6. Images of flame marking using OH PLIF and seed particle contour taken at (a) τ=0, (b) τ=0.25, (c) τ=0.5, and (d) τ=0.75. Arrows indicate evaporated seed regions at the flame base that are not correlate with OH. Crossflow is left to right.

To quantify the bias error in the flame base location inferred from seed particle images, the windward and lee-side flame base locations were determined from the particle and OH PLIF images. The windward-side flame base is defined by the shortest distance between the jet exit center (x/d=0, y/d=0) and the flame marker for the region x/d<-0.5. The lee-side flame base is defined similarly for the region x/d>0.5. For the OH PLIF images, the flame is marked by the 20% maximum OH signal contour, and for the seed particle images, the flame is marked by the edge of the dark region where particles have disappeared. Because the seed particles are imaged as discrete particles, the seed particle contour cannot be determined from a threshold contour. Instead, the particle image is divided in to overlapped interrogation windows, where the particle density is determined by the total number of peaks in pixel intensity. The flame is determined by the 50% maximum density contour. The edge finding procedure is detailed in Appendix B. Figures 5.7 and 5.8 show histograms of the bias between the flame base determined from particle images and OH PLIF images for both the windward and lee side. The histograms show the total bias, $\Delta D_{PLIF\text{-}PLMS}$, and both components in the x-coordinate, $\Delta x_{PLIF\text{-}PLMS}$, and y-coordinate, $\Delta y_{PLIF\text{-}PLMS}$. The y-axis of the histogram is normalized by the total number of images. The bias error in the x-coordinate is much smaller than the bias error in the y-coordinate because the dominant motion of the flowfield is in the vertical direction. The histograms also show that the bias error is more significant for the lee-side flame base compared to the windward side. On the windward side, higher strain rates result in a smaller preheat zone compared to the lee side. Bias errors associated with high temperature fluid are more prevalent on the lee side of the flame because the wake

promotes recirculation of heated fluid. Table 5.2 shows that the average bias error between the flame bases determined by particle images and the flame base determined by OH PLIF images. On average, the bias error is on the order of 1 mm, which is similar to the bias found by Watson *et al.* (1999) for ceramic particles.

Flame Base	$\Delta D_{PLIF\text{-}PLMS}$ (mm)	$\Delta x_{PLIF\text{-}PLMS}$ (mm)	$\Delta y_{PLIF\text{-}PLMS}$ (mm)
Windward	0.82	0.26	0.74
Lee	1.05	0.25	0.98

Table 5.2. Mean bias error between the windward and lee-side flame base locations determined from OH PLIF and seed particle image.

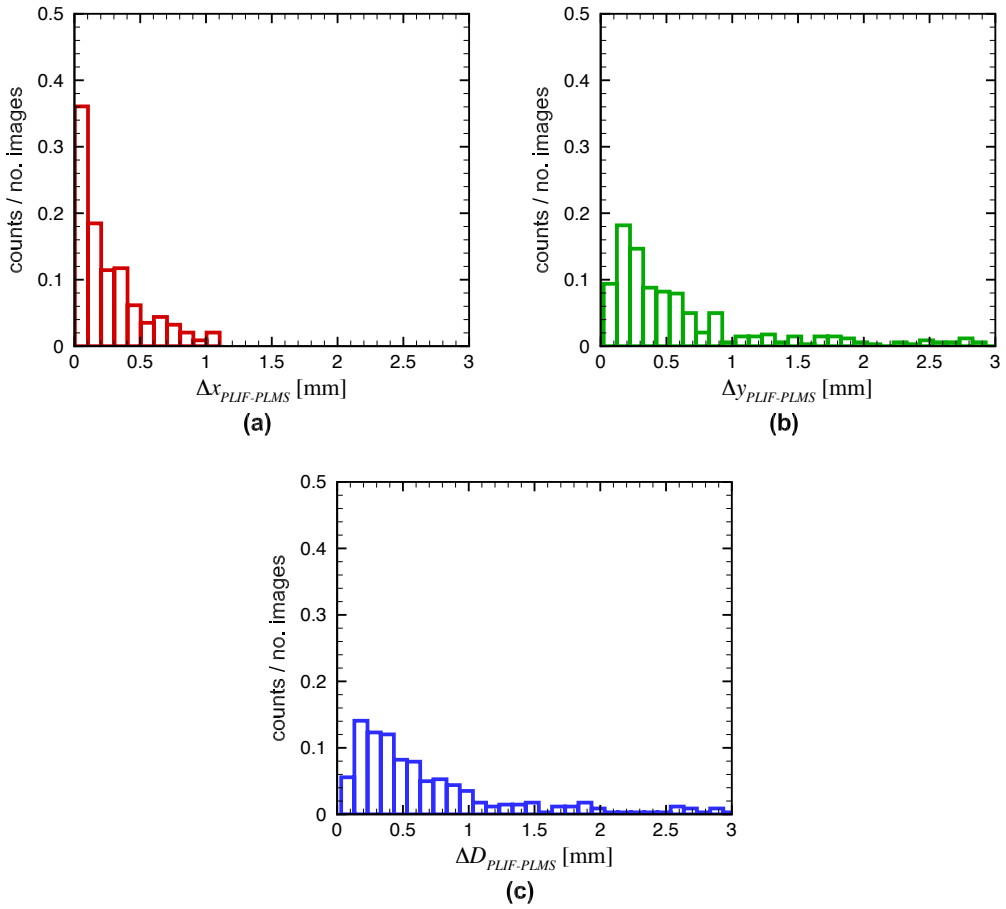

Figure 5.7. Histograms of the bias error of the (a) crossflow-streamwise component, (b) crossflow-normal component, and (c) distance between the windward-side flame base locations determined from OH PLIF and seed particle images.

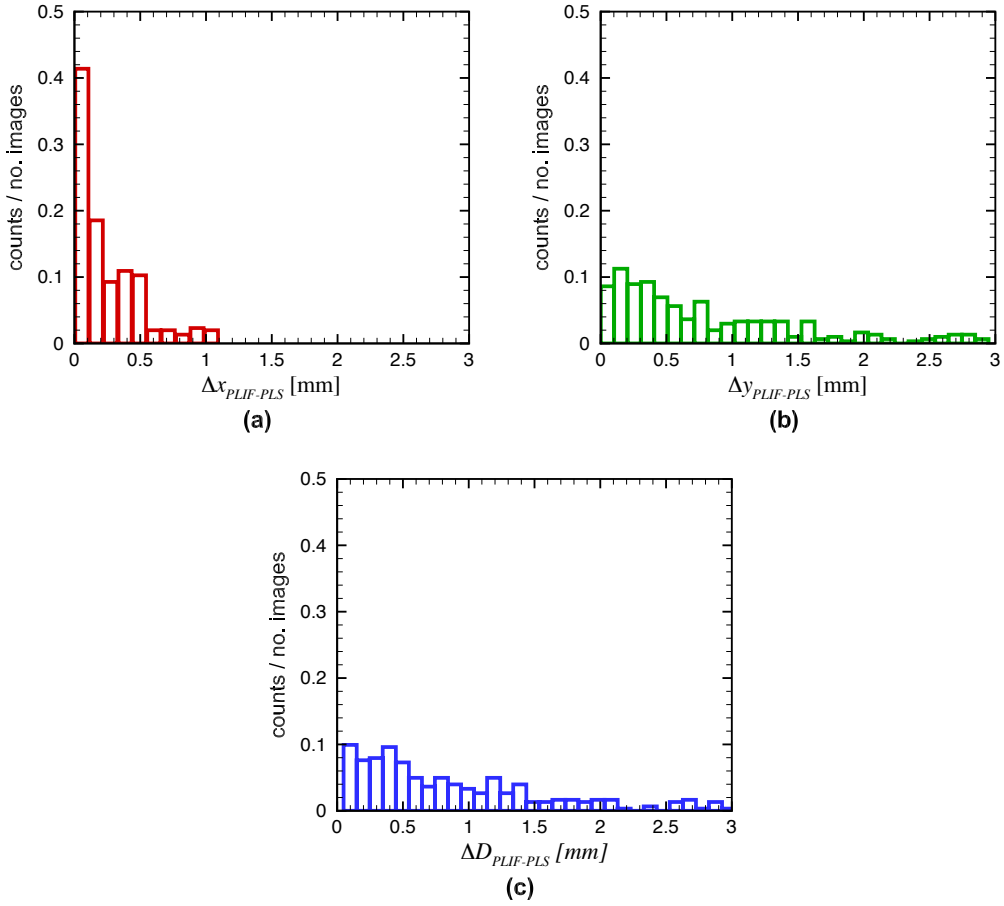

Figure 5.8. Histograms of the bias error of the (a) crossflow-streamwise component, (b) crossflow-normal component, and (c) distance between the lee-side flame base locations determined from OH PLIF and seed particle images.

5.2.2 Velocity Resolution and Uncertainty

Error in velocity measurements from PIV can result from a variety of sources. The accuracy of PIV depends on the measurement of particle displacements, which is determined from the correlation peak. Random errors arise from sources such as out-of-plane particle loss, image noise, image distortion and even the correlation algorithm itself. Bias errors include non-uniformities in seed density or particle illumination, velocity gradients within the interrogation window and *peak-locking*, which occurs when imaging small particles less than 2 pixels in diameter. Several studies have conducted accuracy assessments for the PIV technique. In PIV error analysis, it is common to define the accuracy in terms of pixels. For two-component PIV, Westerweel (2000) determined that for ideal conditions (uniform seeding, no image noise, ideal particle sizes, etc.) PIV errors can be reduced to 0.02 pixels; however a more practical estimate is between 0.05-0.1 pixels (Huang *et al.* 1997). For three-component stereoscopic PIV, an additional source of error arises from the stereoscopic reconstruction of the out-of-plane velocity component. Analysis by Lawson and Wu (1997) showed that error in the out-of-plane component is related to error in the in-plane component by the proportionality constant $tan(\varphi)$, where φ is the angle between the camera viewing direction and the direction normal to the illumination plane. The error is minimized when φ=45°. Another error in the out-of-plane component arises from any misalignment between the target grid and the illumination plane, or registration error. Registration error can be removed by a self-calibration technique, where the misalignment is corrected from camera pair images of

the same particle field (Wieneke 2005). The self-calibration technique, however, does not correct for any image distortion, such as blurring from a reacting flow. Van Doorne and Westerweel (2007) estimated that the error in stereoscopic PIV measurements of a pipe flow ranged from 0.05 pixels at the center of the field of view to 0.18 pixels at the edges where image distortion and velocity gradients within the interrogation window were more prominent.

A common method of assessing the uncertainty in PIV measurements is to apply the PIV technique to known particle displacements from synthetic images computed from a known velocity field. To account for all sources of uncertainty, errors from image distortion and non-uniform seeding would also need to be modeled in the synthetic images. In the current study, determining the uncertainty in such a manner is impractical, and an alternative analysis is used. Recall that the flowfield was simultaneously imaged with two independent stereoscopic PIV systems in order to image a larger field of view. Although the fields of view for each camera pair were different, the cameras were aligned such that the top and bottom fields of view overlapped slightly. An estimate of the uncertainty was obtained by comparing the velocity vectors in the overlap region. Because the grid resolutions of the velocity vectors were slightly different, the bottom velocity field was interpolated on to the grid of the top velocity field. The uncertainty was estimated from the percent difference between the velocity vectors. Figure 5.9 shows a PDF of the percent difference between the velocity vectors measured by the two stereoscopic PIV systems. The average percent difference between the velocity vectors was found to be less than 6%.

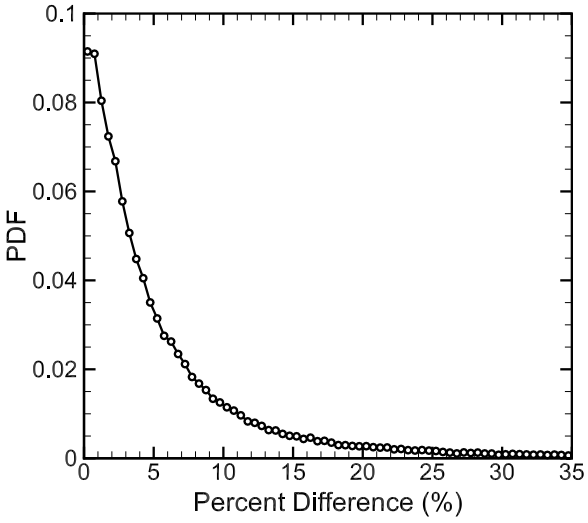

Figure 5.9. One-sided probability density function of the percent difference between velocity vectors in the overlap region of the top and bottom fields of view

In the PIV technique the particle displacement is determined by the pixel displacement of a particle within Δt. A Δt that is too large results in poor correlations and leads to invalid vectors. Because particle displacements are dependent on the local flow velocity, which varies throughout the field of view, the dynamic range may be different at each velocity vector location. For the forced JFICF considered in this study, the range of expected velocities is quite large—peak velocities induced by the forcing can reach upwards of 50 m/s, whereas the velocity in the wake region behind the jet may be on the order of 1 m/s. To measure the peak velocities, Δt must be sufficiently small; however a small Δt is unable to resolve low velocities of interest, namely velocities on the order of the laminar flame speed (0.4 m/s for methane). To resolve low velocities and obtain valid vectors for large velocities, the PIV images were processed with two different Δt values. PIV images are acquired in a frame-straddling manner, shown in Figure 2.9, where the

pulse from laser *A* and the pulses from laser *B* are imaged on adjacent frames, and Δt is set by delaying laser *B*. Because PIV image pairs are acquired at 5 kHz, a longer second time delay exists between laser *B* and laser *A*. The images were processed with both time delays—between laser *A* and laser *B*, Δt_{AB}, and between laser *B* and laser *A*, Δt_{BA}—where Δt_{AB} was used to obtain valid vectors for the large peak velocities and Δt_{BA} was used to resolve low velocities. A single velocity field was extracted from the two velocity fields by conditioning the velocity vectors. For velocity vectors calculated with Δt_{BA}, vectors less than 4 m/s were considered valid vectors; otherwise, the vectors calculated with Δt_{AB} were used. The maximum valid vector obtained using Δt_{BA} was found to be approximately 5 m/s, and therefore, a threshold of 4 m/s was chosen. Table 5.3 summarizes the time delays and estimated velocity resolution for forced and unforced JFICF. The velocity resolution is calculated assuming that the intrinsic accuracy of the stereoscopic PIV technique is approximately 0.2 pixels. For both unforced and forced JFICF, Δt_{AB} was determined by taking PIV images at several time delays. The highest percentage of valid vectors was found for Δt_{AB} that corresponds to a maximum pixel displacement of approximately 10 pixels. For the unforced JFICF, the velocity resolution for Δt_{AB} was sufficiently low, and therefore Δt_{BA} was not considered.

	Δt_{AB} (μs)	Resolution (m/s)	Δt_{BA} (μs)	Resolution (m/s)
Forced JFICF	15	1.04	185	0.08
Unforced JFICF	50	0.31	-	-

Table 5.3. Time delay and velocity resolution for PIV measurements of forced and unforced JFICF.

5.2.3 Time-Resolved Velocity Fields

Because the total combined field of view of the stereoscopic PIV measurements was limited to approximately 50 x 40 mm, the entire flame base could not be viewed simultaneously. For the forced JFICF, the windward and lee-side regions were imaged separately. For the unforced JFICF, only the lee-side flame base was imaged because the motion of the windward-side flame base could not be captured within the field of view. For each region of interest, 1638 vector fields were acquired. Figure 5.10 shows a diagram of the three fields of view. The windward-side flame base of the forced JFICF is shown in red, lee-side flame base of the forced JFICF is shown in green, and the lee-side flame base of the unforced JFICF is shown in blue. Note that both forced and unforced JFICF are fully lifted.

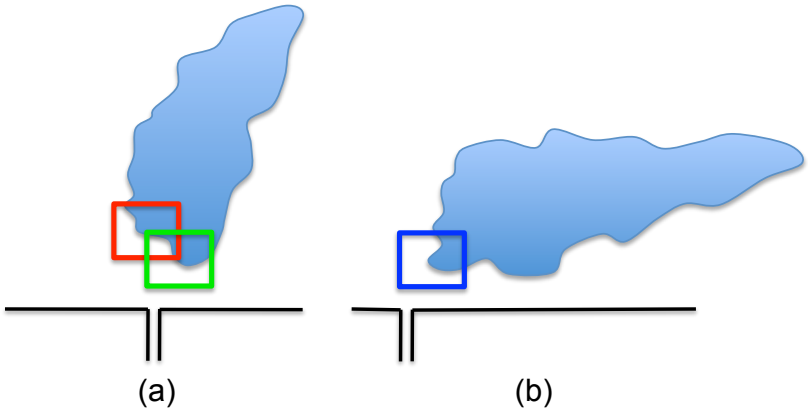

Figure 5.10. Diagrams showing the field of view of velocity field measurements of the forced (a) and unforced (b) JFICF. The field of view of the windward side of the forced flame is shown in red, the lee side of the forced flame in green and the lee side of the unforced flame in blue.

5.2.3.1 Lee-Side Flowfield of an Unforced JFICF

Velocity fields were acquired at 5 kHz to obtain time-correlated images of the flowfield. Figure 5.11 shows a time sequence of the flowfield evolution of the lee side of an unforced methane JFICF. The time between each image is 0.2 ms, which is the smallest time resolution acquired by the PIV system. The contour shown is the vorticity, ω_z, and the dotted black line indicates the location of the flame estimated by the disappearance of seed particles. For ease of discussion, the evaporated seed particle contour will be referred to as the *flame* or *flame base*; however, as discussed in Section 5.2.1, dark regions of evaporated seed particles do not guarantee the presence of a reaction zone. Any ambiguity in the interpretation of the flame will be noted. Figure 5.12 shows a larger plot of the instantaneous flowfield shown in Figure 5.11d. The flow structure in the region below the flame is similar to the structure of a non-reacting JICF, where a series of vorticies develop on the windward side. For the time sequence shown, the flame base is located several jet diameters downstream of the jet exit and does not exhibit a strong response to the vortical motions in the jet shear layer. In general, any instantaneous image of the flowfield of the unforced JFICF looks like Figure 5.12, where the flame base stabilizes in the wake region behind the jet between x/d of 2 and 6. The flame base appears contorted and wrinkled, which is similar to observations made by Hasselbrink and Mungal (2001b) for JFICF imaged using OH PLIF. They observed that the OH layer on the lee side of the flame was highly contorted and relatively broad and concluded that the fluid upstream of the lee-side flame base was partially premixed.

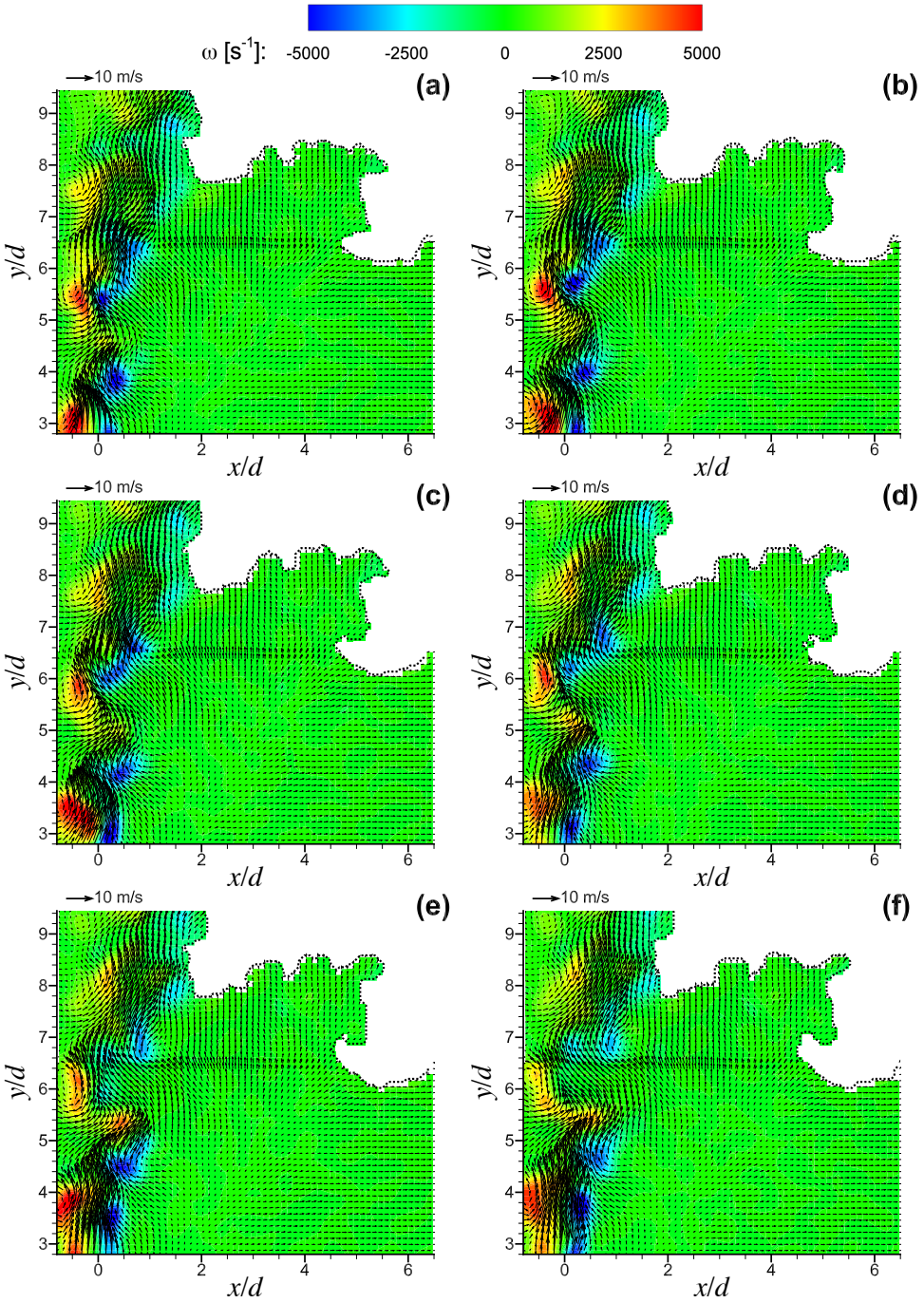

Figure 5.11. Time sequence of the lee-side velocity and vorticity field of an unforced JFICF at $Re_{j,mean}$=6240. Images (a)-(f) are sequential and the time interval between images is 0.2 ms. The flame is marked by the dotted black line. Crossflow is left to right.

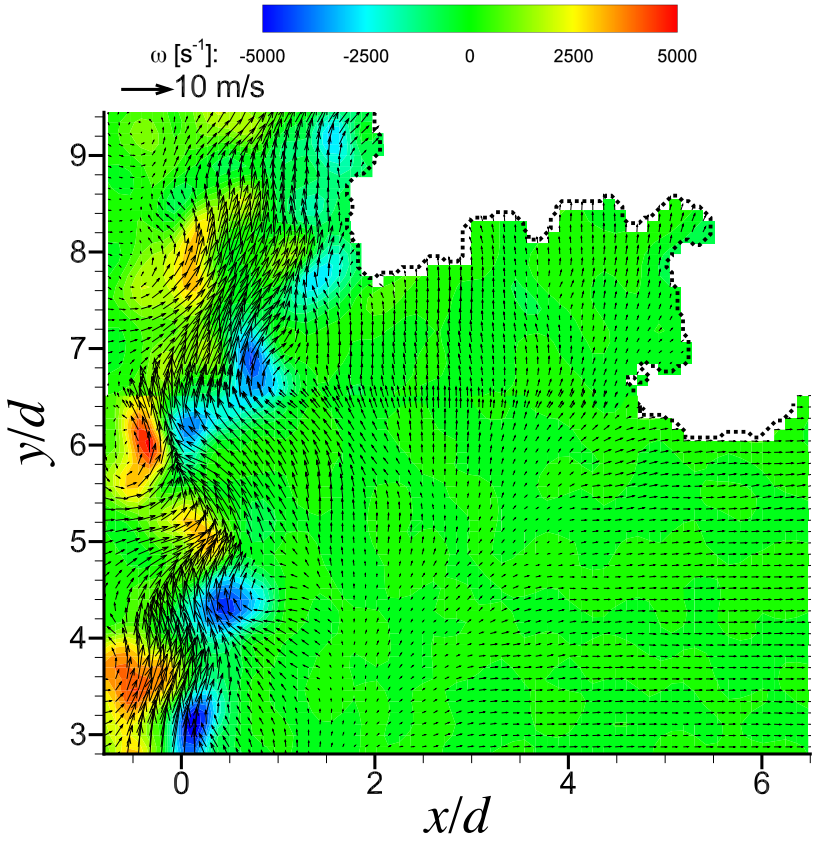

Figure 5.12. Instantaneous plot of the lee-side velocity and vorticity field of an unforced JFICF at $Re_{j,mean}$=6240. The flame is marked by the dotted black line. Crossflow is left to right.

The presence of partially premixed fuel upstream of the flame base serves as a stabilizing mechanism for the lee-side flame base, and potentially, allows for upstream propagation of the flame. Time-resolved measurements of the flowfield show that the flame does indeed propagate upstream. An example sequence is shown in Figure 5.13. For clarity, every third image is shown. In Figure 5.13a the typical flowfield, as discussed above, is observed where the flame stabilizes several diameters downstream of the jet exit. In Figure 5.13b, a pocket of flame region forms below the flame base in Figure

5.13a. Although, the flame looks isolated, the image is a two-dimensional slice of the flowfield, and the flame is most likely the result of out-of-plane flame motion. In Figure 5.13c-f the flame expands and propagates upstream in both *x* and *y* directions. The out-of-plane motion of the isolated flame region is inferred from the out-of-plane fluid velocity component, *w*. Figure 5.14 shows three image pairs of the flowfield immediately before and after the development of the isolated flame. Three examples of isolated flame events are shown in Figure 5.14a-b, c-d, and e-f. In all observed isolated flame events, a region of out-of-plane fluid velocity on the order of the laminar flame speed—0.4 m/s for methane—precedes the appearance of the isolated flame. Although upstream flame propagation is dominated by out-of-plane events, in-plane events are also observed. Figure 5.15 shows upstream propagation of the flame marker in the plane of the flowfield image. Again, for brevity every third image is shown and the propagation region is highlighted in purple. From Figure 5.15a-d the flame marker propagates upstream along the edge of the jet. Because strain rates are large along the jet edge, the flame boundary marked by the seed particles may not be a true indication of the flame due to potential extinction; however, continued upstream propagation is likely the result of flame propagation. In Figure 5.15e,f the flame marker does not continue to propagate upstream and begins to convect downstream with the jet. The abrupt change in the motion is the result of several possible phenomena—the flame is extinguished, the flame has consumed all available oxidizer, or the flame is convected downstream by the jet—however, to determine the exact cause, scalar measurement and a more definitive marker of the reaction zone are needed.

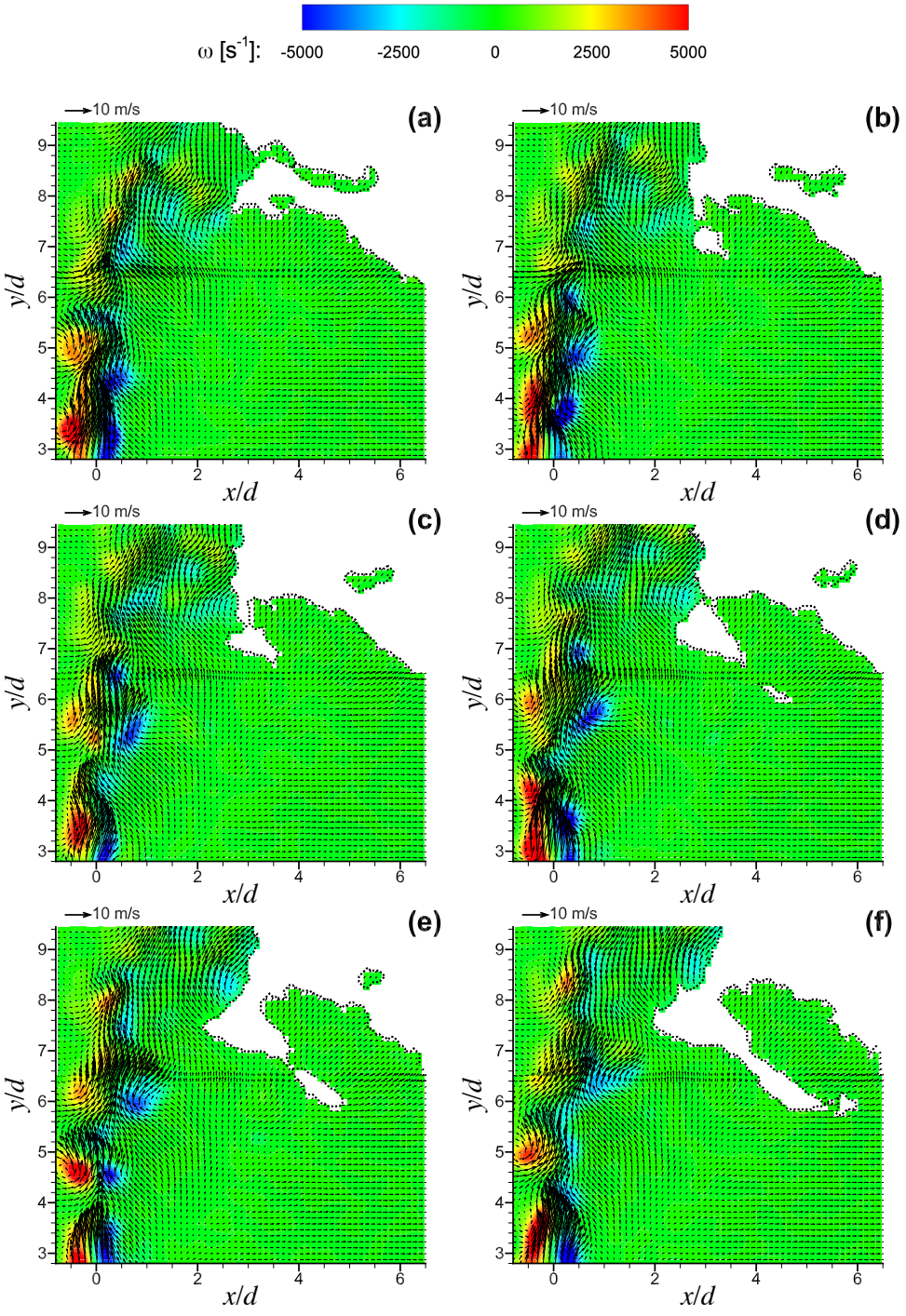

Figure 5.13. Time sequence of out-of-plane flame motion of the lee-side flame base of an unforced JFICF at $Re_{j,mean}$=6240. Every third image is shown. The time interval between (a)-(f) is 0.6 ms. The flame is marked by the dotted black line. Crossflow is left to right.

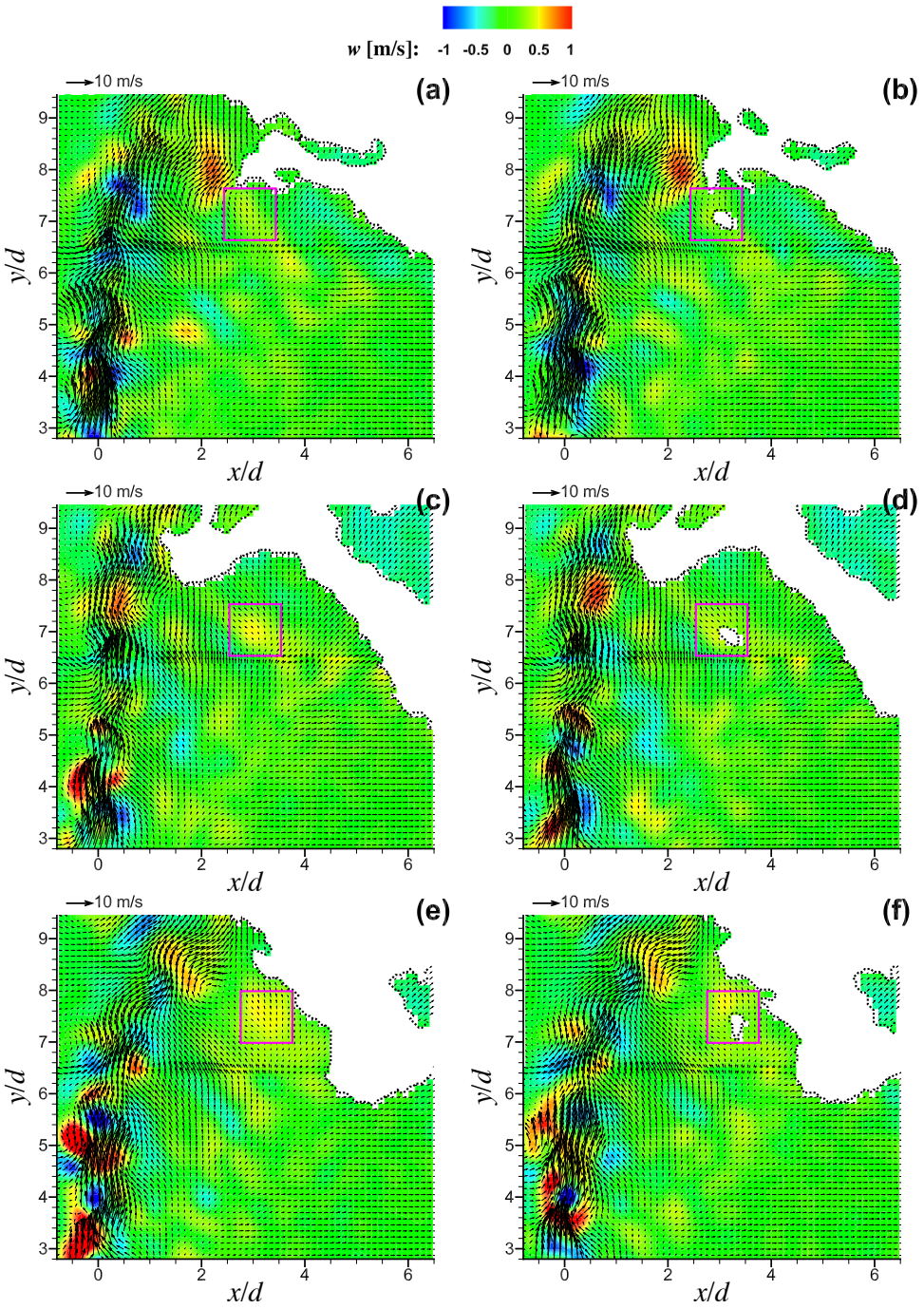

Figure 5.14. Lee-side flame base of an unforced JFICF at $Re_{j,mean}$=6240 before and after the appearance of isolated flame regions. Time interval between each image pair, (a)-(b), (c)-(d), and (e)-(f) is 0.2 ms. The flame is marked by the dotted black line. Crossflow is left to right.

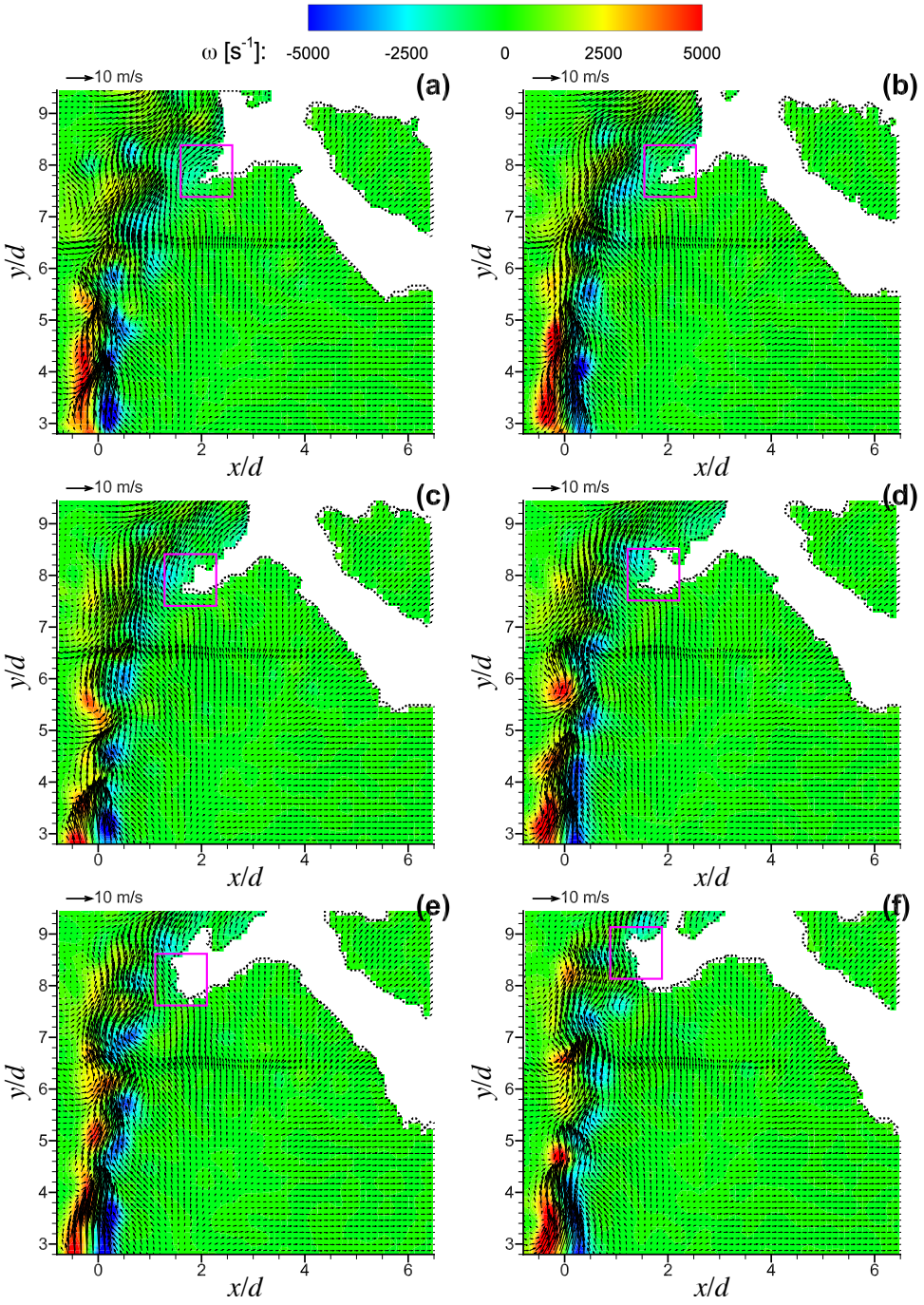

Figure 5.15. Time sequence of in-plane flame motion of the lee-side flame base of an unforced JFICF at $Re_{j,mean}$=6240. Every third image is shown. The time interval between (a)-(f) is 0.6 ms. The flame is marked by the dotted black line. Crossflow is left to right

For partial premixing to occur upstream of the flame base, jet fuel must be present upstream of the flame; therefore, the stabilization mechanism of the flame is directly related to the fluid mechanism that carries and mixes jet fuel in the upstream region. As discussed in Chapter 1, the jet in crossflow is a complex flow geometry that is characterized by several vortical features. Experimental studies of non-reacting JICF have observed that jet fluid can be carried downstream by different mechanisms, namely the counter-rotating vortex pair and the wake structures behind the jet (Fric and Roshko 1994, Smith and Mungal 1998). Wake structures, however, do not necessarily carry jet fluid into the wake for all JICF conditions. Smith and Mungal (1999) suggest that the presence of jet fluid in the wake depends on the development of the wake structures, which is related to the blowing ratio. According to the model by Fric and Roshko, the horseshoe vortex that forms in the boundary layer separates from the lee side of the jet and is pulled upward by the CVP. The sudden upward motion of the horseshoe vortex, referred to as bursting, results in the formation of vortical wake structures. Expanding on this model, Smith and Mungal explain that the fluid associated with the bursting event is accelerated through vortex stretching induced by development of the CVP. For large r, the jet momentum is high and the CVP develops closer (in the x-direction) to the jet; therefore, bursting events occur close to the jet column, which allows jet fluid to be drawn from the lee side of the jet into the wake structure. For small r, the jet momentum is lower and the CVP, and hence bursting events, develops further from the jet column, which results in jet fluid not being drawn into the wake structures. Smith and Mungal observed that the transition between wake behaviors occurs at blowing ratios between 10-

15. Because r=6.9 for the unforced JFICF considered in this study, jet fluid is not expected to be present in the wake structures, and therefore the flame base cannot be stabilized by the wake. Upstream flame propagation, shown in Figure 5.13, is observed to occur frequently in the out-of-plane direction; therefore, the lee-side flame base stability is likely the result of the CVP bringing well-mixed of fuel and air toward the flame base.

5.2.3.2 Windward-Side Flowfield of the Forced JFICF

Forcing significantly changes the flame stability characteristics of the JFICF. Unlike the unforced non-premixed methane JFICF where the flame base stabilizes behind the jet, the forced JFICF stabilizes further forward nearly directly above the jet exit. As discussed in Section 3.1, the liftoff characteristics of the windward and lee-side flame bases are different, which suggests that the stabilization mechanisms are different. Figure 5.16 shows a time sequence of the windward-side flowfield of a single forcing cycle. The acquisition rate is a multiple of the forcing frequency, and thus 20 sequential frames constitute a single forcing period. Furthermore, every twentieth frame is exactly one forcing period apart. For brevity, every other frame is shown. As the vortical structure encounters the flame base, Figure 5.16a-d, the windward side of the vortex pulls the flame base down and toward the centerline of the jet. In Figure 5.16e, a discontinuity in the flame develops due to either local extinction or out-of-plane wrinkling; however, the flame base continues to propagate upstream and toward the jet centerline in Figure 5.16e-j. The flame propagation is fueled by well-mixed fuel and air in the trailing column of the ejected vortical structure. Upstream flame propagation is also observed in the out-of-

plane direction shown in Figure 5.17. Owing to the three-dimensionality of the ejected vortical structure, the out-of-plane and in-plane flame base motions are the result of the same fluid mechanism. As discussed above, flame marking using seed density is not able to clearly identify flame extinction; however, in the time sequence here, the flame continues to propagate upstream after the passage of the vortical structure suggesting that the reaction zone at the flame base has not been extinguished (Figure 5.16e-j, Figure 5.17d-f). Although the strain rate induced by the vortical structure is large, the scalar dissipation near the reaction zone may not be large. In turbulent planar jets, the scalar dissipation structures were found to be correlated to the time history of the strain rate field and not the instantaneous strain rate itself (Kothnur and Clemens, 2005). Because the head of the vortical structure passes by the flame region quickly, large strain rates are not sustained over the entire forcing cycle, and therefore a single vortex-flame interaction does not necessarily extinguish the flame. The vortex-flame interaction thins and stretches the flame region, which increases the surface area of the flame. Kim *et al.* (2009) also observed an increase in flame surface area due to flame stretch in forced non-premixed coaxial hydrogen jet flames. The increase in the flame surface is consistent with results from other studies of flame-vortex interactions (Roberts and Driscoll 1991). Studies have also found thickening of the flammability layer upstream of the vortical structure (Chao *et al*. 2002, Demare and Baillot 2004). Thickening of the reaction zone is difficult to interpret from the flame marker; however images of OH structures in Figure 5.6a,d show broad OH layers at the windward and lee-side flame bases.

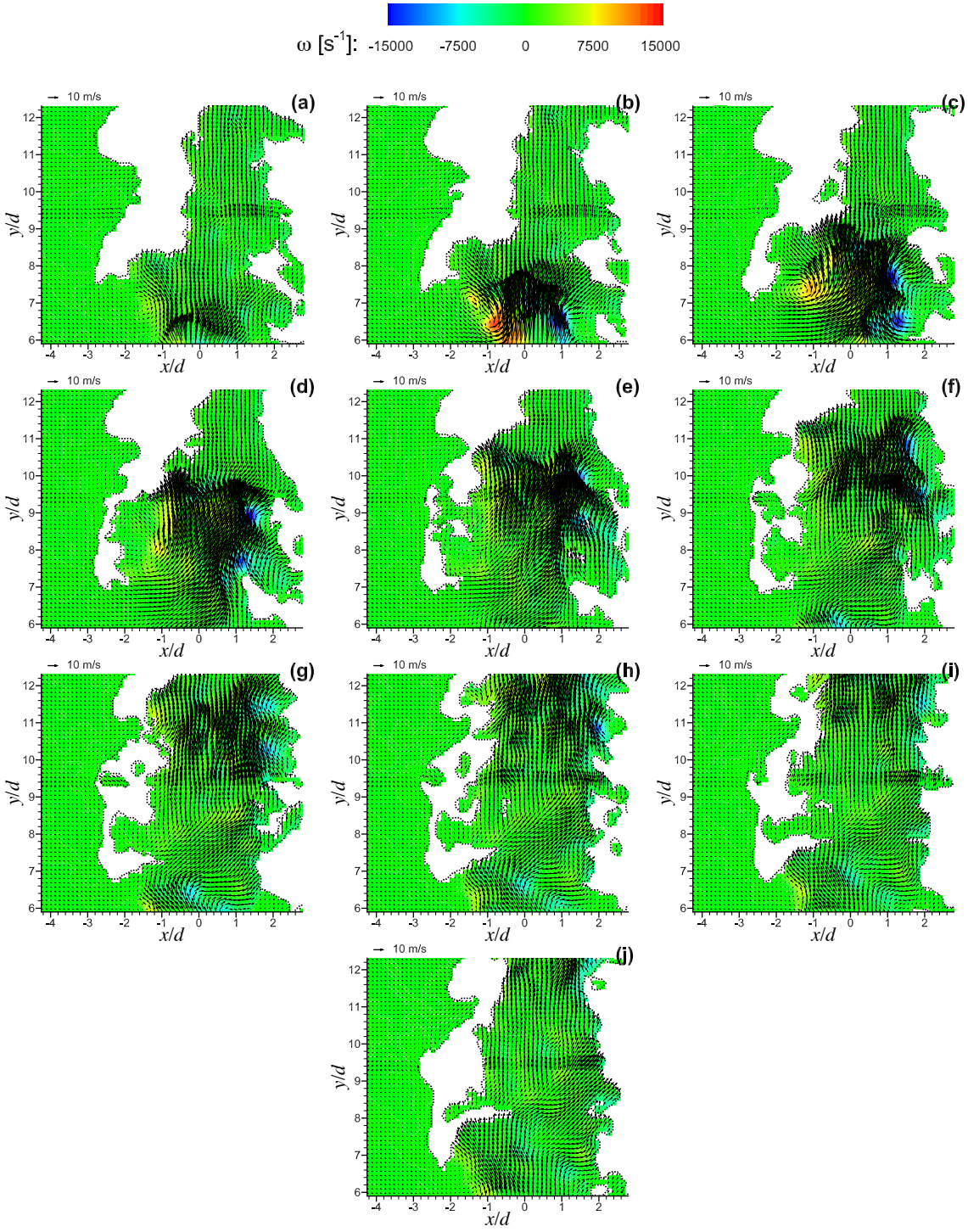

Figure 5.16. Flowfield evolution of the windward side of a forced JFICF at $Re_{j,mean}$=6240 and an amplitude ratio of 3.3 during a forcing period. Every other frame is shown, and the time interval between (a)-(j) is 0.4 ms. The flame is marked by the dotted black line. Crossflow is left to right.

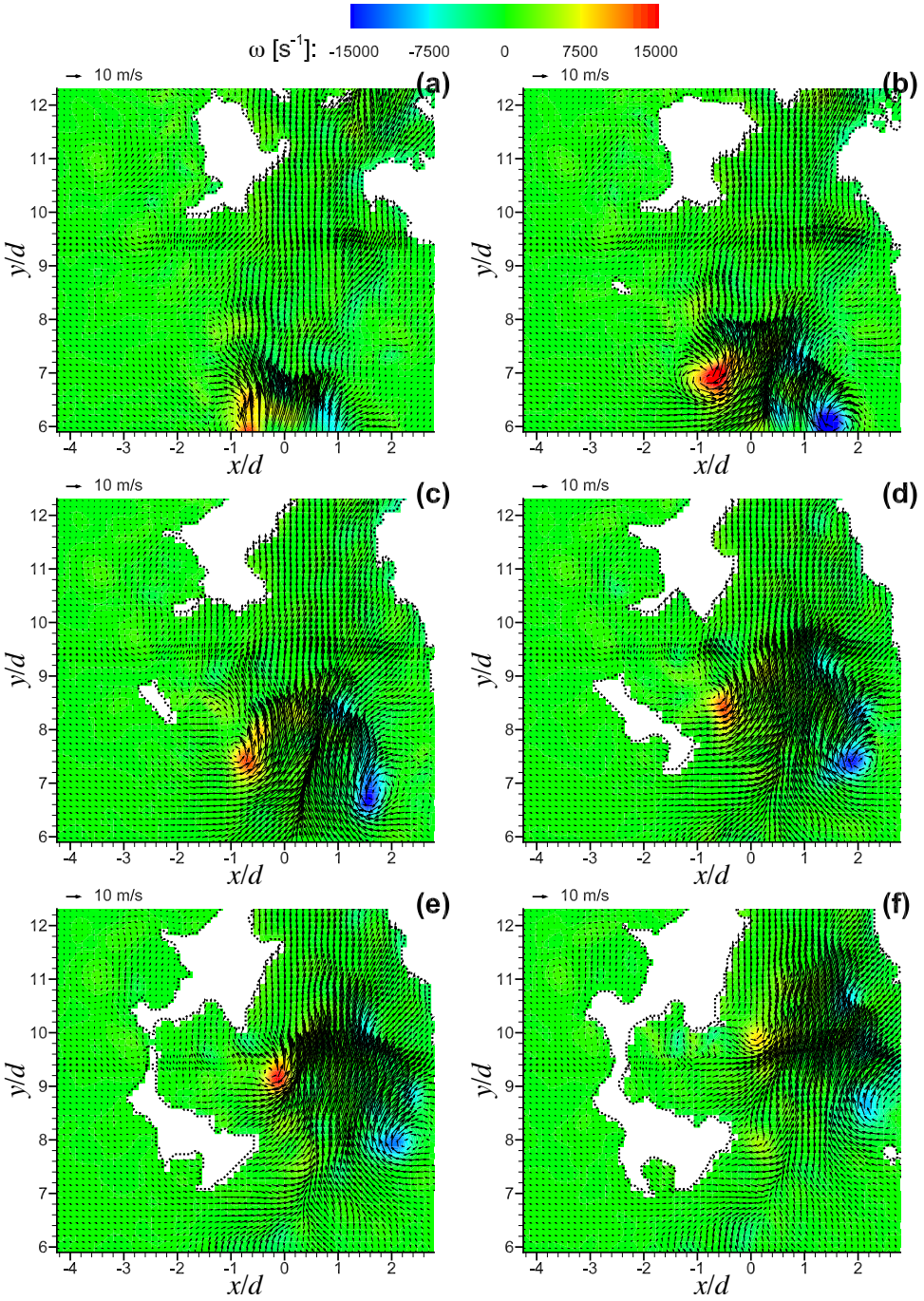

Figure 5.17. Out-of-plane flame base motion of the windward side of a forced JFICF at $Re_{j,mean}$=6240 and an amplitude ratio of 3.3 during a forcing period. Every other frame is shown, and the time interval between (a)-(f) is 0.4 ms. The flame is marked by the dotted black line. Crossflow is left to right.

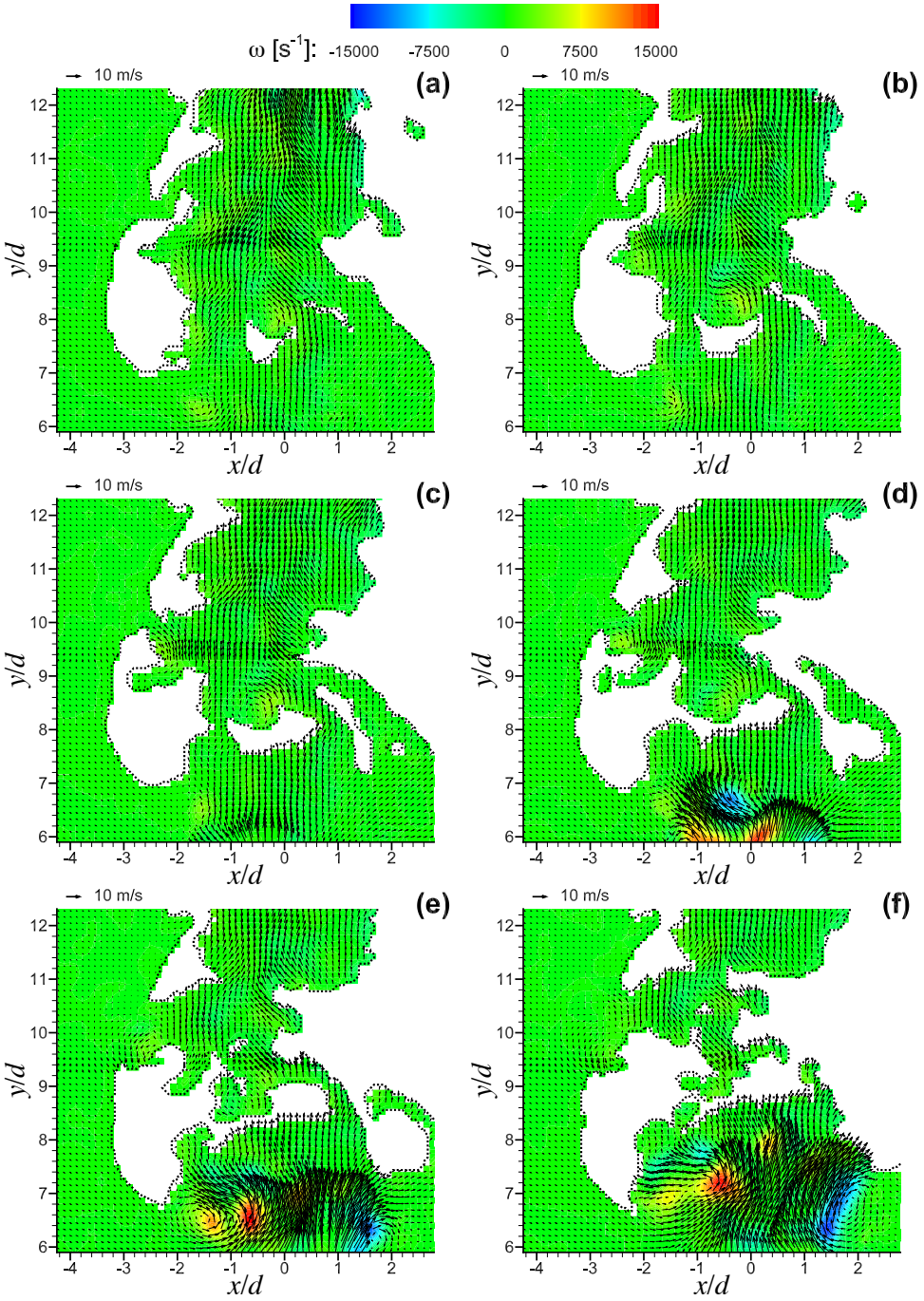

Figure 5.18. Formation of a flame bridge structure in a forced non-premixed JFICF. Every other frame is shown, and the time interval between (a)-(f) is 0.4 ms. The flame is marked by the dotted black line. Crossflow is left to right.

In forced non-premixed axisymmetric jets, Lakshminarasimhan *et al.* (2007) observed the presence of OH layers downstream of the head of the vortical structures. They suggest that this "bridge" between the reaction zones on either side of the jet flame plays a key role in flame stability. The formation of a similar bridge-like event can be inferred from the images of a forced non-premixed JFICF shown in Figure 5.18. These possible bridge-like events are observed during some, but not all forcing cycles. Figure 5.18a shows the flowfield after a vortical structure has passed by the flame base. The flame propagates toward the jet centerline into well-mixed fluid in Figure 5.18b-e, and eventually joins with flame from the lee side of the jet flame in Figure 5.18f. In Figure 5.18d-f, a vortical structure from the subsequent forcing cycle moves into the field of view just upstream of the bridge. The images, however, do not confirm the existence of a flame bridge in forced JFICF—the flame marker does not distinguish between the reaction zone and regions high temperature fluid or extinction—but rather suggest that a potential formation mechanism for flame bridges may be related to the stabilization of the flame base by ejected vortical structures.

The windward-side flame base stabilizes over a wide range of y/d locations. Figure 5.19 shows four flowfields that are acquired at the same phase within the forcing cycle. Even at the same phase, the flame base location varies significantly. The flame base in Figure 5.19a is located near y/d of 7, whereas the flame base in Figure 5.19d is above the field of view of the image. Furthermore, the flame location in the x-direction can also vary significantly from $4d$ upstream of the jet exit centerline (Figure 5.19a) to $2d$ upstream (Figure 5.19b). The intermittent behavior of the windward flame is also

observed in the luminosity images discussed in Section 5.1, where the windward-side flame base does not respond to the 250 Hz forcing frequency.

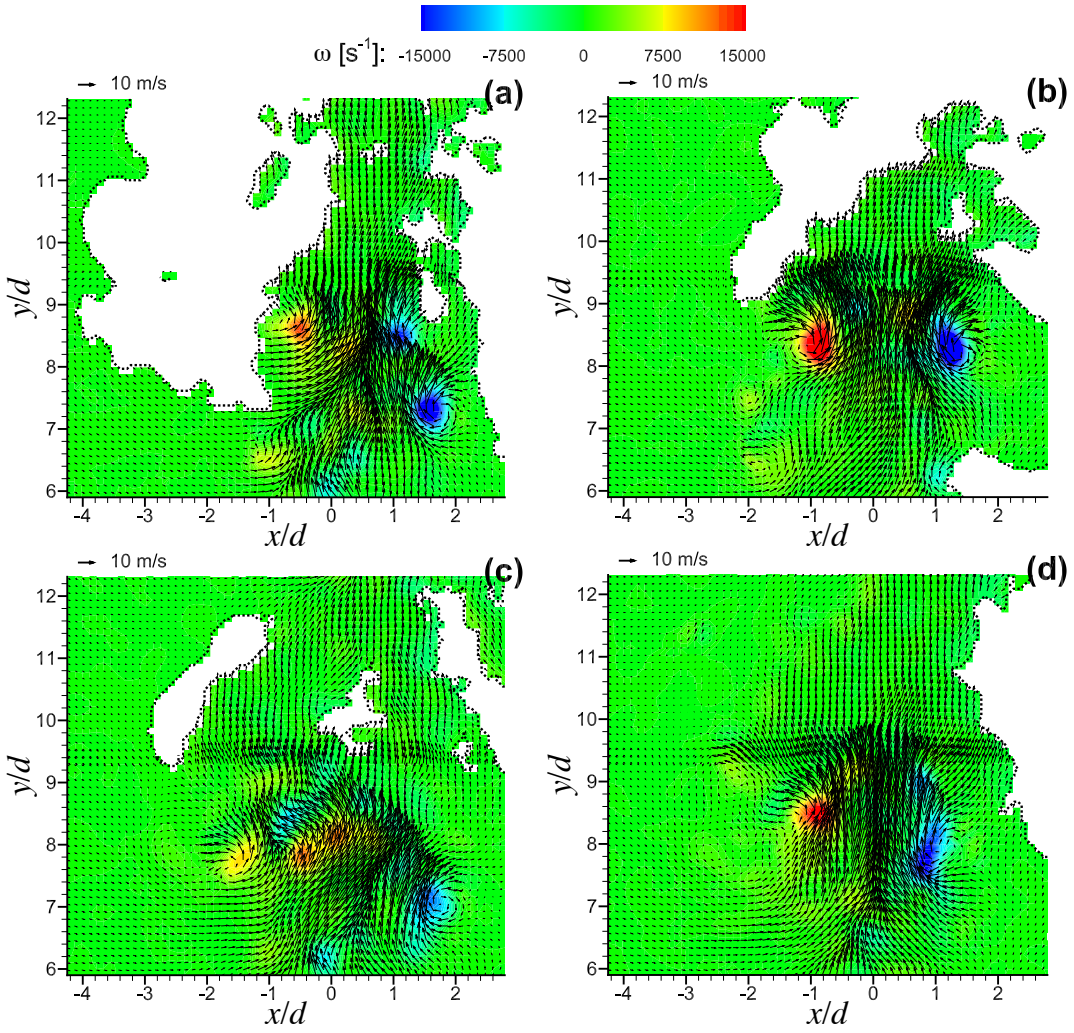

Figure 5.19. Instantaneous flowfields of the windward side of a forced JFICF at $Re_{j,mean}$=6240 and an amplitude ratio of 3.3. Images (a)-(d) are acquired at the same phase within the forcing cycle and are uncorrelated in time. The flame is marked by the dotted black line. Crossflow is left to right.

The intermittent behavior is the result of both stabilizing and destabilizing mechanisms present in the windward region. The stabilizing mechanism—where the flame is pulled down and toward the jet centerline by the vortical structure and then propagates upstream into well-mixed fluid—has been discussed above. A destabilizing mechanism can also occur as the result of flame-vortex interactions. In studies of flame-vortex interactions, if the strength of the circulation of the vortex is sufficiently large, the flame-vortex interaction does not result in the flame thinning but rather extinction (Renard *et al.* 2000). From Figures 5.16 and 5.17, the flame continues to propagate upstream after the passage of the vortical structure, and therefore, the flame is presumed to be not extinguished. Although complete extinction of the flame from a single passing vortex is not observed, discontinuities in the flame frequently develop (Figure 5.16e). Figure 5.20 shows the development of a discontinuity in the flame. In Figure 5.20a-b, the passing vortical structure stretches and thins flame. In Figure 5.20c-d, a weaker secondary vortical structure forms as the head of the primary vortical structure begins to pinch. In forced non-reacting JICF, a secondary vortical structure is also observed to form as the head of the vortical structure pinches from the trailing fluid column (Figure 3.7). Figure 5.20e-f shows the secondary vortical structure punching through the flame resulting in a locally extinguished flame hole. In some instances, the isolated flame base is extinguished by subsequent vortical ejections. Figure 5.21a shows an isolated flame base that has resulted from local extinction from a previous vortical ejection. In Figure 5.21b-c, the ejection of the subsequent vortical structure extinguishes the thinned flame. The flame is presumed to be extinguished because in Figure 5.21d-e the flame marker

shrinks in size and does not propagate. In Figure 5.21f, the flame base is located well downstream in the *y*-direction compared to its previous location in Figure 5.21a. The integrated effect of the primary, secondary and subsequent vortical structures can result in extinction of the flame base. The reason for the absence of a 250 Hz peak in the frequency response spectrum of the windward-side flame base is because this extinction mechanism does not occur regularly.

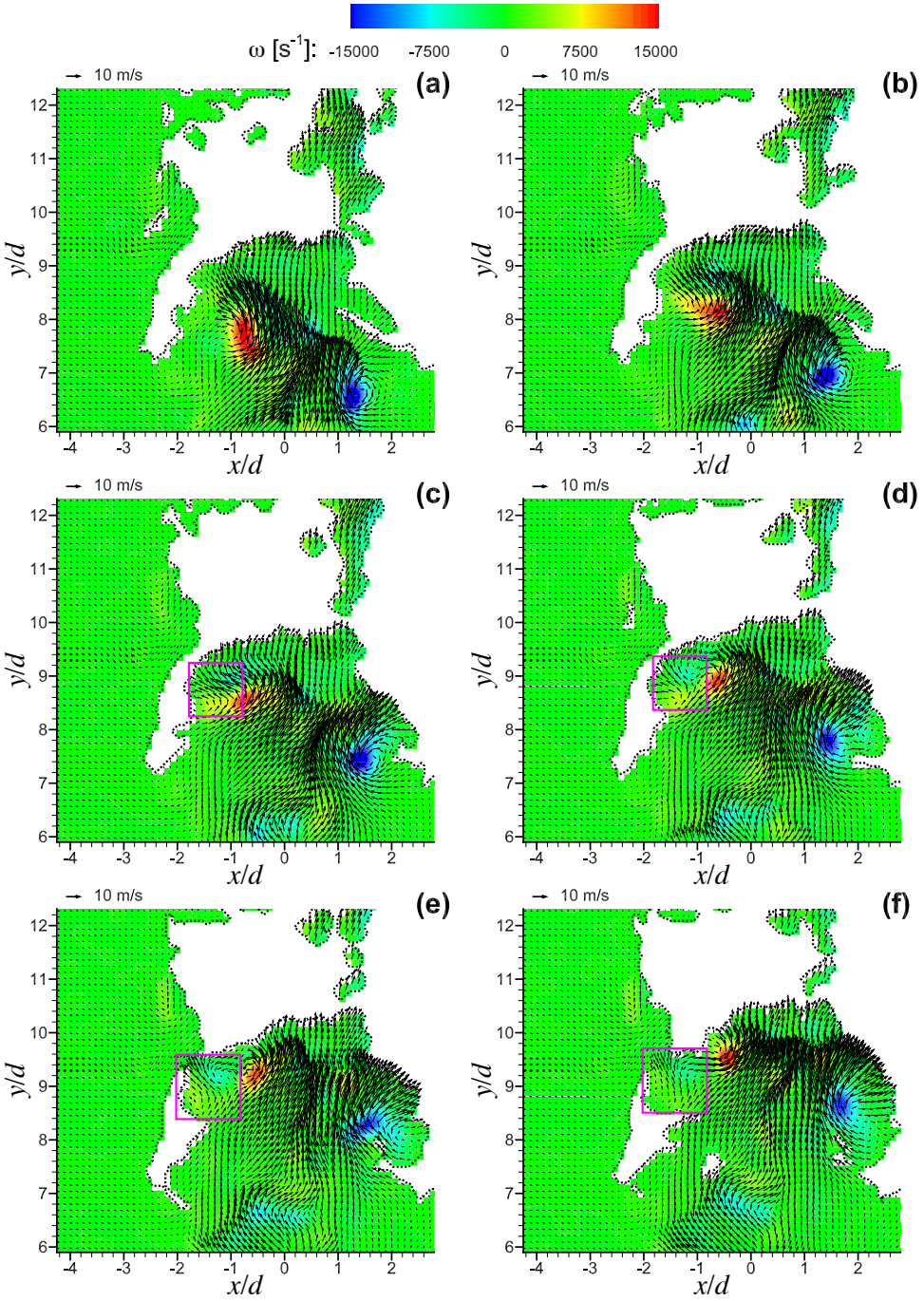

Figure 5.20. Local extinction of the flame region on the windward side of a forced non-premixed JFICF. The time interval between (a)-(f) is 0.2 ms. The flame is marked by the dotted black line. Highlighted square shows a secondary vortical structure. Crossflow is left to right.

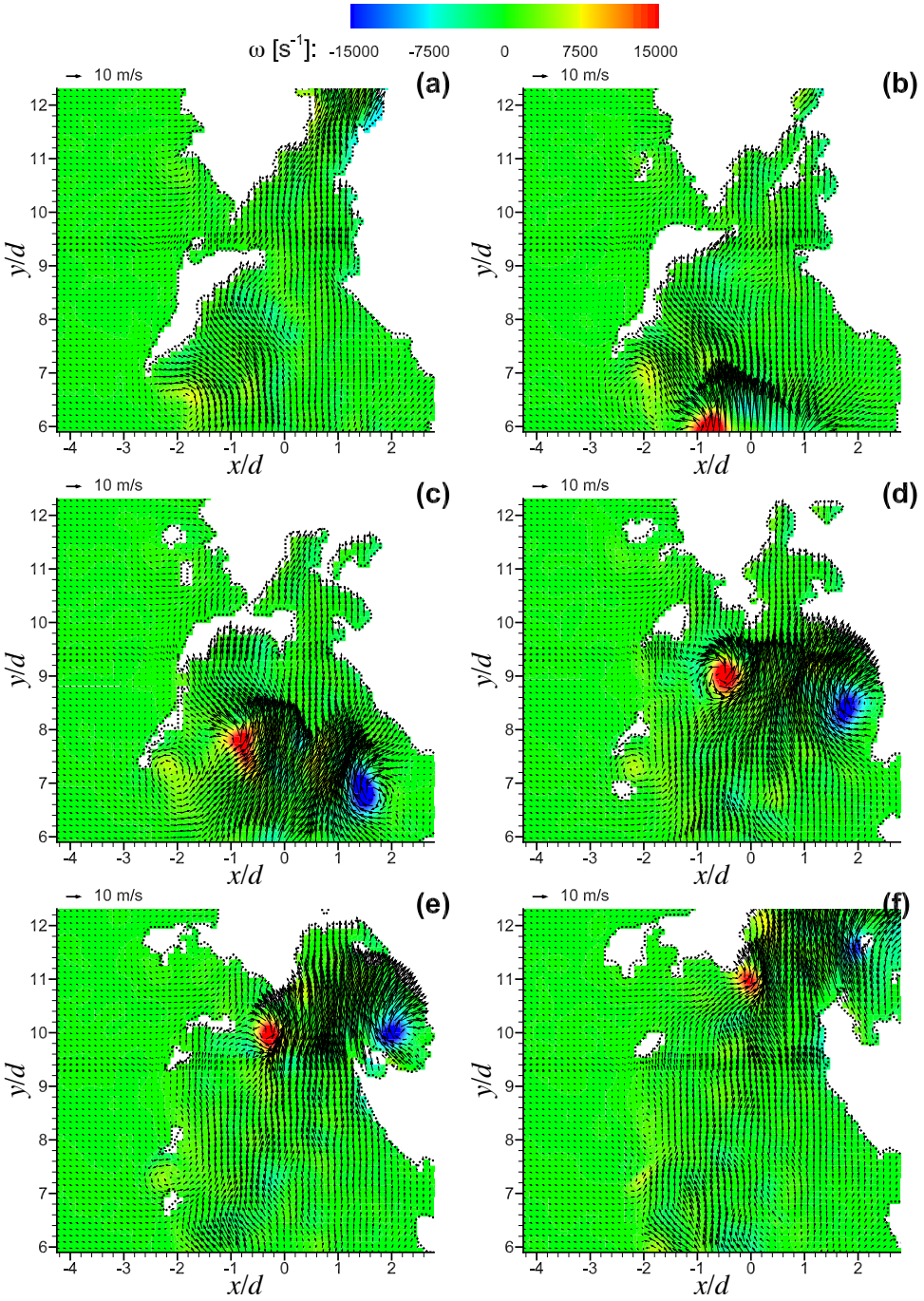

Figure 5.21. Extinction of the flame base region on the windward side of a forced non-premixed JFICF. The time interval between (a)-(f) is 0.6 ms. The flame is marked by the dotted black line. Crossflow is left to right.

5.2.3.3 Lee-Side Flowfield of the Forced JFICF

Unlike the windward-side flame base, the lee-side flame base responds to the forcing frequency as indicated by the peak at 250 Hz in the frequency response spectrum. Figure 5.22 shows the flowfield of the lee side of the forced non-premixed JFICF. For brevity, every third frame is shown. In Figure 5.22a, the flame base is located near x/d=4 and y/d=7. In Figure 5.22b-c, isolated flames appear below the flame in Figure 5.22a indicating that the flame is propagating upstream into partially-premixed fluid. At this point, the vortical structure is still several jet diameters upstream of the flame base, and therefore the upstream propagation is not aided by the passage of a vortex. In this regard, the lee-side flame motion of the forced JFICF is similar to the lee-side flame motion of the unforced JFICF. In Figure 5.22d-f, the vortical structure reaches the flame and pulls the flame upstream toward the centerline of the jet. Here, the lee-side flame motion is similar to the windward side of the forced JFICF; however, unlike the windward side, the lee-side flame base does not exhibit strong intermittency and is more stable. Furthermore, thickening of the flame below the vortical structure is observed in Figure 5.22f. Thickening of the flame marker does not necessarily indicate thickening of the reaction zone; however images of OH layers in Figure 5.6 show that the OH layers at the lee-side flame base are thick. The windward-side flame base is thinned and stretched by both the vortical structure and the incident crossflow, which increases the likelihood of local extinction resulting from secondary and subsequent vortical structures. Flame thickening below the vortical structure would also be inhibited by the presence of the crossflow. The lee-side flame base stabilizes behind the jet and is thinned and stretched only by the

ejected vortical structure. In fact, the crossflow enhances the mixing of fuel and air upstream of the lee-side flame base and brings mixed fluid toward the flame base. The strong response of the lee-side flame base to the forcing frequency is the result of flame base stabilizing closer to the jet exit, which allows for vortical structures to interact with the flame during nearly every forcing cycle.

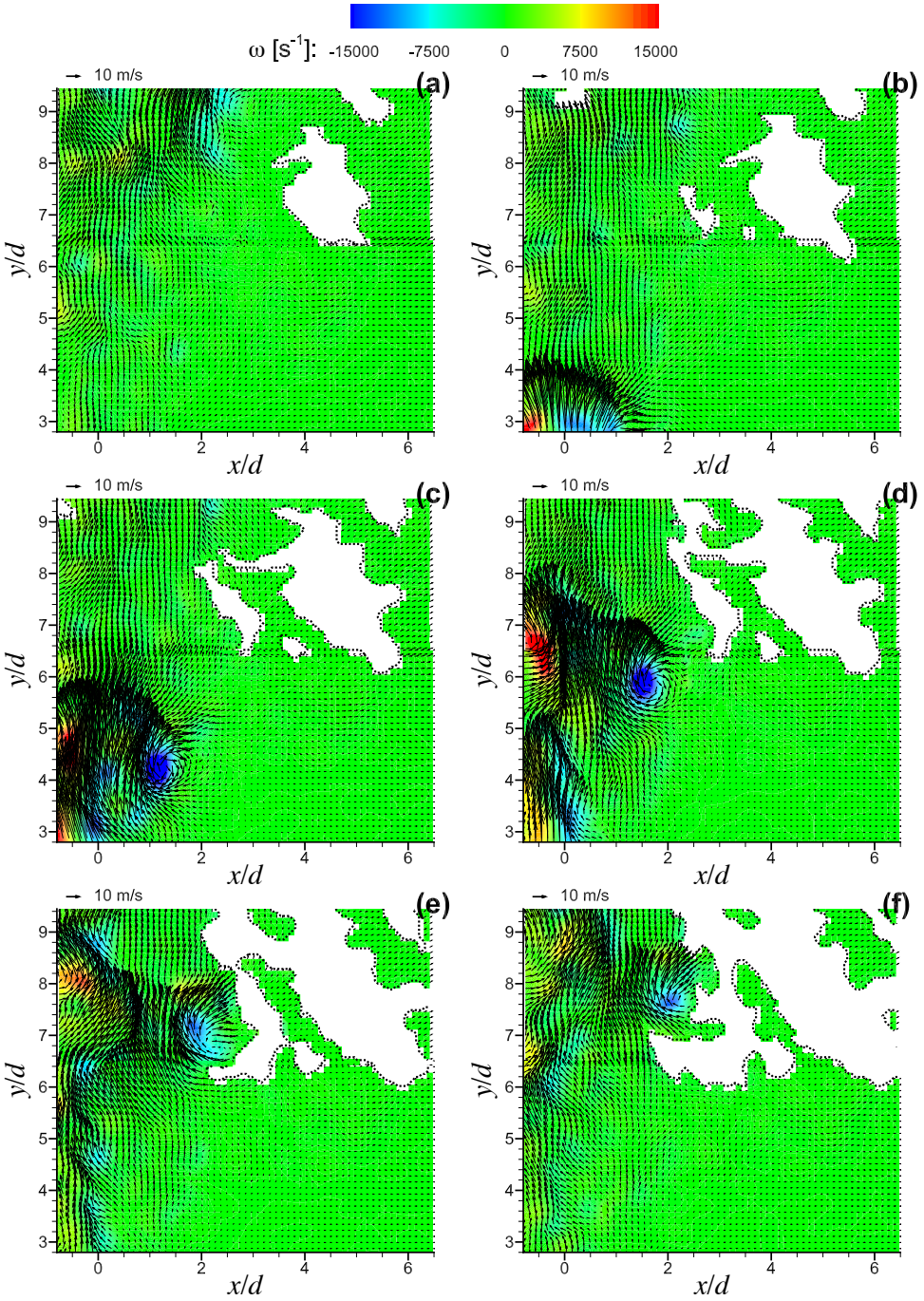

Figure 5.22. Flowfield evolution of the lee side of a forced JFICF at $Re_{j,mean}$=6240 and an amplitude ratio of 3.3 during a forcing period. Every third frame is shown, and the time interval between (a)-(f) is 0.6 ms. The flame is marked by the dotted black line. Crossflow is left to right.

5.2.4 Statistical Description of the Flow at the Flame Base

For lifted flames, the flowfield can be described by conditioning flowfield statistics on the fluid region just upstream of the flame base (Muñiz and Mungal 1997, Hasselbrink and Mungal 1998). In axisymmetric jet flames, the flame base is typically assumed to be the lowest axial position of the flame; however for JFICF, flame motion occurs in both the crossflow-streamwise and crossflow-normal directions, and therefore the flame base defined by the lowest position of the flame may introduce a bias from the true flame base location. The flame base for JFICF may be more appropriately defined as the minimum distance between the flame marker and the jet exit center. For the JFICF considered here, both definitions result in similar flame base locations, and the flame base defined by the minimum distance is used. The gas velocity of the region just upstream of the flame base is determined by the average of the nearest velocity vector immediately below the flame base location and the neighboring vectors immediately to the right, left and below. For brevity, the lee side of the unforced JFICF will be referred to as the *unforced case*, the windward side of the forced JFICF will be referred to as the *windward case* and lee side of the forced JFICF will be referred to as the *lee case*. As previously defined, the x-coordinate is in the crossflow-streamwise direction, the y-coordinate is in the crossflow-normal direction, and thus the z-coordinate is in the out-of-plane direction.

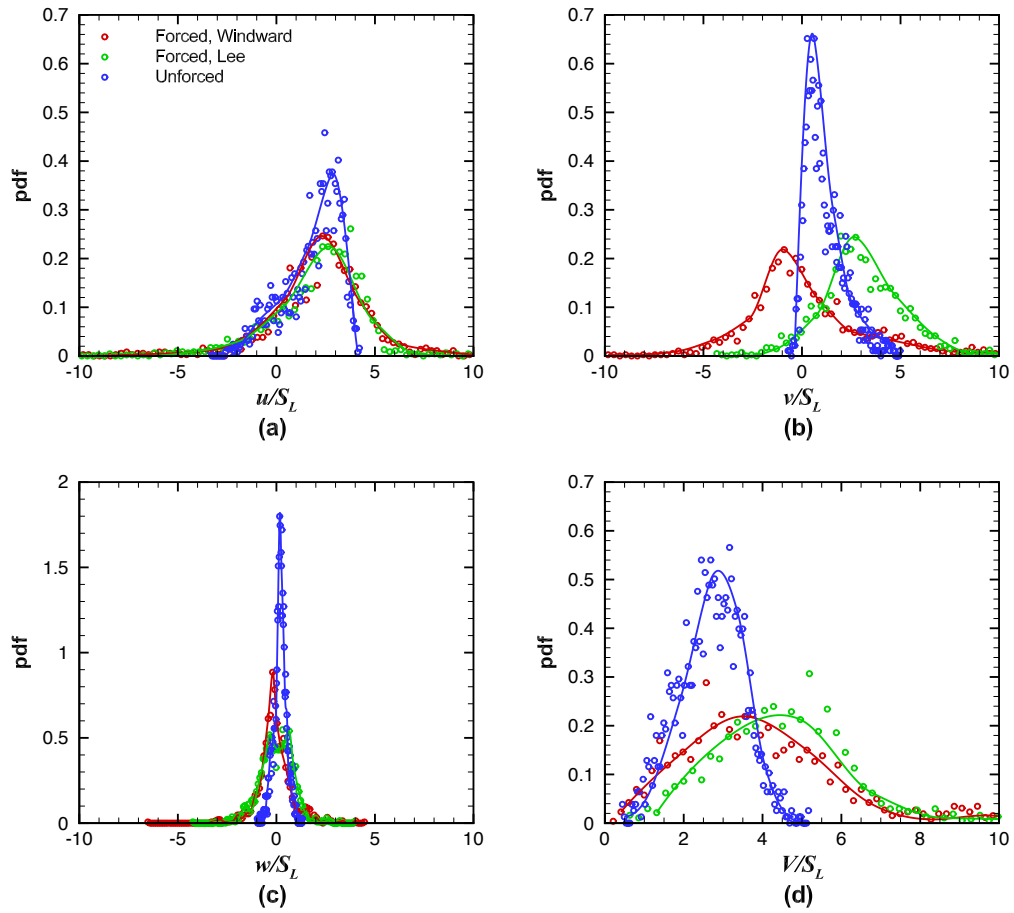

Figure 5.23. Probability density functions of the local gas velocity conditioned at the flame base location. Velocity components, (a) u, (b) v and (c) w, and the velocity magnitude, V, are normalized by the laminar flame speed.

Figure 5.23 shows probability density functions of the local gas velocity conditioned at the flame base for the unforced, windward and lee cases. The three velocity components, u, v, and w, and the speed, V, are normalized by the premixed laminar flame speed, S_L. The PDFs of u/S_L show that the PDF for each case peaks at the crossflow velocity of 1.7 m/s, which indicates that the stabilization in the x-direction is dominated by the crossflow. The effect of the vortical ejections in the windward and lee

case is apparent from the broader tail on the right-hand side, whereas the PDF of unforced case falls sharply between u/S_L of 3 and 4. For the windward and lee cases, the width of the PDFs of v/S_L is broader than the unforced case, which suggests that ejected vortical structures significantly influence the vertical motion of the flame base in the y-direction. For the unforced case, the y-component of the local gas velocity is almost always positive and peaks near the laminar flame speed. In general, v does not exceed the $3S_L$ limit found by Muñiz and Mungal in axisymmetric lifted flames. The PDF of v/S_L of the windward case shows a preference for negative velocities, which suggests that the flame base tends to be pulled down by the local gas velocity. The right-hand side of the tail extends to near $10S_L$, which reflects the occasional upward motion of the windward flame base due to the extinction mechanism discussed in Section 5.2.3.2. The PDF of v/S_L of the lee case shows a preference for positive velocities. The lee-side flame base of the unforced JFICF is more stable than the windward-side flame base, and therefore the tails of PDF for the lee case are not as wide. The PDFs of w/S_L, show that the out-of-plane velocity component is much smaller than the in-plane components. The peak of the unforced PDF of w/S_L is slightly positive and not centered at zero, which is likely the effect of the asymmetry in the counter-rotating vortex pair. The windward and lee PDFs of w/S_L are slightly broader than the unforced PDF and are centered closer to zero. The broadening is due to the ejection of vortical structures, which induces stronger out-of-plane velocity than the CVP in the unforced case. The zero centerline suggests that ejected vortical structures do not exhibit significant asymmetry in the z-direction. The PDF of V/S_L for the unforced case peaks near $3S_L$, but the right side of the PDF exceeds

$3S_L$. Similar results were found by Hasselbrink and Mungal (1998), who suggest that the difference between the axisymmetric case—where the local gas velocity does not exceed $3S_L$—and the crossflow case is due to the three-dimensionality of the JFICF. The out-of-plane component of the local gas velocity measured in the current study shows that w is not significant compared to the in-plane velocity components, and therefore the difference in the local gas velocity is not due to three-dimensionality of the JFICF. The PDFs of V/S_L for the windward and lee cases also exceed the $3S_L$ limit, but are much broader than the unforced case. Although the $3S_L$ limit of the local gas velocity is relatively robust and has been confirmed by other lifted flame studies (Watson *et al.* 1999, Su *et al.* 2006), it is not applicable to forced JFICF.

In addition to the local gas velocity, other flowfield statistics can be conditioned on the flame base location. Figure 5.24 shows probability density functions of velocity fluctuations normalized by the mean gas velocity. Because seed particles disappear in heated regions, velocity can only be calculated in non-reacted fluid. The PDFs of u' and v' are broader for the forced case than the unforced case. The ejection and subsequent breakdown of vortical structures increases the turbulence intensity, in particular the x and y components, at the flame base of the forced JFICF. The PDFs of w' for all three cases are similar indicating that forcing does not effectively increase the out-of-plane turbulence intensity at the flame base. Figure 5.25 shows PDFs of the velocity fluctuations normalized by the premixed laminar flame speed. Both normalization variables result in similar shaped PDFs. In premixed turbulent combustion theory, the turbulent flame speed, S_T, is found to scale with the velocity fluctuation tangent to the local flame front,

u'_o (Law 2006). Although the tangent component of the velocity fluctuation is not shown in Figure 5.25, the flame motion is predominantly in the *y*-direction, and therefore, the tangential velocity fluctuation can be approximated by u'. From Figure 5.25, u'/S_L is generally less than unity, and in the limit of $u'/S_L \ll 1$,

$$\frac{S_T}{S_L} \approx 1 + \frac{1}{2}\left(\frac{u'}{S_L}\right)^2 \tag{5.1}$$

From the measurements of u' at the flame base, S_T/S_L can be estimated using Eq. 5.1. In the *Premixed Flame* and *Turbulent Intensity Theories*, the flame is assumed to stabilize where the local gas velocity equals the turbulent flame speed. Table 5.4 compares the average S_T/S_L calculated from u' to the average v velocity at the flame base for each case. For the unforced and windward cases, v and S_T are comparable, but for the lee case, v and S_T are different. The validity of the *Turbulent Intensity Theory* for the unforced and windward cases, but not the lee case, implies that the theory does not fully describe the flame stabilization mechanism in forced flames.

	S_T/S_L	$u_{G,y}/S_L$
Unforced	1.17	1.16
Windward	2.14	2.42
Lee	1.72	3.43

Table 5.4. Comparison of the average turbulent flame speed and local gas velocity at the flame base of unforced and forced non-premixed JFICF.

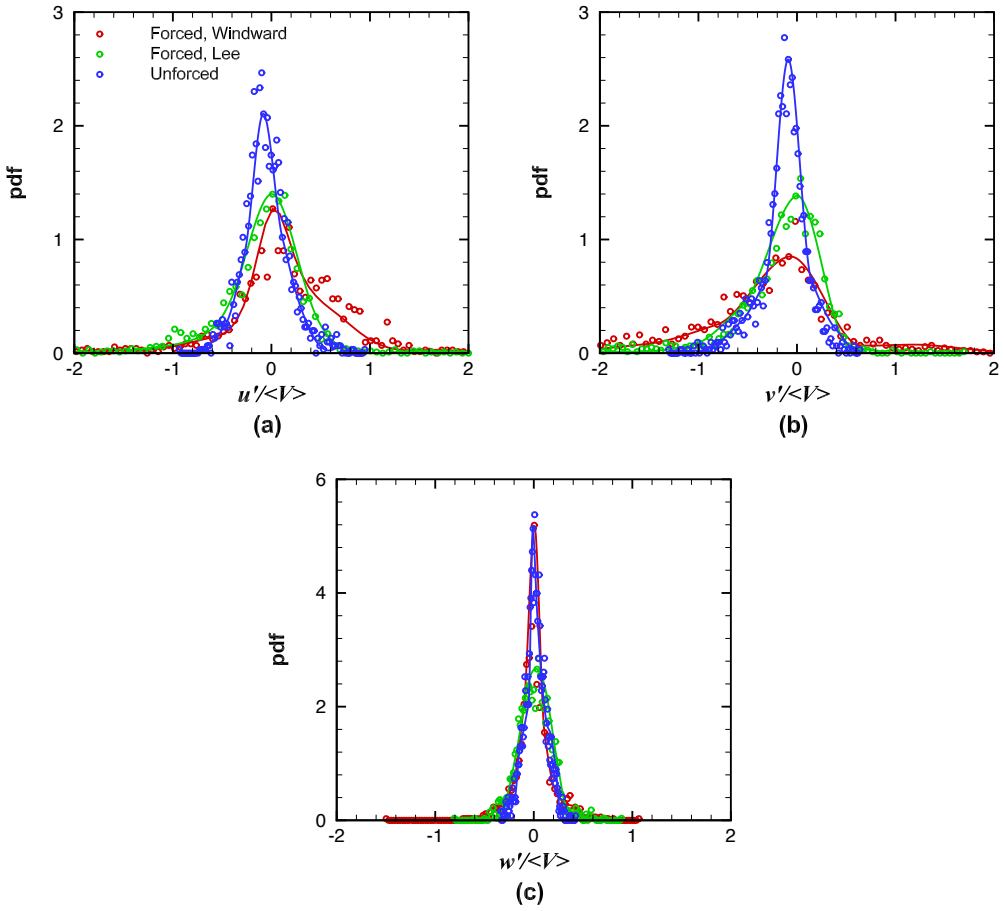

Figure 5.24. Probability density functions of the local gas velocity fluctuations conditioned at the flame base location. Velocity fluctuation components, (a) u', (b) v' and (c) w', are normalized by the mean gas velocity.

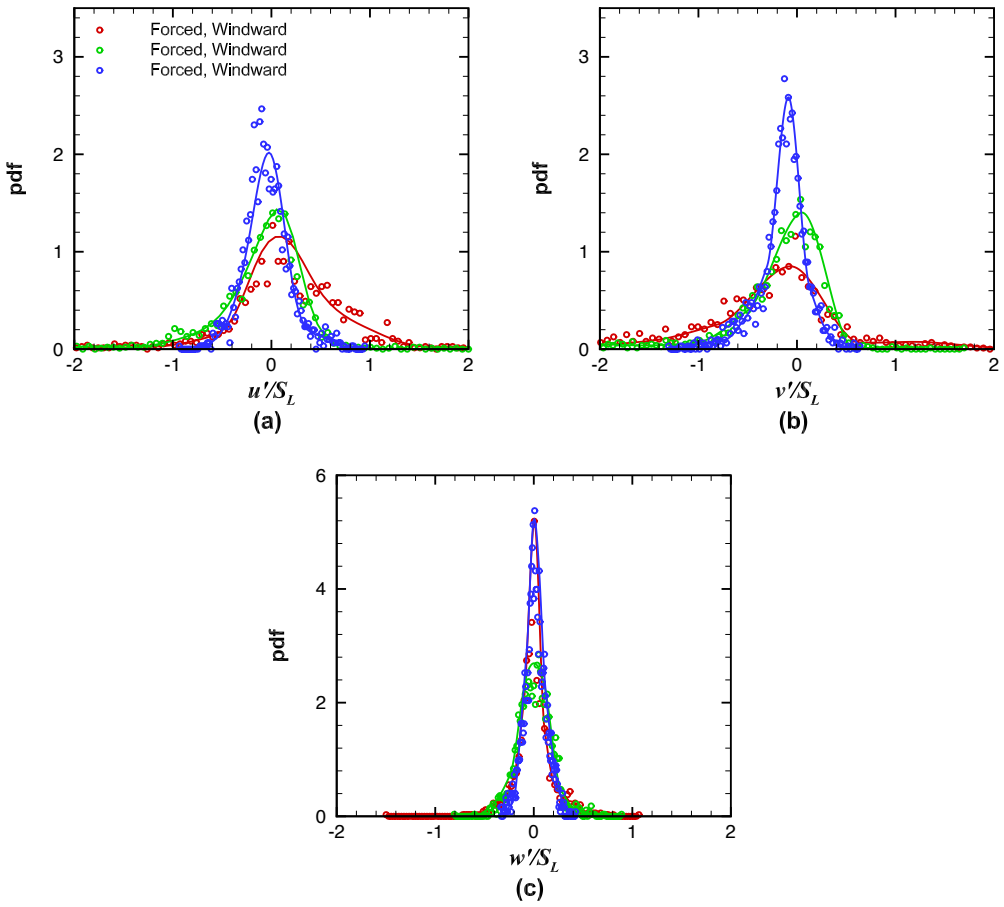

Figure 5.25. Probability density functions of the local gas velocity fluctuations conditioned at the flame base location. Velocity fluctuation components, (a) u', (b) v' and (c) w', are normalized by the laminar flame speed.

Several studies have found evidence that supports *Large Eddy* and *Edge Flame Concepts* (Pitts 1987, Lyons 2007). In the *Large Eddy* and *Edge Flame Concepts*, the propagation speed of the flame front plays an important role in flame stabilization. To determine the flame propagation speed, measurements of the velocity of the flame base and the local gas upstream of the flame base are necessary. From the time-resolved images of the flowfield, the velocity of the flame base can be determined from the motion of the flame marker using a similar methodology from Upatnieks *et al.* (2002, 2004). The velocity of the flame base is determined by a five-point central difference as follows

$$u_{f,i} = \frac{x_{f,i}^{(t+2)} + 8x_{f,i}^{(t+1)} - 8x_{f,i}^{(t-1)} - x_{f,i}^{(t-2)}}{12\Delta t} \tag{5.2}$$

For the JFICF geometry, all three components of the flame base velocity, $u_{f,i}$, are relevant; however, only the x and y-component of the velocity can be calculated from the planar measurements. In Eqn. 5.2, x_f is the location of the flame base, the subscript i indicates the direction of the component, the superscript t indicates the time step of the image frame and Δt is the time interval between time steps. The resolution of the flame marker is approximately 0.37 mm, so to reduce the resolution of $u_{f,i}$, the time interval is equivalent to five frames or Δt=1 ms. The resultant resolution of the flame base velocity is approximately 0.37 m/s, which is on the order of the laminar flame speed. Figures 5.26-5.28 show plots of the flame base location and calculated flame base velocity for the unforced, windward and lee cases. For the windward case, the flame base is out of view

in a number of movie frames. These frames were not considered in the analysis and result in blank portions of the time series. Discontinuities in the plots of the flame base location not associated with the flame moving out of view are the result of out-of-plane flame motion. These discontinuities result in peaks in the flame base velocity, which introduce bias errors in the flame propagation velocity. A 7x7 median filter was applied to the time series, but the filter was unable to remove all the peaks. As discussed in Section 5.2.3, the appearance of out-of-plane flame motion is preceded by a significant out-of-plane velocity, and therefore the time series can be filtered based on w. For clarity, the y_f location of the flame base at any frame, i, in the time series is written as $y_f(i)$, and therefore the flame base location in the previous frame is $y_f(i\text{-}1)$. Similar notation is written for the x location of the flame base, x_f. To systematically remove discontinuous regions, the difference between $y_f(i)$ and $y_f(i\text{-}1)$ is determined. If the difference is greater than one jet diameter, w in frame $i\text{-}1$ is determined at the flame base location $(x_f(i), y_f(i))$. If w is greater than 1 m/s, the frame i is removed. Figures 5.29-5.31 show the in-plane flame base velocity components calculated from the flame base motion after the discontinuous regions are removed.

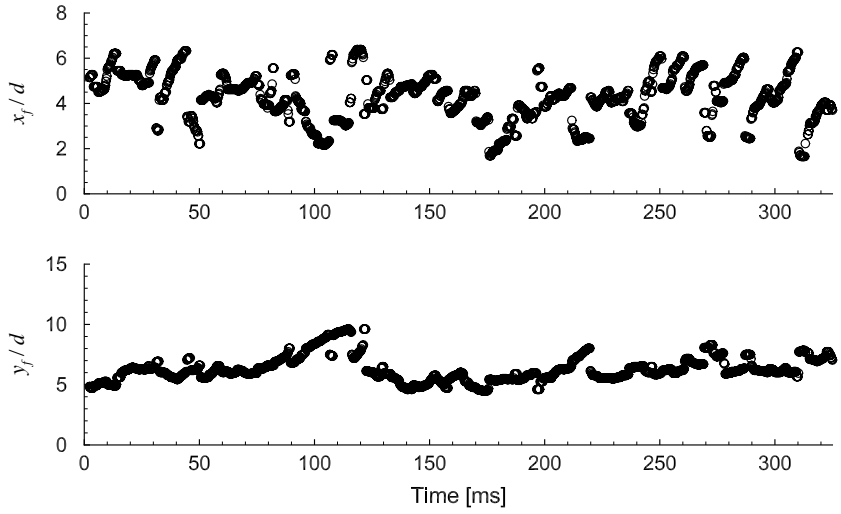

(a)

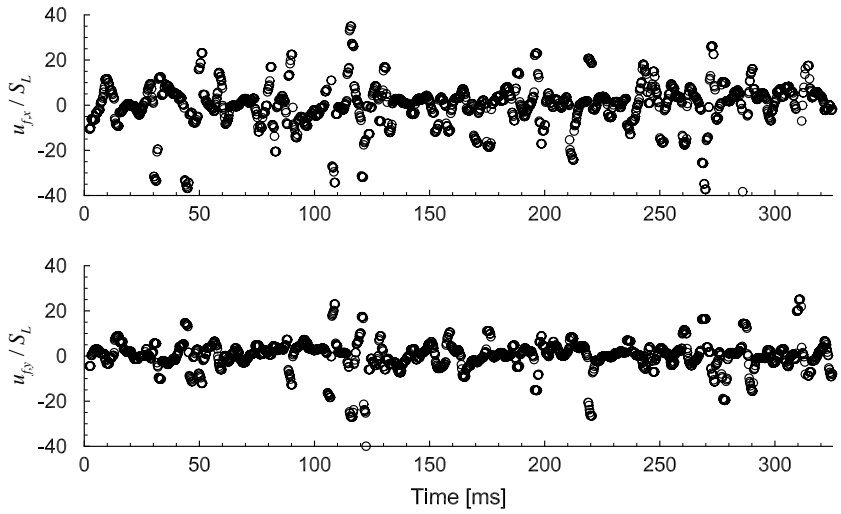

(b)

Figure 5.26. Time history of the flame base location (a) and the flame base velocity (b) for the lee-side flame base of an unforced non-premixed JFICF.

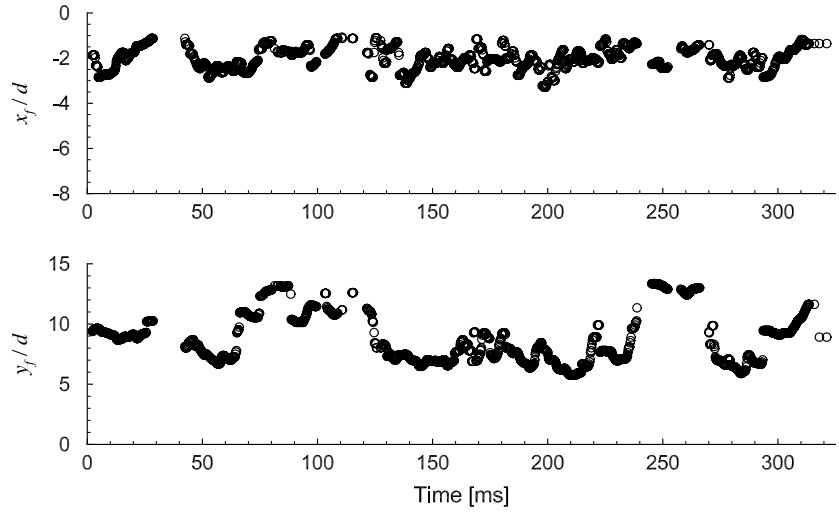

(a)

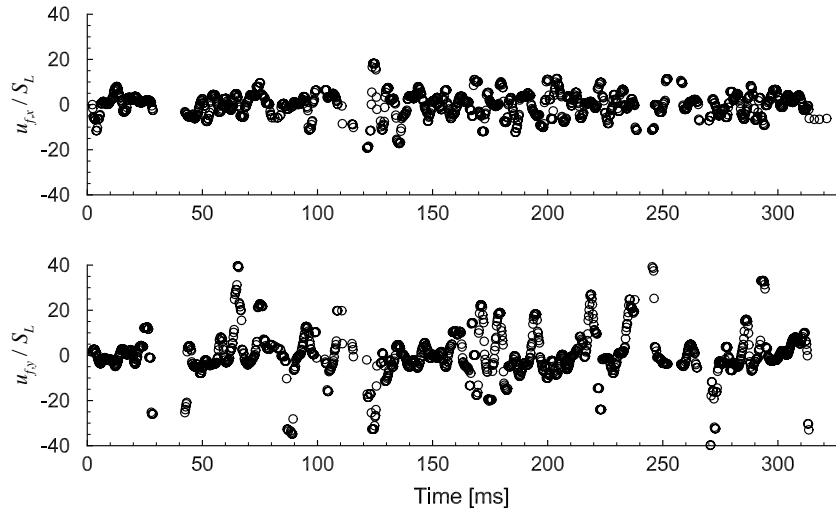

(b)

Figure 5.27. Time history of the flame base location (a) and the flame base velocity (b) for the windward-side flame base of a forced non-premixed JFICF.

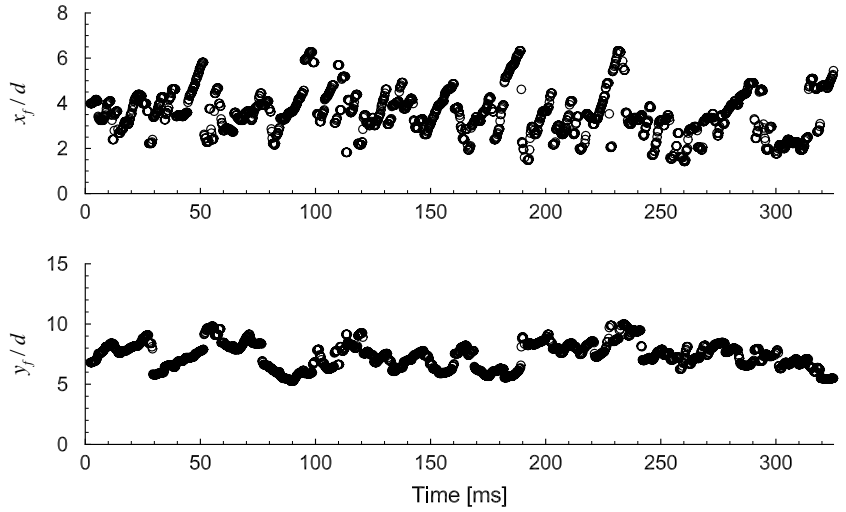

(a)

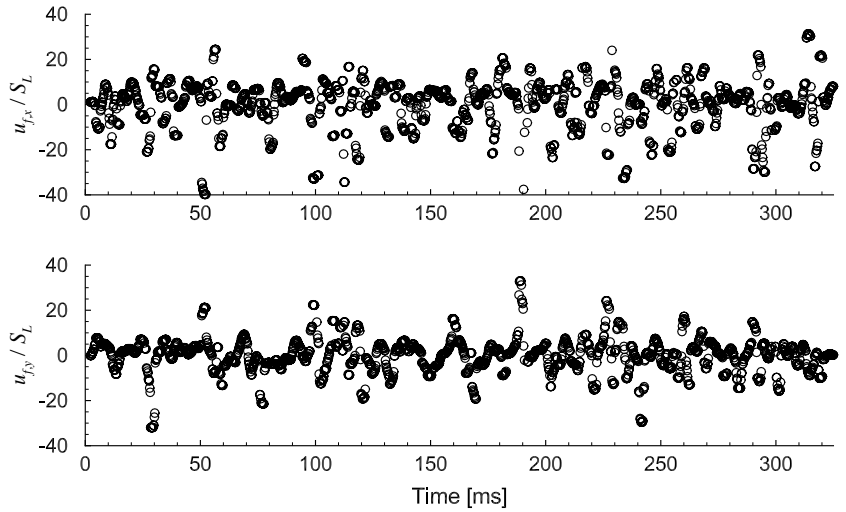

(b)

Figure 5.28. Time history of the flame base location (a) and the flame base velocity (b) for the lee-side flame base of a forced non-premixed JFICF.

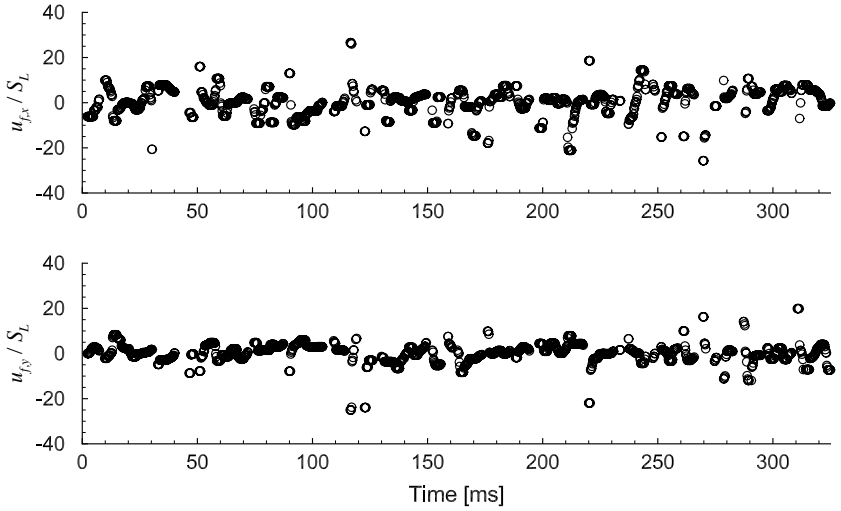

Figure 5.29. Time history of the flame base velocity for the lee-side flame base of an unforced non-premixed JFICF after discontinuous regions are removed.

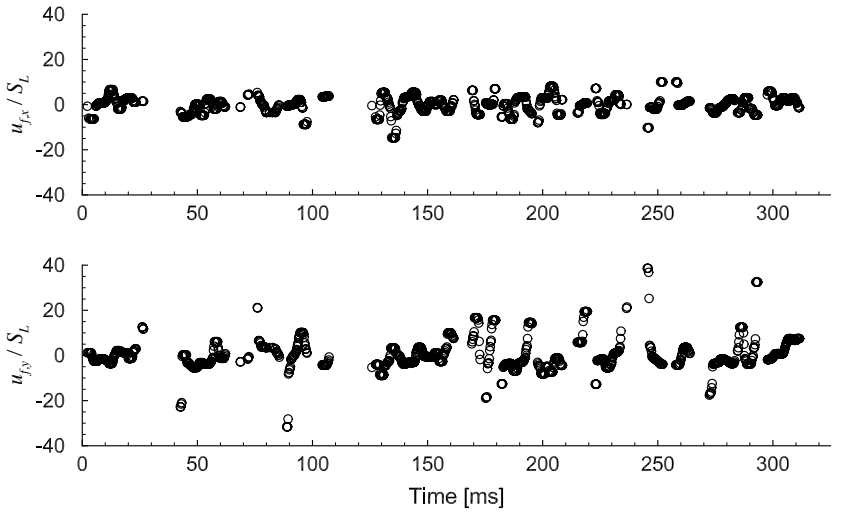

Figure 5.30. Time history of the flame base velocity for the windward-side flame base of a forced non-premixed JFICF after discontinuous regions are removed.

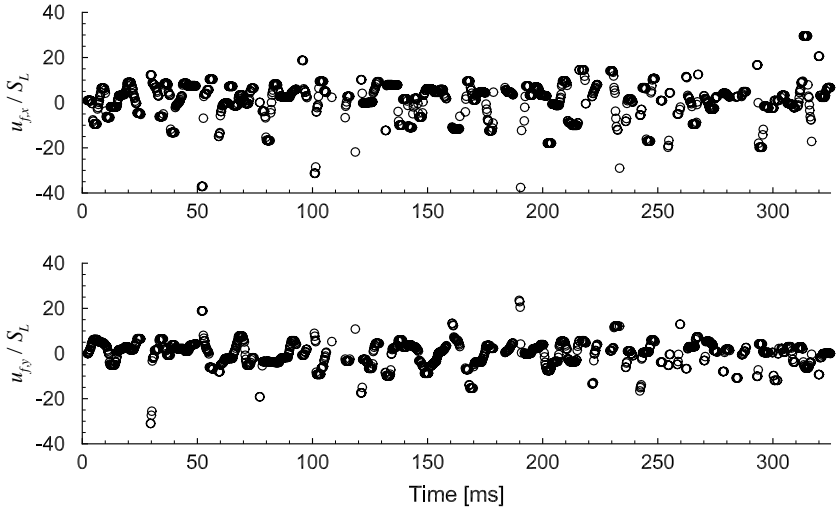

Figure 5.31. Time history of the flame base velocity for the lee-side flame base of a forced non-premixed JFICF after discontinuous regions are removed.

The flame propagation velocity, S_b, is determined from the difference between the velocity of the flame base and the local gas velocity. Figure 5.32 shows probability density functions of the flame propagation velocity. Again, the x and y components and the propagation speed are shown. The PDFs of flame propagation velocity collapse for unforced, windward and lee cases, which is rather surprising considering that the flame base motion and flowfield for each case is significantly different. The collapse suggests that the ejected vortical structures do not enhance the propagation speed of the flame. The PDFs of $S_{b,x}$ and $S_{b,y}$ show both positive and negative propagation velocities. In the forced case, positive and negative propagation are related to interactions between the flame and the vortical ejections. In general, individual vortical structures stretch the flame base and pull it closer to the jet exit resulting in positive propagation, and the integrated effect of vortical structures can extinguish the flame base resulting in negative propagation. For

the unforced case, positive propagation is the result of the CVP mixing fuel and air upstream of the flame base; however, the mechanism behind the negative propagation velocity is not as clear because the flame marking technique is not able to readily identify extinction—in the forced case, the local extinction was inferred. Positive and negative propagation velocities are not described by the *Premixed Flame* or *Turbulent Intensity Theory*; however, in the *Edge Flame Concept*, propagation speeds of an edge flame can be of either sign (Buckmaster 2002). The PDFs of $S_{b,x}$ and $S_{b,y}$ peak near the laminar flame speed, and the PDFs of $|S_b|$ peak near 2-3S_L. The widths of the PDFs in Figure 5.32a-c are quite large, where the tails extend to 10S_L. Upatnieks *et al.* (2002, 2004) found that the mean flame propagation velocity in lifted axisymmetric flames is on the order of the laminar flame speed, but did not report the range of the measured flame propagation velocities. The JFICF configuration is more sensitive to out-of-plane motions compared to the axisymmetric jet flame. Because the flame base is determined from a two-dimensional slice, the flame base velocity is biased toward higher speeds due to out-of-plane flame motion—a reaction zone that moves in or out of the imaging plane is interpreted as in-plane flame motion, and therefore inferred flame base velocity is biased by the convection of the reaction zone. Although peak flame base velocities due to discontinuities in the flame base motion are removed by conditioning on w, only large peaks associated with the initial appearance of out-of-plane flame motion are removed. After the flame appears, flame base velocities are calculated from the in-plane expansion of the flame. The bias associated with the in-plane expansion of an out-of-plane flame motion is likely to be small compared to the bias associated with discontinuities in the

flame motion. Upatnieks *et al.* (2004) conclude that their observations do not exclude turbulent propagation velocities in other flame configurations. Although the Reynolds number of the JFICF considered here are similar to the Reynolds numbers in Upatnieks *et al*. (2004), the crossflow enhances mixing and increases turbulence intensities. The increased turbulence may be a plausible explanation for the larger flame propagation.

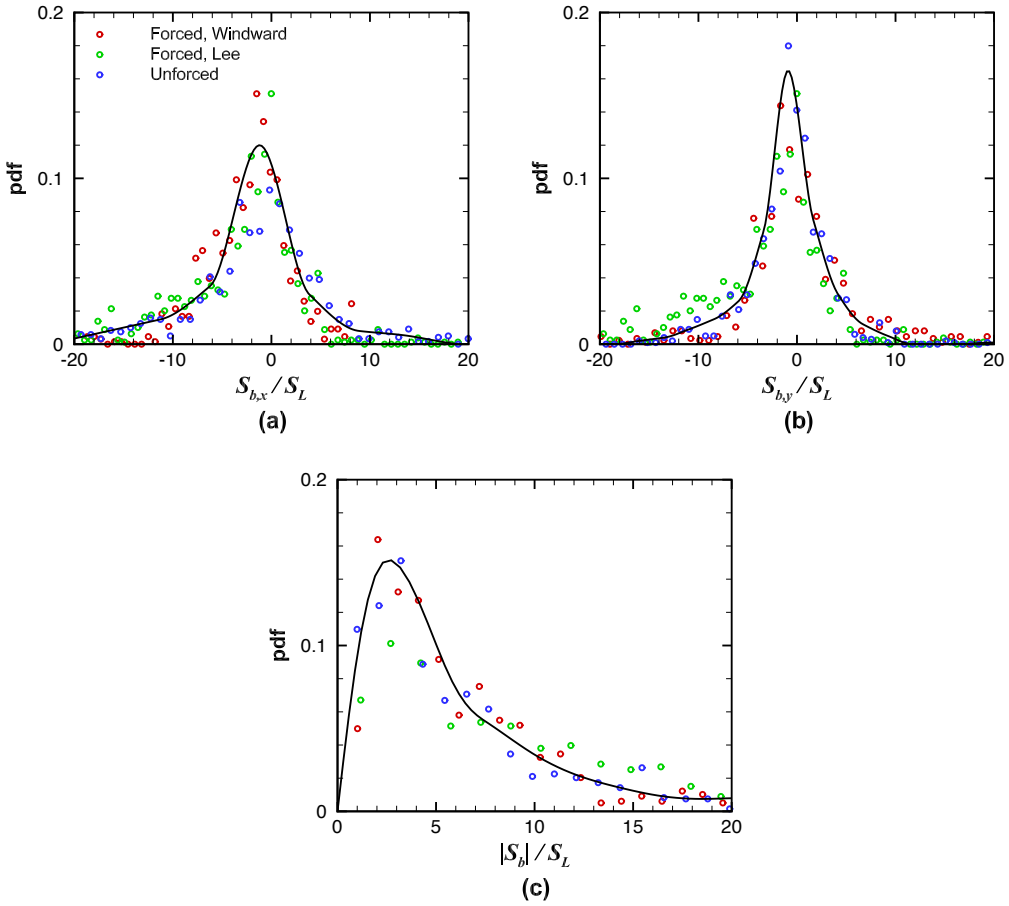

Figure 5.32. Probability density functions of the (a) *x*-component, (b) *y*-component and (c) magnitude of the flame propagation velocity normalized by the laminar flame speed.

5.3 SUMMARY

Time-resolved flowfield images show that the flame base regions of unforced and forced non-premixed JFICF exhibit different flow structures that result in different stabilization characteristics. For all three cases—the lee side of the unforced JFICF, the lee side of the forced JFICF and windward side of the forced JFICF—propagation of the flame base toward the jet exit is observed. For the unforced case, mixing induced by the CVP stabilizes the flame base. For the forced case, the vortex/flame interaction from the ejected vortical structure stabilizes the flame base. The windward-side flame base of the forced JFICF is also destabilized by the vortical ejections, where the integrated effect of vortical structures leads to extinction of the flame base. Because extinction of the flame base does not occur at regular intervals, the windward-side flame base motion does not respond regularly to the forcing frequency.

Flowfield statistics were obtained at the flame base locations for unforced and forced flames. For both flames, the local gas velocity is found to exceed $3S_L$. Turbulent flame speeds calculated from the x-component velocity fluctuations are found to be similar to the local gas velocity for the unforced JFICF and windward side of the forced JFICF, but not the lee side of the forced JFICF. From the flame marker, the velocity of the flame base was calculated and the flame propagation velocity was determined. The PDFs of flame propagation velocities collapse for both the forced and unforced JFICF, which suggests that the ejected vortical structures do not enhance flame propagation speed. The peak of the PDF of S_b occurs near 2-3S_L, which is larger than the flame propagation velocity found in axisymmetric flames. A possible explanation for the increased flame

propagation velocity is that the crossflow increases the turbulence intensities and the flame propagates at a higher turbulent flame speed.

Chapter 6: Conclusions

The effect of forcing on non-premixed and partially-premixed JFICF has been studied experimental. A variety of non-laser and laser-based diagnostic techniques have been used to determine the global combustion, mixing and flowfield characteristics of both unforced and forced JFICF.

6.1 Global Effects and Mixing Characteristics

Forced non-premixed and unforced partially-premixed turbulent JFICF are compact and blue in color indicating a reduction of soot. Simultaneous images of CH* chemiluminescence and PLMS reveal that the forced non-premixed JFICF flame structure is asymmetrically lifted and remains relatively stable. The flame length and windward-side liftoff height are relatively insensitive to amplitude ratio; however, the lee-side liftoff height increases as amplitude ratio increases.

The effects of forcing on global characteristics are related to the enhanced mixing of the forced JFICF. Mixture fraction fields for unforced and forced nonreacting JICF have been extracted from acetone PLIF images and show that forcing results in enhanced nearfield mixing. The jet trajectory of the forced JICF suggests that the forced JICF scales with $r_{peak}d$. The mixture fraction profile for the forced jet begins to decay earlier and decays at a faster rate than the profile of the unforced jet. Phase-averaged mixture fraction fields reveal that the enhanced mixing is due to three fluid mechanical phenomena:

(1) Ejected vortical structures entrain ambient crossflow air.

(2) The interaction between the ejected vortex pair in the current forcing cycle and the remnant vortical structure from the previous cycle results in "step-like" mixture fraction profiles where a well-mixed state is just downstream of a region of fuel rich fluid.

(3) Forcing induces reverse flow at the jet exit, which draws ambient air into the nozzle resulting in an ejection of partially premixed fluid.

A similar mixing process is likely to occur for fully lifted and possibly for partially lifted JFICF. As a result, forcing mixes the fuel in the nearfield resulting in a flame with a partially-premixed character.

Emissions of NOx, CO, and UHC have been measured for non-premixed and partially-premixed JFICF at both unforced and forced conditions for two fuels—a 70% methane/30% hydrogen blend and propane. Both forcing and partial premixing lead to similar reductions in NOx. *Forced non-premixed* JFICF, *unforced partially-premixed* JFICF, and *forced partially-premixed* JFICF have lower NOx emissions, but increased CO and UHC compared to an *unforced non-premixed* JFICF. As forcing or air dilution increase, net NOx production depends on competing effects—residence time for NOx production decreases, but soot radiation decreases and hence thermal NOx production increases. CO emissions are similar for forced non-premixed and unforced partially-premixed JFICF with similar NOx emissions; however, the mean Reynolds number of the unforced partially-premixed JFICF is smaller than the peak Reynolds number of the forced

non-premixed JFICF, which suggests that quenching for the forced flame depends on an effective strain rate that is smaller than the peak strain rates induced by forcing. UHC emissions increase drastically when forcing or air dilution fully lifts the flame exposing unburned fuel in the jet to the crossflow. For a constant fuel flow rate, increasing the amplitude ratio of a partially-premixed JFICF results in lower NOx emissions than increasing air dilution alone because the maximum amount of air dilution is limited by flame blowout. This suggests that the induced vortical structures due to forcing not only enhances mixing but also stabilizes the flame.

Simple NOx scaling analysis shows that forced non-premixed flames scale with amplitude ratio in the regime where $\tau_G<\tau_{G,crit}$. In this regime, the flame residence time is the dominant NOx mechanism. For $\tau_G>\tau_{G,crit}$, NOx emissions for different fuels do not collapse because the effect of soot radiation on thermal NOx becomes important and NOx production depends on the soot propensity of the particular fuel. Simple NOx scaling does not collapse EI_{NOx} for unforced partially-premixed flames. Scaling based on volumetric arguments does not adequately describe NOx emissions but succeeds in collapsing EI_{NOx} for forced non-premixed flames. A possible explanation is that in unforced partially-premixed flames, NOx production regions do not reach the jet centerline, whereas in forced non-premixed flames, induced vortical structures mix air and hot products, which creates regions amenable for NOx production throughout the jet volume.

6.2 FLAME STABILITY

Time-resolved flowfield measurements show that unforced and forced non-premixed JFICF exhibit different stability characteristics. The flame is interpreted from the evaporation of seed particles. At the flame base, the seed particle contour was found to be on average 1 mm from the OH layer. The unforced flame stability is dominated by the development of the CVP. The CVP carries well-mixed fluid to the flame base, which allows the flame base to propagate upstream. The forced flame stability is dictated by the strong vortical ejections, which interact with the flame base. An ejected vortical structure stretches and pulls the flame down and toward the centerline of the jet toward well-mixed fluid in the trailing column. Differences in the stability of the windward and lee side of the forced JFICF are also observed. The frequency spectra of both the windward and lee-side flame base motions were determined from the flame base inferred from luminosity movies of the forced JFICF. A peak at the forcing frequency was observed for the lee-side spectrum, but not for the windward-side spectrum, which indicates that the lee-side responds regularly to the forcing frequency but the windward side does not. Because the lee side of the flame base is located behind the jet, the lee-side flame base is stabilized in a similar manner to the lee side of the unforced JFICF. The difference between the lee sides of the forced and unforced flames is that the breakdown of vortical structures mixes fuel and air upstream of the flame base in the forced case, whereas the development of the CVP mixes fuel and air in the unforced case. The windward-side flame base is strained by the vortical structure and the incident crossflow. The integrated effect of the crossflow and repeated interactions with vortical structures causes the flame base to

extinguish. The extinction, however, does not occur at regular intervals due to the integrated nature of the extinction mechanism, and therefore, the windward-side flame motion does not respond regularly to the forcing frequency.

Flame stability was also investigated by determining the flowfield statistics conditioned on the flame base. The local velocity upstream of the flame base in all three cases was found to exceed $3S_L$. Turbulent flame speeds calculated from the x-component of the velocity fluctuations correlate well for the unforced JFICF and the windward side of the forced JFICF, but not the lee side, which implies that flame stabilization theories based solely on S_T do not provide a complete description of flame stability in forced flames. The velocity of the flame base and, in turn, the flame propagation velocity were determined. Flame propagation velocities were found to collapse for the unforced and forced JFICF, suggesting that flame stability is described more appropriately from an edge flame perspective. The collapse in propagation velocities also implies that ejected vortical structures induced by forcing do not enhance flame propagation velocity. The most probable flame propagation velocity is approximately 2-3S_L, which is larger than the laminar flame speed predicted by edge flame theories. The increased flame propagation velocity suggests that the flame base of the forced and unforced JFICF is not a purely laminar edge flame. The edge flame propagation velocity is possibly augmented by turbulent intensities and flame curvature.

6.3 FUTURE WORK

The effects of forcing and partial premixing on non-premixed JFICF are similar because both methods enhance mixing. Forcing, however, has an inherent safety advantage because the mixing of the fuel and air is limited to the near region of the jet flame and the region just upstream of the flame base. Although forcing has similar effects of soot, flame length and NOx reduction, CO and UHC emissions are larger for forced non-premixed JFICF than unforced partially-premixed JFICF. In both cases, increased UHC is expected due to the lifted flame base, which exposes unburned fuel to the crossflow. The larger increase in UHC, and also CO, for the forced non-premixed JFICF is due to the rapid entrainment of crossflow air by the ejected vortical structures, which potentially quenches reaction zones. To detail the quenching mechanism and its effect on UHC and CO, measurements of the scalar field are required; however, diagnostic techniques for scalar measurements of reacting flows are limited. Tracer methods using NO or acetone molecules are not suitable for reacting flow because the tracer molecules do not survive the high temperature reaction zone. Simultaneous Raman/Rayleigh/PLIF techniques that measure species containing carbon atoms are spatially limited and are difficult to implement in non-axisymmetric flowfields. Therefore, advances in the development of diagnostic techniques for scalar measurements are needed.

Further investigation on the role of soot in NOx production is also warranted. For propane flames, reduction in NOx is dependent on the amount of forcing or partial premixing because the presence of soot complicates NOx production. As soot volume fractions are reduced, the temperature of the flame increases, which results in increased

thermal NOx production. The global NOx emission of the flame is dependent of the net effects of reduced residence time and increased temperature. Simple NOx scaling analysis does not account for the effect of soot. In order to develop a complete NOx scaling law for forced flames, measurements of soot volume fraction and radiant fraction are necessary.

The liftoff height of the forced JFICF is dependent on the amplitude ratio, and therefore forcing can potentially provide an additional mechanism to control flame stability. The flame stability of the forced flame is quite complicated and the various flame stability theories do not provide a complete description. Although, the flame base of the forced JFICF exhibits characteristics of an edge flame, the propagation velocities are larger than the laminar flame speed; however, to determine the true propagation velocity, all three spatial components of the flame motion needs to be resolved. At present, three-dimensional experimental diagnostic are limited; however, simultaneous cross-plane or parallel-plane imaging may provide useful results.

Appendices

Appendix A: Acetone PLIF Corrections

Acetone planar laser-induced fluorescence is an oft-used laser diagnostic technique for quantitative measurements of mixture fraction in non-reacting jets. In order to extract mixture fraction fields from the acetone PLIF images, several standard corrections are required. First, background reflections were removed by subtracting a background image from the raw PLIF image of the jet. The background image was determined from averaging 50 images of the laser sheet with the crossflow on, but no jet flow. Second, to correct for non-uniformities in the laser sheet, the background subtracted jet image is divided by a laser sheet correction image. The laser sheet correction image was acquired by placing a sealed cell with trace amount of acetone in the test section of the tunnel. To reduce reflections in the acetone cell, the laser sheet was allowed to enter and pass through fuse silica windows on the top and bottom of the cell. Although acetone fluoresces in the visible and a fuse silica imaging window is not required, fuse silica was used because reflections from the UV laser caused BK-7 windows to fluoresce. The laser sheet correction image was obtained from an average of 25 images, where each image is acquired from ten laser pulses per image exposure. An example of the laser sheet correction image is shown in Figure A.1. Background images with the cell evacuated of acetone were also taken in the same manner and subtracted from the laser sheet images. Figure A.2 shows examples of a background corrected jet image and a sheet corrected jet image. The mixture fraction is then determined by normalizing the image by the maximum signal in the jet potential core.

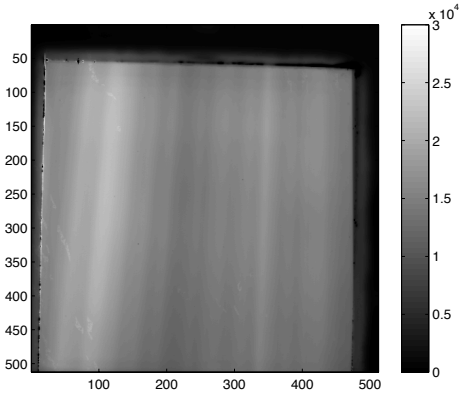

Figure A.1. Laser sheet correction image obtained from imaging the acetone cell.

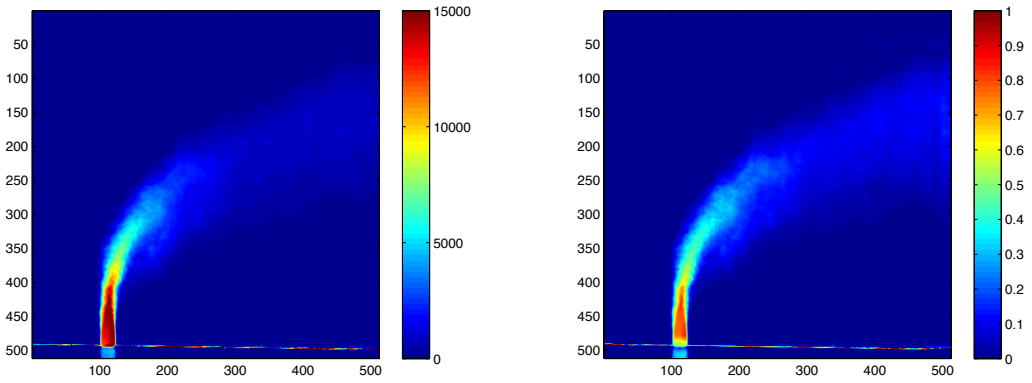

(a) (b)

Figure A.2. Uncorrected jet PLIF image (a) and sheet corrected jet PLIF image (b) of an unforced non-reacting JICF at Re=3250. The sheet corrected jet PLIF image is normalized by the maximum signal in the jet potential core.

As seen in Figure A.2b, the signal in the potential core is not uniform. Because the concentration of acetone (26% by volume) was not negligible, the non-uniformity of the potential core is the result of absorption of laser energy by the acetone molecules. The

attenuation of laser light intensity by absorption, I, is described by the Beer-Lambert Law as follows:

$$\ln\left(\frac{I}{I_0}\right) = -\alpha x \tag{A.1}$$

where the non-attenuated laser intensity, I_0, can be determined along a ray path, x, from the absorption coefficient, α, in m^{-1}. For collimated laser sheets, the absorption correction is straightforward, where the fluorescence signal can be corrected along ray paths that follow pixel rows or columns of the image. In the current study, the laser sheet was allowed to expand in order to image a larger field of view, and rays were not coincident with pixel rows or columns; therefore, the absorption must be corrected along the expanding ray paths. Here, the absorption correction for an expanding sheet follows the iterative scheme detailed by Smith (1996). To correct for absorption, the laser sheet correction image, L_0, is modified pixel by pixel to account for absorption from the jet as follows

$$\begin{aligned}\ln\frac{L_{\text{mod}}}{L_0}\bigg|_{i,j} = {} & (1-\tan\theta)\left(\ln\frac{L_{\text{mod}}}{L_0} - \alpha\frac{S_{jet}}{L_{\text{mod}}}\Delta x\right)\bigg|_{i+1,j} \\ & + \left(\frac{5}{6}\tan\theta\right)\left(\ln\frac{L_{\text{mod}}}{L_0} - \alpha\frac{S_{jet}}{L_{\text{mod}}}\Delta x\right)\bigg|_{i+1.j\pm1} \\ & + \left(\frac{1}{6}\tan\theta\right)\left(\ln\frac{L_{\text{mod}}}{L_0} - \alpha\frac{S_{jet}}{L_{\text{mod}}}\Delta x\right)\bigg|_{i.j\pm1}\end{aligned} \tag{A.1}$$

where, L_{mod} is the modified laser sheet correction, S_{jet} is the jet PLIF image, θ is the angle of the ray at the particular pixel location, and Δx is the spatial resolution of an image pixel. The indices i and j refer to the pixel row and column, i+1 refers to the row above pixel i and j+1 refers to the column to the right of pixel j. The laser sheet was brought in from the top of the test section, and thus the direction of the ray paths are from top to bottom. The ray paths are determined by imaging the resultant shadows of a comb placed in the laser sheet path on top of the acetone cell. The absorption corrected jet image is determined by dividing the jet PLIF image by the modified laser sheet correction. The absorption coefficient was found iteratively and conditioned on the uniformity of the potential core of the unforced JICF in the absorption corrected jet image. After applying the correction scheme, the uniformity of the potential core was within 97%; therefore, a reasonable estimate of the error introduced by the absorption correction is approximately 3%. Figure A.3 shows jet images uncorrected and corrected for absorption.

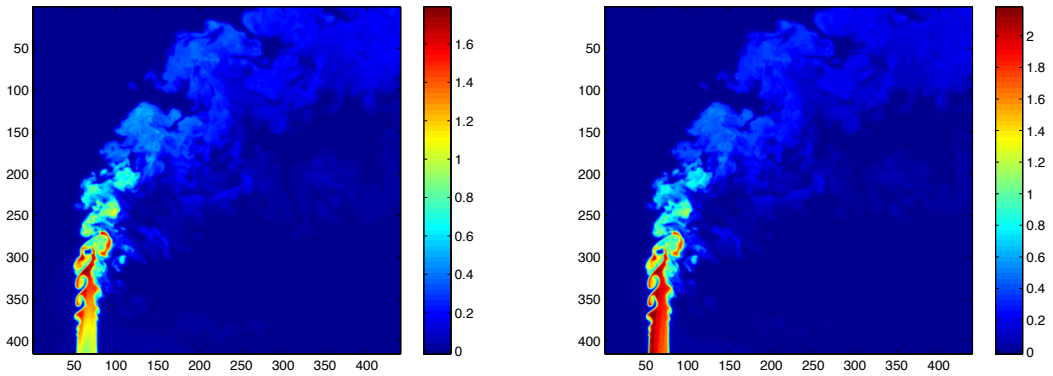

(a) (b)

Figure A.3. Uncorrected jet PLIF image (a) and absorption corrected jet PLIF image (b) of an unforced non-reacting JICF at Re=3250.

Appendix B: Flame Marking from Particle Seed Images

In order to indentify the flame base location, dark regions of evaporated or pyrolyzed particles are determined from the PIV particle seed images. The images are processed in Matlab using the image processing toolbox. Because particles are imaged as discrete pixel intensities, the edges of dark regions cannot be determined by applying an intensity threshold or marked by the intensity gradient. Instead, the image is divided into 10 x 10 pixel interrogation windows with 50% overlap, and the seed density of each window is determined by counting the number of intensity peaks. Peaks are determined by using the Matlab function *findpeaks*, where the minimum peak height defined as half the maximum pixel intensity in the entire non-windowed image. The resultant image of peak counts is assumed to be proportional to the particle seed density. The flame marker edge is determined from the binarized image conditioned on the 50% threshold of the maximum peak count. Figure B.1 shows images of seed particles (a), the seed density (b), and the flame marker edge (c).

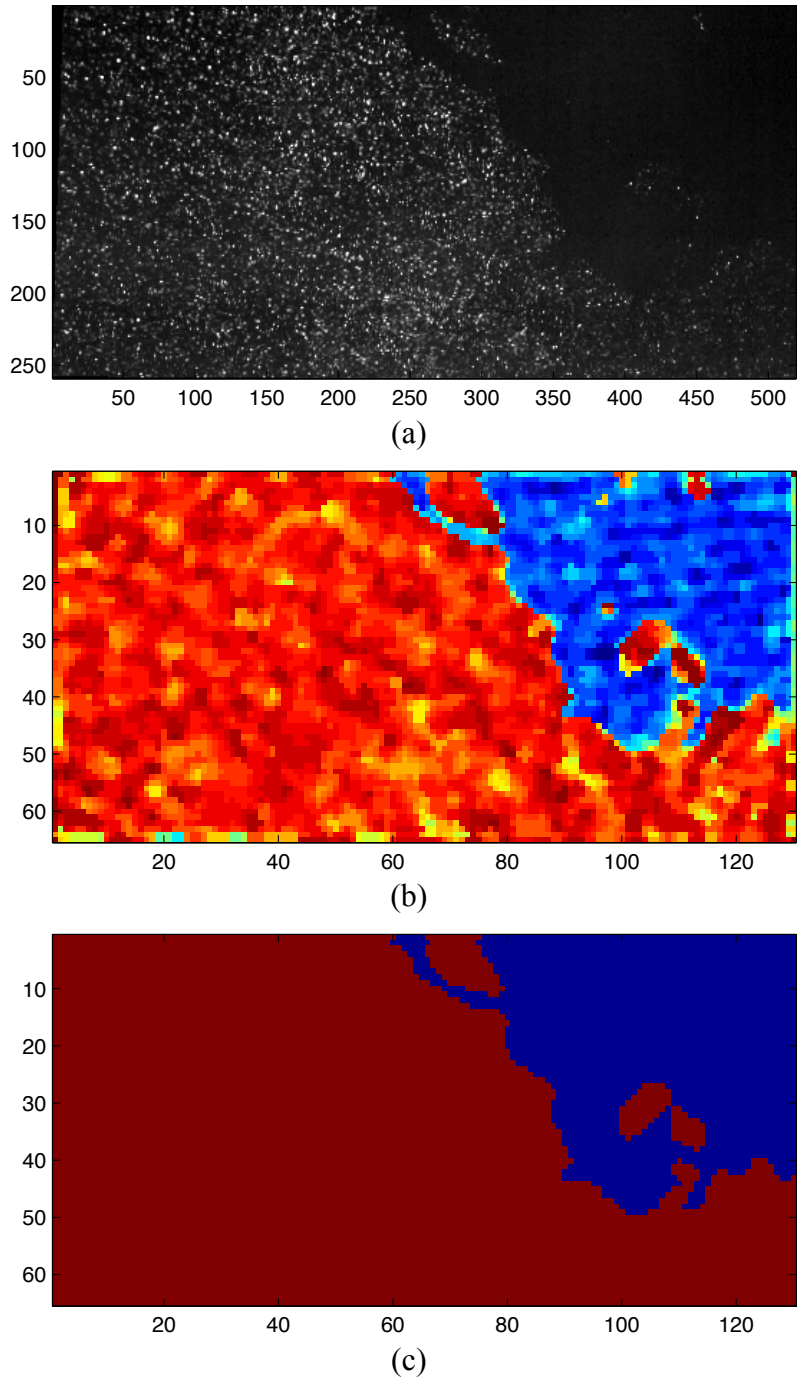

Figure B.1. Images of seed particles (a), seed density (b), and flame marker edge (c) for a $Re_{j,mean}$=6240 forced non-premixed JFICF.

Bibliography

Amantini, G., Frank, J. H., Gomez, A. (2004). Experiments on Standing and Traveling Edge Flames Around Flame Holes. *Proceedings of the Combustion Institute*, *30*, 313-321.

Bandaru, R. V., Turns, S. R. (2000). Turbulent Jet Flames in a Crossflow: Effects on Some Jet, Crossflow, and Pilot-Flame parameters on Emissions. *Combustion and Flame*, *121*, 137-151.

Bosanquet, C. H., Pearson, J. L. (1936). The Spread of Smoke and Gasses from Chimneys. *Transactions of the Faraday Society*, *32*, 1249.

Broadwell, J. E., Breidenthal, R. E. (1984). Structure and Mixing of a Transverse Jet in Incompressible Flow. *Journal of Fluid Mechanics*, *148*, 405-412.

Broadwell, J. E., Lutz, A. E. (1998). A Turbulent Jet Chemical Reaction Model: NOx Production in Jet Flames. *Combustion and Flame*, *114*, 319-335.

Broadwell, J. E., Dahm, W. J., Mungal, M. G. (1984). Blowout of Turbulent Diffusion Flames. *Proceedings of the Combustion Institute*, *20*, 303-310.

Buckmaster, J. (2002). Edge-Flames. *Progress in Energy and Combustion Science*, *28*, 435-475.

Chao, Y. C., Yu, C. Y., Yuan, T. (2002). Stabilization Process of a Lifted Flame Tuned by Acoustic Excitation. *Combustion Science and Technology*, *174*, 87-110.

Chao, Y. C., Yuan, T., Tseng, C.-S. (1996). Effects of Flame Lifting and Acoustic Excitation on the Reduction of NOx Emissions. *Combustion Science and Technology*, *113-114*, 49-65.

Chen, R. H., Driscoll, J. F. (1991). Nitric Oxide Levels of Jet Diffusion Flames: Effects of Coaxial Air and Other Mixing Parameters. *Proceedings of the Combustion Institute*, *23*, 281-288.

Crow, S. C., Champagne, F. H. (1971). Orderly Structure in Jet Turbulence. *Journal of Fluid Mechanics*, *48*, 547-591.

Dahm, W. J., Mayman, A. G. (1990). Blowout Limits of Turbulent Jet Diffusion Flames for Arbitrary Source Conditions. *AIAA Journal*, *28*, 1157-1162.

Demare, D., Baillot, F. (2004). Acoustic Enhancement of Combustion in Lifted Nonpremixed Jet Flames. *Combustion and Flame*, *139*, 312-328.

Donbar, J. M., Driscoll, J. F., Carter, C. D. (2000). Reaction Zone Structure in Turbulent Nonpremixed Jet Flames-From CH-OH PLIF Images. *Combustion and Flame*, *122*, 1-19.

Drake, M. C., Correa, S. M., Pitz, R. W., Shyy, W., Fenimore, C. P. (1987). Superequilibrium and Thermal Nitric Oxide Formation in Turbulent Diffusion Flames. *Combustion and Flame*, *69*, 347-365.

Driscoll, J. F., Chen, R. H., Yoon, Y. (1992). Nitric Oxide Levels of Turbulent Jet Diffusion Flames: Effects of Residence Time and Damkohler Number. *Combustion and Flame*, *88*, 37-49.

El Behery, R. E., Mohamad, A. A., Kamal, M. M. (2005). Combustion Enhancement of a Gas Flare using Acoustical Excitation. *Combustion Science and Technology*, *177*, 1627-2659.

Eroglu, A., Breidenthal, R. E. (2001). Strucutre, Penetration, and Mixing of Pulsed Jets in Crossflow. *AIAA Journal*, *39*, 417-423.

Fregeau, M., Hermanson, J. C. (2009). CO/NOx Emissions of Strongly Pulsed Jet Diffusion Flames. *Combustion Science and Technology*, *181*, 536-554.

Frick, T. F., Roshko, A. (1994). Vortical Structure in the Wake of a Transverse Jet. *Journal of Fluid Mechanics*, *279*, 1-47.

Gamba, M. (2009). *Volumetric PIV and OH PLIF Imaging in the Far Field of Nonpremixed Jet Flames*. Ph.D Thesis, The University of Texas at Austin, Department of Aerospace Engineering and Engineering Mechanics.

Garner, J. E. (1967). *A Review of Jet Efflux Studies Applicable to V/STOL Aircraft*. USAF-AEDC.

Gore, J. P., Zhan, N. J. (1996). NOx Emission and Major Species Concentrations in Partially Premixed Laminar Methane/Air Co-flow Jet Flames. *Combustion and Flame*, *105*, 414-427.

Gutmark, E., Parr, T. P., Hason-Parr, D. M., Schadow, K. C. (1989). On the Role of Large and Small Scale Structures in Combustion Control. *Combustion Science and Technology*, *66*, 107-126.

Gutmark, E., Parr, T. P., Hason-Parr, D. M., Schadow, K. C. (1992). Structure of a Contrlled Duct Flame. *Combustion Science and Technology*, *87*, 217-239.

Han, D., Mungal, M. G. (2003). Simultaneous Measurements of Velocity and CH Distribution. Part II: Deflected Jet Flames. *Combustion and Flame*, *133*, 1-17.

Hasselbrink, E. F., Mungal, M. G. (1998). Observations of the Stabilization Region of Lifted Non-Premixed Methane Transverse Jet Flames. *Proceedings of the Combustion Institute*, *27*, 1167-1173.

Hasselbrink, E. F., Mungal, M. G. (2001a). Transverse Jets and Jet Flames. Part 1. Scaling Laws for Strong Transverse Jets. *Journal of Fluid Mechanics*, *443*, 25.

Hasselbrink, E. F., Mungal, M. G. (2001b). Transverse Jets and Jet Flames. Part 2. Velocity and OH Field Imaging. *Journal of Fluid Mechanics*, *443*, 27-68.

Hermanson, J. C., Ghaem-Maghami, E., Johari, H. (2004). CO/Unburned Hydrocarbon Emissions of Strongly-Pulsed Turbulent Diffusion Flames. *Combustion Science and Technology*, *176*, 1855-1866.

Huang, H., Dabiri, D., Gharib, M. (1997). On Errors of Digital Particle Image Velocimetry. *Measurement Science and Technology*, *8*, 1427-1440.

Johari, H. (2006). Scaling of Fully Pulsed Jets in Crossflow. *AIAA Journal*, *44* (11), 2719-2725.

Johari, H., Paduano, R. (1997). Dilution and Mixing in an Unsteady Jet. *Experiments in Fluids*, *23*, 272-280.

Johari, H., Pacheco-Tougas, M., Hermanson, J. C. (1999). Penetration and Mixing of Fully Modulated Turbulent Jets in Crossflow. *AIAA Journal*, *37*, 842-850.

Kalghatgi, G. T. (1981). Blow-Out Stability of Gaseous Jet Diffusion Flames Part II: Effect of Cross Wind. *Combustion Science and Technology*, *26*, 241-244.

Kalghatgi, G. T. (1984). Lift-off Heights and Visible Lengths of Vertical Turbulent Jet Diffusion Flames in Still Air. *Combustion Science and Technology*, *41*, 17-29.

Kalghatgi, G. T. (1983). The Visible Shape and Size of a Turbulent Hydrocarbon Jet Diffusion Flame in a Cross-Wind. *Combustion and Flame*, *52*, 91-106.

Keller, J. O., Bramlette, T. T., Barr, P. K., Alvarez, J. R. (1994). NOx and CO Emissions from a Pulse Combustor Operating in a Lean Premixed Mode. *Combustion and Flame*, *99*, 460-466.

Kelso, R. M., Smits, A. J. (1995). Horseshoe Vortex Systems Resulting from the Interaction between a Laminar Boundary Layer and a Transverse Jet. *Physics of Fluids*, *7*, 153-158.

Kelso, R. M., Lim, T. T., Perry, A. E. (1996). An Experimental Study of Round Jets in Cross-Flow. *Journal of Fluid Mechanics*, *306*, 111-144.

Kim, M., Choi, Y., Oh, J. Y. (2009). Flame–Vortex Interaction and Mixing Behaviors of Turbulent Non-Premixed Jet Flames Under Acoustic Forcing. *Combustion and Flame*, *156*, 2252–2263.

Kim, T. K., Alder, B. J., Laurendeau, N. M., Gore, J. P. (1995). Exhaust and In-Situ Measurements of Nitric Oxide for Laminar Partially Premixed C2H6-Air Flames. *Combustion Science and Technology*, *110-111*, 361-378.

Kothnur, P. S., Clemens, N. T. (2005). Effects of Unsteady Strain Rate on Scalar Dissipation Structures in Turbulent Planar Jets. *Physics of Fluids*, *17*, 125104.

Lakshminarasimhan, K., Clemens, N. T., Ezekoye, O. A. (2006). Characteristics of Strongly-Forced Turbulent Jets and Jet Flames. *Experiments in Fluids*, *41*, 523-542.

Lakshminarasimhan, K., Ryan, M. D., Clemens, N. T., Ezekoye, O. A. (2007). Mixing Characteristics in Strongly Pulsed Methane Jet Flames. *Proceedings of the Combustion Institute*, *31*, 1617-1624.

Law, C. K. (2006). *Combustion Physics*. New York: Cambridge University Press.

Lawson, N. J., Wu, J. (1997). Three-Simensional Particle Image Velocimetry: Error Analysis of Stereoscopic Techniques. *Measurement Science and Technology*, *8*, 894-900.

Lovett, J. A., Turns, S. R. (1993). The Structure of Pulsed Turbulent Nonpremixed Jet Flames. *Combustion Science and Technology*, *94*, 183-217.

Lozano, A., Yip, B., Hanson, R. K. (1992). Acetone: A Tracer for Concentration Measurements in Gaseous Flows by Planar Laser Induced Fluorescence. *Experiments in Fluids*, *13*, 369-376.

Lyle, K. H., Tseng, L. K., Gore, J. P., Laurendeau, N. M. (1999). A Study of Pollutant Emission Characteristics of Partially Premixed Turbulent Jet Flames. *Combustion and Flame*, *116*, 627-639.

Lyons, K. M. (2007). Toward an Understanding of the Stabilization Mechanisms of Lifted Turbulent Jet Flames: Experiments. *Progress in Energy and Combustion Science*, *33*, 211-231.

Margason, R. J. (1993). Fifty Years of Jet in Cross Flow Research. *AGARD Conference Proceedings 534. CP-534*. AGARD.

Margason, R. J. (1968). *The Path of a Jet Directed at Large Angles to a Subsonic Free Stream*. NASA Tech Report. NASA.

M'Closkey, R. T., King, J. M., Cortelezzi, L., Karagozian, A. R. (2002). The Actively Controlled Jet. *Journal of Fluid Mechanics*, *452*, 325-335.

Muñiz, L., Mungal, M. G. (1997). Instantaneous Flame-Stabilization Velocities in Lifted-Jet Diffusion Flames. *Combustion and Flame*, *111*, 16-31.

Muramatsu, A., Era, Y. (2003). Mixing of Carbon Dioxide Gas and Air by a Pulsating Jet with a Reverse Flow. *Proceedings of the 4th ASME-JSME Joint Fluids Engineering Conference*. Honolulu.

Oh, S. K., Shin, H. D. (1998). A Visualization Study on the Effect of Amplitude ratio on Tone-Excited Isothermal Jets and Jet Diffusion Flames. *International Journal of Energy Research*, *22*, 343-354.

Parikh, P. G., Moffat, R. J. (1982). Resonant Entrainment of a Confined Pulsed Jet. *Transactions of the ASME*, *104*, 482-488.

Peters, N., Donnerhack, S. (1981). Stucture and Similarity of Nitric Oxide Production in Turbulent Diffusion Flames. *Proceedings of the Combustion Institute*, *18*, 33-42.

Peters, N., Williams, F. A. (1983). Liftoff Characteristics of Turbulent Jet Diffusion Flames. *AIAA Journal*, *21*, 423-429.

Pitts, W. M. (1989). Assessment of Theories for the Behavior and Blowout of Lifted Turbulent Jet Diffusion Flames. *Proceedings of the Combustion Institute*, *22*, 809-816.

Pratte, B. D., Baines, W. D. (1967). Profiles of the Round Turbulent Jet in a Cross Flow. *Journal of the Hydraulics Division Proceedings of the ASCE*, *92*, 53-64.

Raffel, M. W. (2007). *Particle Image Velocimetry: A Practical Guide* (2nd ed.). Springer.

Renard, P.-H., The´venin, D., Rolon, J. C., Candel, S. (2000). Dynamics of Flame/Vortex Interactions. *Progress in Energy and Combustion Science*, *26*, 225-282.

Roberts, W. L., Driscoll, J. F. (1991). Laminar Vortex Interacting with a Premixed Flame: Measured Formation of Pockets and Reactants. *Combustion and Flame*, *87*, 245-256.

Ruetsch, G. R., Vervisch, L., Liñán, A. (1995). Effects of Heat Release on Triple Flames. *Physics of Fluids*, *7*, 1447-1454.

Smith, S. H. (1996). *The Scalar Concentration Field of the Axisymmetric Jet in Crossflow*. Ph.D Thesis, Stanford University, Mechanical Engineering.

Smith, S. H., Mungal, M. G. (1998). Mixing, Structure and Scaling of the Jet in Crossflow. *Journal of Fluid Mechanics*, *357*, 83-122.

Steinberg, A. M., Driscoll, J. F. (2008). Measurements of Turbulent Premixed Flame Dynamics using Cinema Stereocopic PIV. *Experiments in Fluids*, *44*, 985-999.

Su, L. K., Mungal, M. G. (2004). Simultaneous Measurements of Scalar and Velocity Field Evolution in Turbulent Crossflowing Jets. *Journal of Fluid Mechanics*, *513*, 1-45.

Su, L. K., Sun, O. S., Mungal, M. G. (2006). Experimental Investigation of Stabilization Mechanisms in Turbulent, Lifted Jet Diffusion Flames. *Combustion and Flame*, *144*, 494-512.

Tang, Y. M., Waldherr, G., Jagoda, J. I., Zinn, B. T. (1995). Heat Release Timing in a Non-Premixed Helmholtz Pulse Combustor. *Combustion and Flame*, *100*, 251-261.

Tsurikov, M. (2003). *Experimental Investigation of the Fine-Scale Structure in Turbulent Gas-Phase Jet Flows*. Ph.D Thesis, The University of Texas at Austin, Department of Aerospace Engineering and Enginering Mechanics.

Turns, S. R. (1995). Understanding NOx Formation in Nonpremixed Flames: Experiments and Modelling. *Prog. Energy Combust. Sci.*, *21*, 361-385.

Turns, S. R., Myhr, F. H., Bandaru, R. V., Maund, E. R. (1993). Oxides of Nitrogen Emissions from Turbulent Jet Flames: Part II-Fuel Dilution and Partial Premixing Effects. *Combustion and Flame*, *93*, 255-269.

Upatnieks, A., Driscoll, J. F., Ceccio, S. L. (2002). Cinema Particle Imaging Velocimetry Time History of the Propagation Velocity of the Base of a Lifted Turbulent Jet Flame. *Proceedings of the Combustion Institute*, *29*, 1897-1903.

Upatnieks, A., Driscoll, J. F., Rasmussen, C. C., Ceccio, S. L. (2004). Liftoff of Turbulent Jet Flames-Assessment of Edge Flame and Other Concepts Using Cinema-PIV. *Combustion and Flame*, *138*, 259-272.

Van Doorne, C. W., Westerweel, J. (2006). Measurement of Laminar, Transitional and Turbulent Pipe Fow using Stereoscopic-PIV. *Experiments in Fluids*, *42*, 258-279.

Vanquickenborne, L., Van Tiggelen, A. (1966). The Stabilization Mechanism of Lifted Diffusion Flames. *Combustion and Flame*, *10*, 59-69.

Vermeulen, P. J., Chin, C. F., Yu, W. K. (1990). Mixing of an Acoustically Pulsed Air Jet with a Confined Crossflow. *Journal of Propulsion and Power*, *6*, 777-783.

Vermeulen, P. J., Rainville, P., Ramesh, V. (1992). Measurements of the Entrainment Coefficient of Acoustically Pulsed Axisymmetric Free Air Jets. *Journal of Engineering for Gas Turbines and Power*, *114*, 409-415.

Watson, K. A., Lyons, K. M., Donbar, J. M., Carter, C. D. (1999). Scalar and Velocity Field Measurements in a Lifted CH4-Air Diffusion Flame. *Combustion and Flame*, *117*, 257-271.

Watson, K. A., Lyons, K. M., Donbar, J. M., Carter, C. D. (2000). Simultaneous Rayleigh Imaging and CH-PLIF Measurements in a Lifted Jet Diffusion Flame. *Combustion and Flame*, *123*, 252-265.

Westerweel, J. (2000). Theoretical Analysis of the Measurement Precision in Particle Image Velocimetry. *Experiments in Fluids*, *[Supp.]*, S3-S12.

Wieneke, B. (2005). Stereo-PIV using Self-Calibration on Particle Images. *Experiments in Fluids*, *39*, 267-280.

Zinn, B. T. (1992). Pulse Combustion: Recent Applications and Research Issues. *Proceedings of the Combustion Institute*, *24*, 1297-1305.

Vita

Kevin C. Marr was born in Dallas, TX on January 6, 1982. In August 2000, he enrolled at the University of Texas at Austin. In December 2003, he graduated with High Honors and received his Bachelor of Science in Aerospace Engineering. In June 2004, he continued on with graduate studies at the University of Texas at Austin, and in December 2005, he earned his Master of Science in Aerospace Engineering. After spending a year attending the University of Michigan, he returned to the University of Texas at Austin in August 2006 to pursue a Ph.D.